Centre for Materials and Structures - School of Engineering

University of Liverpool

Experimental and numerical characterisation of the plastic zone of a fatigue crack at various values of strain hardening exponent.

‘Thesis submitted in accordance with the requirements of the University of Liverpool for the degree of Doctor in Philosophy

By

Komal Shah

December 2017

Acknowledgement

I would like to take this opportunity to express my sincere and heartfelt thanks to my supervisor Prof Eann Patterson (AA Griffith Chair of Structural Materials & Mechanics, University of Liverpool) for trusting me and believing in me to complete this doctoral dissertation. I appreciate his advice and encouragement that has helped guide my studies and thesis research. I truly appreciate the trust and freedom he allowed me to work through problems while not losing the sight of a bigger picture. No written words can express my gratitude and respect for him. I would like to thank Prof Gordon Tatlock (Henry Bell Wortley Prof of Materials Engineering) and Prof Neil James (Head of School of Marine Science & Engineering/ Associate Dean, University of Plymouth) for their invaluable discussions and suggestions. I would like to thank Mathew Jijimon and Dave Atkinson for their continuous help with lab work. I would also like to show my special gratitude to Peter Bond, Dr Roy Moate and Terry Richards for their help with BSE work at Plymouth University. Especially, I wish to thank my parents and mother-in-law for always supporting, encouraging and believing in me. Finally, and most importantly, I wish to thank the love of my life, my husband Ronak and my son Avyukt. They motivated me, supported me and loved me. They are the most important people in my world and I dedicate this thesis to them.

Abstract

Fatigue crack analysis is an essential tool for life prediction and maintenance of components subjected to constant and variable amplitude loading. Investigation of crack growth mechanisms such as crack closure and crack growth retardation due to overload can lead to design optimization as they cause retardation of crack growth, which implies there is a potential opportunity to extract more life from a mechanical component. Despite of enormous literature suggesting the effect of various variables on crack closure, the effect of value of strain hardening exponent on fatigue crack closure is poorly understood and not validated experimentally. Strain hardening also known as work hardening is the term used to describe the phenomenon that most metals become stronger when plastically deformed. In the current project, experiments were carried out on CT specimens of three different materials viz. pure Titanium, Al2024-T3 and Al6061-T6 whose value of strain hardening exponent was 6, 8 and 14 respectively to investigate the effect of the value of strain hardening exponent on crack closure and it was observed that the extent of crack closure was different for different value of strain hardening exponent. The experiments were carried out on all three materials to identify the effect of value of strain hardening exponent on post-overload fatigue crack growth and it was found that, the post-overload crack growth retardation was higher for the material with higher value of strain hardening exponent. The experimental plastic zones were obtained using Thermoelastic Stress Analysis (TSA) technique and it was concluded that, at a higher value of strain hardening exponent (n=6), the radius of the plastic zone is smaller than for a lower value of strain hardening exponent (n=14) for the same crack length. It has been established that the value of strain hardening exponent plays a major role on the size of the plastic zone, values of ΔK_I and crack growth retardation demonstrating that it is an important material parameter.

The pioneering analysis of Hutchinson [17] and Rice and Rosengren [18] to characterise the crack-tip stress fields in the case of strain hardening materials for small scale yielding crack problems in plane strain for mode I or mode II stress distributions was extended by Shih for mixed mode loadings and he plotted the plastic zone contours of a fatigue crack as a function of value of strain hardening exponent, n. Despite of numerous studies have been carried out, these plastic zone contours have never been demonstrated experimentally. Another purpose of this work was to fill that gap by experimentally characterizing the plastic zone of a fatigue crack at different values of strain hardening exponent. It has been revealed that experimental results do not validate Shih's predictions but they are in accordance with Hutchinson's solution.

The research to date has tended to focus on the extent of plastic zone parallel to the direction of crack growth; however, little attention has been paid to model the plastic zone perpendicular to the direction of crack growth. The radius of the plastic zone, $\boldsymbol{r_p}$ is not a reliable measure as the shape of the plastic zone changes with specimens of different thickness and during different modes of loading. Therefore it was decided to consider the area of the plastic zone as a reliable parameter to characterise the plastic work ahead of the crack tip instead of relying on either the size or shape of the plastic zone. It has been demonstrated that the plastic zone size is dependent on the value of strain hardening exponent but the shape is independent of the value of strain hardening exponent. Hence, a novel method to model the plastic zone size using a mathematical function has been proposed. The plastic zone size was determined by applying Irwin and Dugdale's plastic zone radius as variables in the equation of a plane algebraic quartic curve. It was illustrated that the novel method has great potential to model the plastic zone size.

Paper published

(a) Heike Arnolds, Anthony Kakoulli, Komalben Shah, Eann Patterson, Characterization of metal fatigue by optical second harmonic generation, Appl. Phys. Lett. 111, 131901 (2017)

Work in progress manuscript

(a) Observations on crack tip plastic zone size and shape, [1]Shah K, [2]Bond P, [2]James MN & [1]Patterson EA, [1]Department of Mechanical, Aerospace and Materials Engineering, University of Liverpool, [2]School of Engineering, University of Plymouth

Table of Contents

List of Tables

List of figures

List of symbols

$\boldsymbol{a}$	=	Crack length, mm
$\boldsymbol{e}$	=	Surface emissivity, unit less
$\boldsymbol{E}$	=	Young's modulus, N/m^2
$\boldsymbol{G}$	=	Strain energy release rate, J/m^2
$\Delta\boldsymbol{K}$	=	Stress intensity factor range ($\boldsymbol{K_{max} - K_{min}}$), MPa·√m
$\boldsymbol{m}$	=	Paris empirical exponent, unit less
$\boldsymbol{n}$	=	strain hardening exponent, unit less
$\boldsymbol{r_p}$	=	Radius of crack tip plastic region, mm
$\boldsymbol{A}$	=	Thermoelastic calibration constant, MPa/TS
$\boldsymbol{C\varepsilon}$	=	Specific heat at constant strain, J/Kg·K
$\boldsymbol{Cp}$	=	Specific heat at constant pressure, J/Kg·K
$\boldsymbol{K_I}$	=	Mode I stress intensity factor, MPa·√m
$\boldsymbol{K_{II}}$	=	Mode II stress intensity factor, MPa·√m
$\boldsymbol{N}$	=	Number of cycles, cycles
$\boldsymbol{Q}$	=	Heat Input, Cal.
$\boldsymbol{R}$	=	Ratio of $\boldsymbol{\sigma_{min}}$ to $\boldsymbol{\sigma_{max}}$, unit less

$\boldsymbol{S}$	=	Thermoelastic signal, TS
$\boldsymbol{S_{max}}$	=	Max thermoelastic signal per row of pixels, TS
$\boldsymbol{T}$	=	Absolute temperature, °C
$\boldsymbol{\alpha}$	=	Linear coefficient of thermal expansion, K^{-1}
$\boldsymbol{\varepsilon ij}$	=	Strain tensor, μ-strain
$\boldsymbol{\rho}$	=	Density, kg/m3
$\boldsymbol{\sigma ij}$	=	Stress tensor, MPa
σ_1 & σ_2	=	Principal stress, MPa
$\boldsymbol{\sigma_y}$	=	Yield stress, MPa
$\boldsymbol{\nu}$	=	Poisson Ratio, unit less
$\boldsymbol{\varphi}$	=	Phase angle, degrees
$\boldsymbol{\Delta T}$	=	Temperature change, °C
$\boldsymbol{\Delta \varphi}$	=	Change in phase angle, degrees

Abbreviations

3D-XRD	Three-Dimensional X-Ray Diffraction
BET	Backscattered Electron Topography
BSEIA	Back Scattered Electron Image Analysis
C-NIC	Circular - Nomarski Interference Contrast
CT	Compact Tension
DCB	Double Cantilever Beam
DFT	Discrete Fourier Transform
DIC	Digital Image Correlation
EBSD	Electron Back-Scattered Diffraction
ECCI	Electron Channelling Contrast Imaging
EDS	Energy Dispersive x-ray Spectroscopy
EIA	Energy Information Administration
FE-SEM	Field Emission Gun Scanning Electron Microscope
FFT	Fast Fourier Transform
FWHM	Full Width at Half Maximum
MPODM	Multi-Point over Deterministic Method

MT	Middle Tension
TEM	Transmission Electron Microscope
TSA	Thermoelastic Stress Analysis
SACP	Selected Area Channel Pattern
SEI	Secondary Electron Images
SSY	Small Scale Yielding

Chapter 1

Introduction

1.1 Motivation and aims of the research

The consumption of energy has increased rapidly for the past few years. Fossil fuels are the principal energy source which are finite and will run out over the next few centuries if used at the current rate [1]. Thus it is necessary to find ways to either replace fossil fuels as a source of energy by renewable energy resources or ensure efficient usage of fossil fuels. In addition to being finite, fossil fuels emit CO_2 on combustion, which contributes to global warming and a raised carbon footprint. According to Renewable Energy Research Brief 2015, the transport sector accounts for about 23% of annual global energy-related CO_2 emissions. There was 120% rise during the 1970s [2]. The Energy Information Administration (EIA) 2016 states that most of the energy in UK (83%) was produced by consuming fossil fuels (petroleum (36%), natural gas (33%) and coal (14%)). The transportation and industrial sectors account for more than 90% of petroleum consumption. Demand for diesel and aviation fuel is continuously increasing [3]. So it is a priority to find ways to utilize the available resources of fossil fuels more efficiently to save fossil fuels for future generations and to reduce the ecological footprint by enabling more sustainable, reliable and safer designs of components associated with power generation and transportation, including aerospace. Technological measures to reduce fossil fuel dependence in transport sector can be supplemented by a range of strategies including,

1) Smaller engines that burn lesser fuel, hybrid engines that uses less fuels and emit less CO_2, smarter engines that ensure complete combustion of fuel minimizing any scavenging.

2) Reducing the weight of structures (composite materials) in manufacturing of the parts without compromising the safety to improve fuel efficiency.
3) Improving the design of vehicles (motor vehicles, railed vehicles, watercraft, aircraft) to produce less aerodynamic drag
4) Regular inspection, maintenance and repair of components. Frequent examination of components for fatigue cracks as it is one of the primary damage mechanism of structural components [4, 5].

The first three technological measures are applicable before manufacturing of components at the design stage, while the last measure is applicable to components which are currently in service. Many engineers and researchers around the world are working on methods to reliably predict fatigue crack growth to perform necessary repair and to estimate post-damage life to forecast when the component should be removed from service [6].

Fatigue is progressive and localised structural damage that occurs when a material is subjected to repeatedly applied loads [7]. A disastrous fatigue failure could lead to economical outage, environmental damage, fatalities and liability problems. Fatigue also limits the service life of components. The first attempt to identify fatigue was made in the eighteenth century by Wilhelm Albert, since then there has been impressive progress in the field [8]. In the 19^{th} and 20^{th} centuries several serious fatigue failures were reported including fatigue failures of machinery, moving vehicles, welded structures, aircrafts, trains, pressure vessels, bridges etc. For example, in 1989, United Airlines Flight 232 lost its tail engine due to fatigue failure in a fan disk hub leading to death of 111 people [9]. The Hatfield rail crash in 2000 was caused by rolling contact fatigue (defined as multiple surface-breaking cracks). The steel rails of the tracks were subjected to metal fatigue caused by the passage of trains. Repeated loading caused fatigue cracks to grow and when they reached a critical size, the rail failed [10]. The

investigation of these failed structures revealed that failure began with microscopic cracks. These cracks may be the result of material imperfections, design discontinuities, unexpected loading, thermal stress or fatigue. Amongst these, fatigue is the main cause of crack growth resulting in structural failure [11]. So, knowledge of fatigue crack growth is important for structural integrity.

Fatigue cracks initiate due to the movement of dislocations forming persistent slip bands leading to crack nucleation, micro-crack growth and ultimate failure. Fatigue life consists of two periods, a crack initiation period and a crack growth period. Fatigue prediction methods are different for these two periods. The stress concentration factor K_t is used for predictions of crack initiation while the stress intensity factor range ΔK is used for predictions of fatigue crack growth, where ΔK is the difference between the maximum and minimum stress intensity factors during a particular loading cycle ($\boldsymbol{\Delta K = K_{max} - K_{min}}$). The stress intensity factor, $\boldsymbol{K}$ gives the magnitude of elastic stress field and represents the stress distribution around the crack tip. It is a function of specimen geometry, size and the length of the crack and the loading configuration [12]. The Paris law is the most popular fatigue crack growth life prediction model which relates the stress intensity factor range ($\boldsymbol{\Delta K}$) to the crack growth rate per cycle ($\boldsymbol{da/dN}$) for Small Scale Yielding (SSY) conditions (when plastic zone at crack tip is small in comparison with the crack length) [13]. The law assumes that (i) material is uniformly homogeneous, which is unrealistic, and (ii) crack tip stress and strain are independent of specimen thickness, which is not correct. In theory, Paris's law holds only when the crack propagation is controlled by elastic deformation occurring around the crack tip. However, plastic deformation is always present in the vicinity of a stressed crack tip in ductile metal materials. The fatigue fracture is significantly affected by the plastically deformed zone around the crack tip known as the plastic zone. Plastic zone size depends on variables such as yield stress, applied stress, specimen thickness and crack geometry and so it has clear physical

interpretation to describe fatigue crack propagation [14]. The size of the plastic zone is useful for structural analysis because it gives the estimate of how the material behaves when subjected to stress. During the SEM experiments, Davidson observed that, fatigue stress cycle results in many low level acoustic emissions; however the advance of the crack front through the plastic zone causes significant bursts of acoustic emission. By using appropriate sensors, this phenomenon can be used for structural health monitoring [15]. The estimation of the size of the plastic zone can be used to analyse how a material will react within itself when it is plastically deformed, which could give rise to fracture. The size of the plastic zone (when compared with crack length) indicates whether the SSY condition is satisfied or not. Hanh and Rosenfield characterised the plane stress and plane strain plastic zones using etching technique and concluded that it is possible to predict the stress state (plane stress vs plane strain) from the plastic zone shape [16]. In conclusion, plastic zone plays a vital role in crack growth therefore it is important to characterise the plastic zone of a fatigue crack tip.

Several models have been proposed by researchers to model the extent of the crack tip plastic zone including the pioneering work of Irwin [17] and Dugdale [18]. According to Irwin, the extent of the plastic zone r_p ahead of the crack tip is proportional to the square of the stress intensity factor,

$$\boldsymbol{r_p = \frac{1}{\pi}\left[\frac{\Delta K_I}{\sigma_y}\right]^2} \qquad \textbf{[1.1]}$$

where, ΔK_I is the range of the stress intensity factor and σ_y is the yield stress. He made several assumptions such as he considered the material to be elastic-perfectly plastic i.e. stresses cannot exceed the yield stress σ_y, and the value of strain hardening exponent n=0. Irwin analysed the situation along the x-axis only and considered the plastic zone shape to be circular (Fig 1.1(i)). There is no priori reason why the plastic zone should be circular [19].

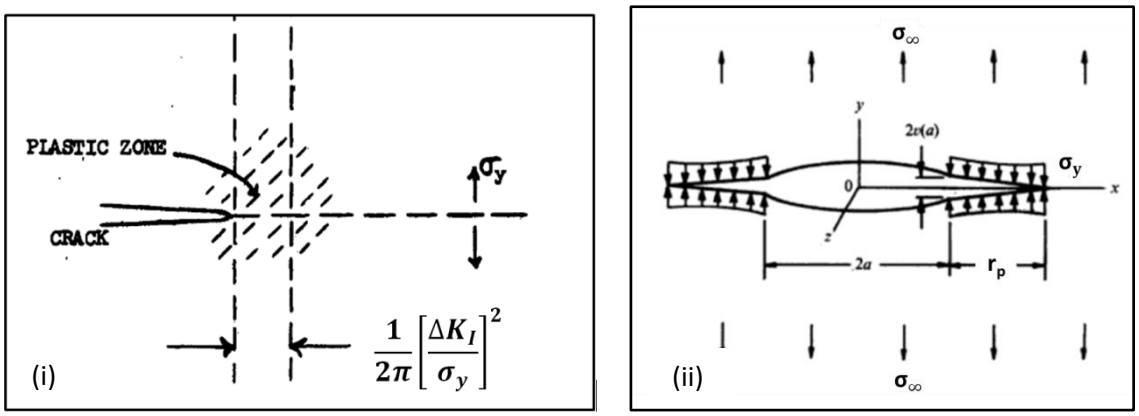

Fig 1.1: A schematic representation of (i) Irwin and (ii) Dugdale plastic zone model [15,16]

Dugdale followed a different approach to find the plastic zone extent. In Dugdale's Strip-Yield model, the plastic zone is envisioned as a narrow strip which extends a distance r_p ahead of the crack tip (Fig 1.1(ii)) [16]. This type of behaviour occurs for few materials particularly, when value of strain hardening exponent n ≈ 0, such as annealed mild steel, polymers), but not for all materials [20].

The Dugdale plastic zone size equation is,

$$r_p = \frac{\pi}{8}\left[\frac{\Delta K_I}{\sigma_y}\right]^2 \qquad \textbf{[1.2]}$$

Irwin and Dugdale both assumed an elastic-perfectly plastic material response. But for strain-hardened materials, less stress redistribution occurs at the crack tip and as a result the plastic zone size would be smaller. The behaviour of plastic zones in strain hardening materials subject to mode I loading under small-scale yielding (SSY) conditions are given by Hutchinson (1968) and by Rice and Rosengren (1968) and are known as HRR singularities [21, 22]. This analysis was extended by Shih for mixed mode loadings [23]. He obtained an elastic-plastic solution for combined mode I and mode II fatigue cracks as a function of value of strain hardening exponent n and plotted the plastic zone contours as shown in Fig 1.2.

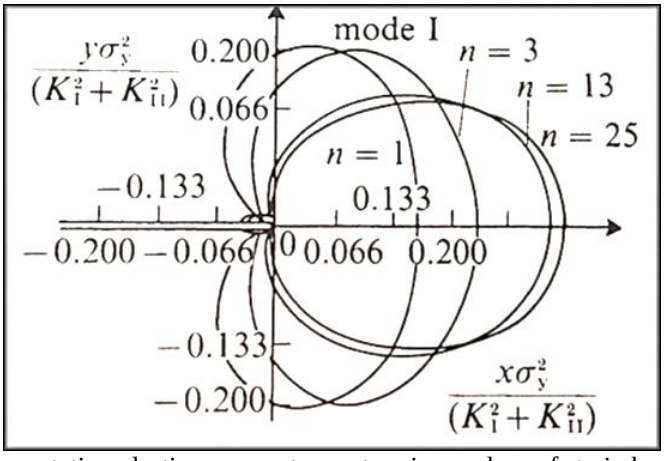

Fig 1.2: A schematic representation plastic zone contours at various values of strain hardening exponent by Shih

The n is strain hardening exponent in a Ramberg-Osgood representation of elastic-plastic constitutive behaviour represented by [24]

$$\boldsymbol{\varepsilon = \frac{\sigma}{E} + \left(\frac{\sigma}{A}\right)^n} \qquad \textbf{[1.3]}$$

where, ε is the uniaxial strain, $\boldsymbol{\sigma}$ is uniaxial stress, E is Young's modulus and $\boldsymbol{A}$ is a monotonic strength coefficient. Here, n= 1 for a linear elastic material and n=∞ for an elastic-perfectly plastic material. The value of n is determined by performing a linear regression on a log-log plot of stress vs strain. Despite of numerous studies, using analytical and numerical approaches, having been carried out [25-31], these plastic zone contours at various values of strain hardening exponent have never been demonstrated experimentally. The purpose of this research is to fill that gap by experimentally characterizing the plastic zone of a fatigue crack for different values of strain hardening exponent. The plastic zone has been estimated analytically by following Hutchinson's theory (1971) and results are compared with Shih's numerical predictions (1973) [21, 23]. Experimental plastic zone have been compared with the numerical predictions of Shih.

Another significant limitation of the Irwin and Dugdale plastic zone models is that their analyses are for ideal mathematical cracks which do not experience "crack closure". The concept of crack-closure was discovered by Elber in 1970, when he observed that fatigue-crack surfaces contact each other even during tension-tension cyclic loading [32]. He suggested that

a zone of residual plastic deformation is left in the wake of a fatigue crack. The crack does not open unless the applied load is enough to overcome this residual compressive stress present in the plastic wake zone. This plasticity induced crack closure will decrease the fatigue crack growth rate by reducing the effective stress intensity range ΔK_{eff} [32]. Since the discovery of plasticity-induced fatigue-crack closure, several other sources of crack closure including viscous-fluids [33] phase transformation [34], oxides [35] and roughness [36] in the crack flanks have been identified. The mechanisms of crack closure are complicated and not fully understood. Enormous experimental investigations, numerical analysis and analytical studies have been conducted to determine the effect of thickness, specimen geometry, stress state and loading condition on crack closure [37-48]. However, the effect of values of strain hardening exponent on fatigue crack closure is poorly understood and not validated experimentally. In the current project, experiments were carried out to investigate the effect of the value of strain hardening exponent on crack closure. In order to have range of value of strain hardening exponent, Pure Titanium, Al 2024-T3 and Al 6061-T6 have been selected for the experiments. Another reason for choosing these materials is their extensive use in aerospace industry.

The life prediction of structural and mechanical components is complicated as they may be subjected to variable amplitude loading or occasional overload cycles during service. It has been known for over five decades that overload cycles of sufficient magnitude can result in crack growth retardation or arrest [49-69]. Several different mechanisms have been proposed to explain the crack growth retardation following an overload [56]. These proposed mechanisms are (i) crack tip blunting [53] (ii) residual compressive stresses close to crack tip [58] and the accompanying interactions between the crack tip and the yield zone [55, 56] (iii) crack tip strain hardening [57] (iv) crack closure due to residual plastic deformation in the crack wake of the advancing crack front [58, 60]. Among these mechanisms, the phenomenon of crack closure [57-60] and the extent of plastic zone directly ahead of the crack -tip [65] are the

most significant mechanisms in explaining post-overload transients supported by a large body of evidence [54-64]. In the current project, the experiments were carried out to investigate how the fatigue crack of strain hardened materials behave when subjected to overloads.

It is extremely difficult to give a proper description of plastic zone size and shape considering the combined influence of the state of stresses, modes of loading, the crack length, dislocation density, materials' properties and its dimensions. For this reason, models most widely known from literature have followed one of two approaches. Either they give an approximation of size with a selected shape, e.g. the Irwin and Dugdale approaches, or they give an impression of shape but retain the first size approximation as derived by Von Mises or Tresca yield criteria. The research to date has tended to focus on the extent of plastic zone parallel to the direction of the crack growth; however, little attention has been paid to modelling the plastic zone perpendicular to the direction of crack growth and to find the plastic zone area. The extent of the plastic zone, $\boldsymbol{r_p}$ is not a reliable measure as the shape of the plastic zone changes with specimens of different thickness and during different modes of crack growth. In addition, the plastic zone size is not similar in the direction parallel to crack growth and perpendicular to crack growth. To overcome these problems, the area of the plastic zone, that contains information about both size and shape, could be more reliable measure to use to predict the plastic work ahead of the crack tip instead of relying on either the size or shape of the plastic zone. In the current project a novel methodology has been proposed to model the plastic zone shape and to determine its area using a mathematical function. The plastic zone size and shape found using this novel model have been compared with experimental results and show a very good agreement.

To characterize the plastic zone at the macro scale, the Thermoelastic Stress Analysis (TSA) technique has been selected because it has the ability to measure full-field strain maps in a specimen accurately and reliably and it does not require priori knowledge of materials

property. To characterize the plastic zone at the micro scale, Back Scattered Electron image analysis (BSEIA) and Discrete Fourier Transformation (DFT) processing has been employed to measure the plastic strain distribution around a fatigue crack tip.

1.2 Objectives

The aim of the research was to characterise the plastic zone of a fatigue crack experimentally and numerically at various values of strain hardening exponent.

The main objectives of the project were,

(1) To characterise the experimental plastic zone at constant amplitude loading and during overload using two techniques named Thermoelastic Stress Analysis (TSA) and Back Scattered Electron Image Evaluation (BSEIA) at macro scale and micro scale.

(2) To characterise the plastic zone at range of strain hardening exponents, n (n = 6, 8 and 14) to elucidate the effect of value of strain hardening exponent on plastic zone size and shape. To investigate the effect of plasticity-induced crack closure and overloads at various values of strain hardening exponent.

(3) To characterize the plastic zone using existing theories including Hutchinson (1971) and Shih (1973) [17, 19].

(4) To develop a novel method to characterize the plastic zone using a mathematical function.

1.3 Thesis structure

This thesis focuses on experimental characterisation of plastic zone to investigate the effect of value of strain hardening exponent on crack closure and overload crack growth retardation.

Chapter 2 reviews different techniques to characterise the plastic zone experimentally and numerically. This chapter also reviews the literature regarding the effect of plasticity-

induced crack closure and overloads. Finally this chapter compares two widely used full-field stress fields (TSA – Thermoelastic Stress Analysis) and displacement fields (DIC- Digital Image Correlation) techniques to choose the most suitable technique to characterise the plastic zone.

Chapter 3 presents the literature survey of the most commonly used mathematical models characterising the stress fields ahead of the crack tip. The plastic zone shape proposed by Von Mises is described. Following this, the phenomena of fatigue crack closure is discussed.

Chapter 4 reveals why the particular materials are selected for the experiments. It also describes the procedure to prepare the specimens for the experiments. Finally, the principles of TSA (Thermoelastic Stress Analysis) and BSEIA (Back Scattered Electron Image Analysis) techniques, equipment used and the process to characterise the plastic zone from the data is described.

Initially, Chapter 5 lists the results from TSA technique. It also discusses the effect of a value of strain hardening exponent on plastic zone size and shape, plasticity-induced crack closure and overloads. Subsequently, it shows the results from BSEIA technique for a strain hardening exponent, n=6. Next, it explores the BSEIA technique's sensitivity to the overload. This chapter then discusses the applicability of BSEIA technique to the materials of value of strain hardening exponent, n = 8 and n = 14. It also explores novel method to recognise the plasticity from BSE images using the statistical information of image. Finally, it proposes the usefulness of Circular - Nomarski Interference Contrast (C-NIC) microscopy in absence of Field Emission Gun Scanning Electron Microscope (FE-SEM).

Chapter 6 compares the experimental plastic zone with the numerical plastic zone proposed by previous researchers. This chapter then discusses the plastic zone achieved by

author by following Hutchinson's methodology [17]. Finally, it reveals the novel method to model the plastic zone using a mathematical function.

Chapter 7 draws the major conclusions of this thesis, and recommendation for future work is covered in chapter 8.

Chapter 2

Theory & Literature Review

To predict the service life of components subjected to cyclic loading, accurate detection and characterization of fatigue crack growth is essential. To characterise the fatigue crack growth, the range of stress intensity factor and the crack tip plastic zone have been established as the most suitable and widely accepted parameters in the fracture mechanics [69]. Information about the crack tip plastic zone can be very useful for evaluating the components used in power plants, oil refineries and transportation including aviation industry. For these reasons, there has been a great deal of research interest in the size and shape of the crack tip plastic zones as means of characterizing crack tip plastic deformation. Many aspects contribute to the catastrophic growth of fatigue cracks such as specimen geometry, stress state, loading condition and strain hardening capacity of materials [69-73]. A considerable amount of literature has been published detailing the effect of specimen geometry, stress state, loading conditions and specimen thickness on crack tip plasticity by analytical, numerical and experimental methods; however, only a few papers in the literature investigate the effect of strain hardening analytically and numerically yet there are no studies which experimentally demonstrate the effect of strain hardening on the plastic zone. In the current project, an experimental investigation was conducted to explore the effect of value of strain hardening exponent on the plastic zone. This chapter provides the insight of plastic zone and reviews different techniques to characterise the plastic zone.

A large and growing body of literature has investigated the effects of overloads on fatigue crack growth in the presence of crack closure, since the crack closure mechanism

(which modifies the stress intensity factor range experienced by the crack tip and hence the crack growth rate) has been recognised as a crucial phenomenon in the explanation of retardation due to overload [74-85]. A survey of the literature suggests that literature on the behaviour of strain hardened materials during overload is scarcely reported. In particular, the effect of the value of strain hardening exponent on overload remains unexplored. And to the best of author's knowledge, no report has found the effect of value of strain hardening exponent on the plastic zone during an overload. Therefore, another motivation for this study is to characterise the plastic zone for strain hardened materials during overload. This chapter also explains fatigue crack closure phenomena, effect of overload and provides a literature review for the same.

2.1 Linear Elastic and Elastic Plastic Fracture Mechanics

Fracture mechanics is the field of mechanics concerned with the study of the propagation of cracks in materials and the characterization of the material's resistance to fracture. The stress and the flaw size are the driving force of fracture and the fracture toughness is a measure of material's resistance to crack propagation. Fracture occurs when the driving force reaches or exceeds the material resistance. Several parameters are available for characterizing the fracture driving force i.e. energy release rate G, stress-intensity factor K, J integral and CTOD [14]. The appropriate driving force parameters for linear elastic materials are energy release rate G and stress intensity factor K while driving force parameters for elastic plastic regime are the J integral and CTOD [69].

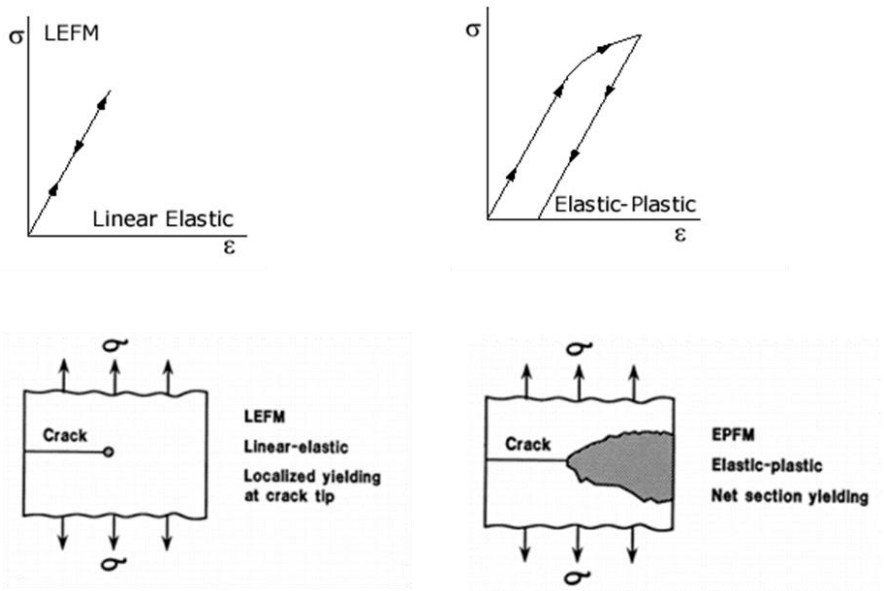

Fig 2.1 Linear Elastic Fracture Mechanics (LEFM) applies when the nonlinear deformation of the material is confined to a small region near the crack tip. Elastic Plastic Fracture Mechanics (EPFM) is proposed to analyse the relatively large plastic zones.

Fracture mechanics was developed during World War I by A. A. Griffith to explain the failure of brittle materials. He assumed that the work required to create new surfaces is proportional to the surface energy [86]. The growth of a crack requires the creation of two new surfaces and hence an increase in the surface energy. Irwin applied Griffith's theory to ductile material but it gave unrealistically high surface energies so he concluded that crack tip plasticity must be playing a significant role in ductile fracture [17]. In ductile material, a plastic zone develops at a crack tip, as applied load increases the plastic zone size increases until the crack grows and the material behind the crack tip unloads. During the plastic loading and unloading cycle near the crack tip, energy dissipates as heat and this additional energy needed for crack growth in ductile materials denoted by plastic dissipation $\boldsymbol{G_p}$. Irwin and his colleagues also found a method to calculate the amount of energy available for fracture in terms of asymptotic stress and displacement fields around a crack front in linear elastic solid represented by Fig 2.2.

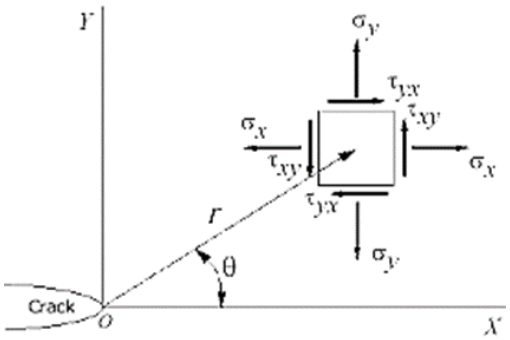

Fig 2.2 Crack tips produce a 1/√r singularity. The stress fields near a crack tip of an isotropic linear elastic material expressed as a product of 1/√r and a function of θ with a scaling factor K

The stress field around a crack tip is denoted by equation,

$$\boldsymbol{\sigma_{ij}} = \left(\frac{\boldsymbol{K}}{\sqrt{\boldsymbol{2\pi r}}}\right) \boldsymbol{f_{ij}(\theta)} \qquad \textbf{[2.1]}$$

Where, $\boldsymbol{\sigma_{ij}}$ is Cauchy stresses, $\boldsymbol{r}$ is the distance from crack tip, $\boldsymbol{\theta}$ is the angle with respect to the plane of the crack and $\boldsymbol{f_{ij}}$ are functions that depends on crack geometry and loading conditions. Irwin used the stress intensity factor *K* to quantify the crack tip driving force [17].

In 1961, Paris used the stress intensity factor range $\boldsymbol{\Delta K}$ to characterize the rate of crack advance per cycle to predict the crack growth rate as shown in Fig 2.3, which became known as Paris law [87].

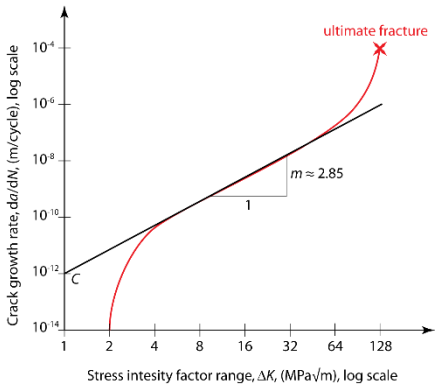

Fig 2.3: Schematic plot of the typical relationship between the crack growth rate and the range of the stress intensity factor [91].

$$\frac{\boldsymbol{da}}{\boldsymbol{dN}} = \boldsymbol{C\Delta K^m} \qquad \textbf{[2.3]}$$

where $\boldsymbol{a}$ is the crack length, $\boldsymbol{N}$ is the number of load cycles, $\boldsymbol{C}$ and $\boldsymbol{m}$ are material constants. Paris was the first to explain that during cyclic loading of a crack, there is a reverse cyclic

plastic zone near the crack tip, which was examined later by Rice [13, 88]. In the same year, Wells at the British Welding Institute proposed a crack-tip opening displacement (CTOD) parameter in order to extend the elastic stress intensity factor approach into elastic–plastic yielding conditions [89]. While examining the fractured surfaces, Wells noticed that the crack faces had moved apart prior to fracture and plastic deformation had blunted an initially sharp crack. The degree of crack blunting was proportional to the toughness of the material and so he proposed the opening at the crack tip as a measure of fracture toughness commonly known as CTOD (Crack Tip Opening Displacement), represented by $\boldsymbol{\delta}$.

$$\boldsymbol{\delta = \frac{4}{\pi}\frac{K_I^2}{\sigma_{ys}E}} \qquad \textbf{[2.4]}$$

where $\boldsymbol{K_I}$ is mode I stress intensity factor, $\boldsymbol{\sigma_{ys}}$ is yield stress and $\boldsymbol{E}$ is Young's modulus.

The path-independent and nonlinear energy release rate *J*-integral was proposed by Rice in 1968 to characterize the intensity of elastic–plastic crack-tip fields [22]. He showed that the value of the *J*-integral is equivalent to energy release rate in a nonlinear elastic material that contains a crack.

2.1.1 Small-Scale Yielding (SSY)

Conventional fracture mechanics has developed single parameters that seek to uniquely describe the displacement, strain and stress ahead of a crack. For materials that do not undergo plastic deformation, the single parameter is referred to as K. When plastic strain develops at the crack tip, the J-integral provides this single parameter. If plasticity remains well contained to the crack tip region and is not influenced by the size of the surrounding structure, then K and J are uniquely related such that [90],

$$\boldsymbol{K = \sqrt{\frac{EJ}{1-\nu^2}}} \qquad \textbf{[2.5]}$$

where E is the elastic modulus and ν is Poisson's ratio. This condition is referred to as Small Scale Yielding (SSY) since the plastic zone is small in comparison to the relative dimensions of the structure in which it is contained. As material toughness increases, the plastic zone at the crack tip increases in size and eventually interacts with the finite boundaries of the structure in which it is contained thus exceeding the SSY condition. BSISO standard 12108:2012 (Fatigue testing and Fatigue crack growth method for Metallic materials) states that specimen should remain predominantly in a linear-elastic stress condition throughout the test. For the Compact Tension (CT) specimens the minimum uncracked ligament for producing valid data are given by [91],

$$(\boldsymbol{W-a}) \geq \left(\frac{\boldsymbol{4}}{\boldsymbol{\pi}}\right)\left(\frac{\boldsymbol{K_{max}}}{\boldsymbol{R_{p0.2}}}\right)^{\boldsymbol{2}} \qquad \textbf{[2.6]}$$

where, W is width of the CT specimen, a is crack length, K_{max} is maximum stress intensity factor and $R_{p0.2}$ is 0.2 % proof strength at the test temperature. In order to fulfil the SSY condition, in a current research, the dimensions W and a are chosen in a way that all the fatigue tests satisfies the equation [2.6]. This also allows the comparison of measured plastic zone sizes to the Irwin's and Dugdale's plastic zone.

2.2 Plastic Zone

In order to understand plastic zone, it is important to understand the stress and deformation fields near the tips of cracks based on the linear elastic analysis of crack tip fields. The stress field around a mode I crack tip can be described by a set of linear elastic field equations. Fig 2.4 represents the 2D Infinitesimal element showing the variation of Cartesian components of the stresses on the various faces.

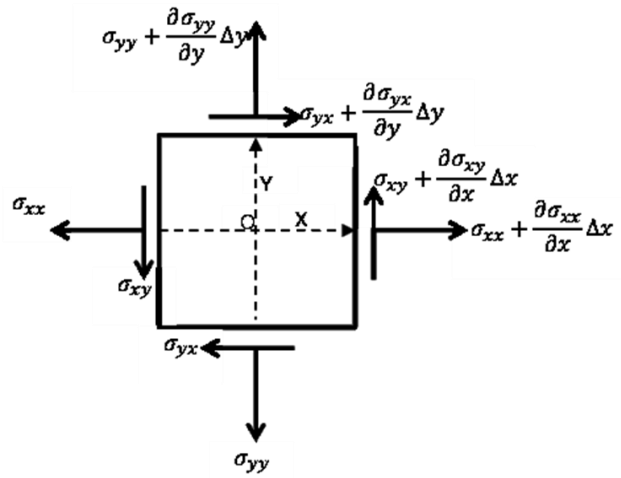

Fig 2.4: 2D Infinitesimal element showing the variation of Cartesian components of the stresses [14]

The equilibrium equations for rectangular Cartesian coordinate can be written as:

$$\frac{\partial \sigma_x}{\partial x} + \frac{\partial \sigma_{xy}}{\partial y} = 0 \qquad [2.7]$$

$$\frac{\partial \sigma_{xy}}{\partial x} + \frac{\partial \sigma_y}{\partial y} = 0 \qquad [2.8]$$

And the compatibility equation:

$$\nabla^2(\sigma_x + \sigma_y) = 0 \qquad [2.9]$$

Where,

$$\nabla^2 = \frac{\partial^2}{\partial x^2} + \frac{\partial^2}{\partial y^2}$$

According to the theory of plane elasticity, for two-dimensional continuous elastic medium, the stresses can be derived from a function $\boldsymbol{\Phi}$ (x, y):

$$\sigma_x = \frac{\partial^2 \Phi}{\partial y^2}, \qquad \sigma_y = \frac{\partial^2 \Phi}{\partial x^2}, \qquad \sigma_{xy} = -\frac{\partial^2 \Phi}{dx\, dy} \qquad [2.10]$$

$\boldsymbol{\Phi}$ is known as an Airy stress function which was first introduced by Airy in 1862 [92],

The stress sum of equation [2.10] can be written as:

$$\sigma_x + \sigma_y = \nabla^2 \Phi \qquad [2.11]$$

Substituting equation [2.10] in to equation [2.9], the compatibility equation can be written as:

$$\frac{\partial^4 \Phi}{\partial x^4} + 2\frac{\partial^4 \Phi}{\partial x^2 \partial y^2} + \frac{\partial^4 \Phi}{\partial y^4} = 0 \qquad [2.12]$$

Or

$$\nabla^4(\Phi) = \nabla^2[\nabla^2(\Phi)] = 0 \quad \textbf{[2.13]}$$

Equation [2.12] and [2.13] are called the Biharmonic equation and its solutions are called Biharmonic functions. Every function $\Phi(x, y)$ that fulfils equation [2.13] is called an Airy stress function. The commonly used forms of stress field equations are Westergaard stress field equation and Muskhelishvili's complex representation of the stress field [14].

2.2.1 The Westergaard stress field

In 1939, Harold M. Westergaard developed a solution for the stress field surrounding a crack. Westergaard introduced a complex stress function ***Z(z)*** to analyse stresses in crack bodies, where $z = x + iy$ and $i = \sqrt{-1}$. The relationship between Westergaard stress function and the Airy stress function is given as follows [93],

$$\Phi = Re \iint z + yIm \int z \quad \textbf{[2.14]}$$

Where Re and Im denote the real and imaginary parts of the function respectively, and represents the integration with respect to z.

Substituting equation [2.14] into equation [2.10] gives,

$$\begin{aligned} \sigma_x &= ReZ - yImZ' \\ \sigma_y &= ReZ + yImZ' \\ \sigma_{xy} &= ReZ - yImZ' \end{aligned} \quad \textbf{[2.15]}$$

When $y = 0$, the imaginary parts of σ_x and σ_y and the shear stress σ_{xy} vanish which indicates that the crack plane is a principle plane. Therefore, the stresses are symmetric about the crack plane, i.e. $\theta = 0$ and equation [2.15] implies mode I loading.

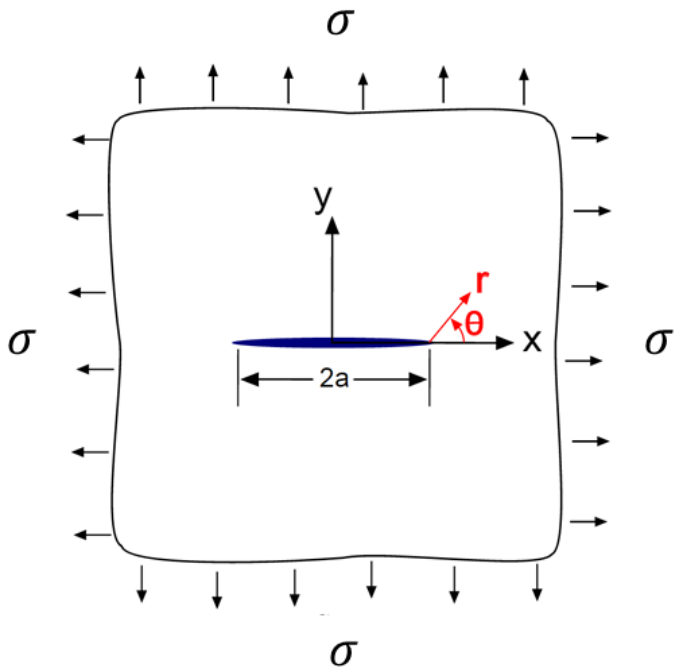

Fig 2.5: Through-thickness crack in an infinite plate loaded in biaxial tension [14]

Considering a through crack in an infinite plate subjected to biaxial remote tension, if the origin of the coordinate system is defined at one of the crack tips of the crack, as shown in Fig 2.6, the Westergaard stress function can be given as,

$$\boldsymbol{Z(z) = \frac{K_I}{\sqrt{2\pi z}} \;\; , \; K_I = \sigma\sqrt{\pi a}} \qquad \textbf{[2.16]}$$

Where $\boldsymbol{\sigma}$ is the remote stress and $\boldsymbol{a}$ is the half crack length. Substituting equation [2.10] into equation [2.15], stress fields can be expressed as,

$$\boldsymbol{\sigma_x = \frac{K_I}{\sqrt{2\pi r}}\left[\frac{5}{4}cos\left(\frac{\theta}{2}\right) - \frac{1}{4}cos\left(\frac{3\theta}{2}\right)\right]} \qquad \textbf{[2.17a]}$$

$$\boldsymbol{\sigma_y = \frac{K_I}{\sqrt{2\pi r}}\left[\frac{3}{4}cos\left(\frac{\theta}{2}\right) + \frac{1}{4}cos\left(\frac{3\theta}{2}\right)\right]} \qquad \textbf{[2.17b]}$$

$$\boldsymbol{\sigma_{xy} = \frac{K_I}{\sqrt{2\pi r}}\left[\frac{1}{4}sin\left(\frac{\theta}{2}\right) + \frac{1}{4}sin\left(\frac{3\theta}{2}\right)\right]} \qquad \textbf{[2.17c]}$$

2.2.2 Mode I stress field equations in terms of principle stresses

The derivation of mode I stress field equation in terms of principle stresses can be derived from a Mohr's circle construction as shown in Fig 2.6 [90],

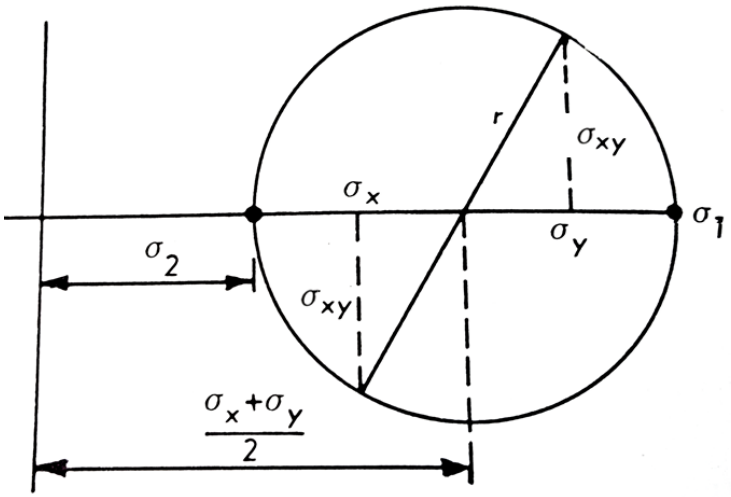

Fig 2.6: Mohr's circle construction [90]

From the Fig 2.6 it is seen that,

$$\boldsymbol{\sigma_{1,2} = \frac{\sigma_x+\sigma_y}{2} \pm r} \qquad \textbf{[2.18]}$$

where,

$$\boldsymbol{r = \sqrt{\frac{(\sigma_y-\sigma_x)^2}{2} + \sigma_{xy}^2}} \qquad \textbf{[2.19]}$$

So that

$$\boldsymbol{\sigma_{1,2} = \frac{\sigma_x+\sigma_y}{2} \pm \sqrt{\frac{(\sigma_y-\sigma_x)^2}{2} + \sigma_{xy}^2}} \qquad \textbf{[2.20]}$$

Substitution of equation [2.17a], [2.17b] and [2.17c] in equation [2.20] gives,

$$\boldsymbol{\sigma_1 = \frac{K_I}{\sqrt{2\pi r}} cos\frac{\theta}{2}\left(1 + sin\frac{\theta}{2}\right)} \qquad \textbf{[2.21a]}$$

$$\boldsymbol{\sigma_2 = \frac{K_I}{\sqrt{2\pi r}} cos\frac{\theta}{2}\left(1 - sin\frac{\theta}{2}\right)} \qquad \textbf{[2.21b]}$$

$\boldsymbol{\sigma_3 = 0}$ for plane stress or $\boldsymbol{\sigma_3 = \nu(\sigma_1 + \sigma_2)}$ for plane strain **[2.21c]**

2.3 Plastic zone shape

The Irwin and Dugdale approaches model explained earlier consider only the crack plane $\boldsymbol{\theta}$=0 and it was assumed that the zone was of a circular shape or a strip shape. A more accurate impression of its shape can be obtained by examining the yield condition. It is possible to estimate the extent of plasticity at all angles around the crack tip by using a yield criterion to the Westergaard crack tip stress field equations 2.8. There are two well-known yield criteria often cited in literature i.e. von Mises and Tresca yield criteria [90]. Only the Von Mises criterion is discussed here as it is employed to describe the shape of the plastic zone in following chapters.

2.3.1 Von Mises yields criteria

According to von Mises's criterion also known as the maximum distortion energy criteria (i.e. the energy associated with changes in the shape of the material), yielding of a material begins when the maximum distortion/shear energy in the material equals the maximum distortion/shear energy at yielding in a simple tension test denoted by,

$$(\boldsymbol{\sigma_1 - \sigma_2})^2 + (\boldsymbol{\sigma_2 - \sigma_3})^2 + (\boldsymbol{\sigma_3 - \sigma_1})^2 = \boldsymbol{2{\sigma_{ys}}^2} \qquad \textbf{[2.22]}$$

where $\boldsymbol{\sigma_1}$, $\boldsymbol{\sigma_2}$ and $\boldsymbol{\sigma_3}$ are principle stresses. In previous section, the mode I stress field equations were derived in terms of the principle stresses, namely,

$$\boldsymbol{\sigma_1 = \frac{K_I}{\sqrt{2\pi r}} cos\frac{\theta}{2}\left(1 + sin\frac{\theta}{2}\right)} \qquad \textbf{[2.23a]}$$

$$\boldsymbol{\sigma_2 = \frac{K_I}{\sqrt{2\pi r}} cos\frac{\theta}{2}\left(1 - sin\frac{\theta}{2}\right)} \qquad \textbf{[2.23b]}$$

$$\boldsymbol{\sigma_3 = 0\ for\ plane\ stress\ or\ \ \sigma_3 = \nu(\sigma_1 + \sigma_2) for\ plane\ strain} \qquad \textbf{[2.23c]}$$

Substitution of equations [2.23a], [2.23b] and [2.23c] in equation [2.20] for plane stress results in,

$$\frac{{K_I}^2}{2\pi r}\left(1+\frac{3}{2}sin^2\theta+cos\theta\right)={2\sigma_{ys}}^2$$

Or $$r(\theta)=\frac{1}{4\pi}\left(\frac{K_I}{\sigma_{ys}}\right)^2(1+\frac{3}{2}sin^2\theta+cos\theta) \quad \textbf{[2.24]}$$

Equation 2.24 can be converted to dimensionless by dividing by r_p, the first order approximation to plastic zone size for θ=0, representing for plane stress,

$$\frac{r(\theta)}{r_p}=\frac{1}{2}+\frac{3}{4}sin^2\theta+\frac{1}{2}cos\theta \quad \textbf{[2.25]}$$

Figure 2.7 shows the shape of the plane stress and plane strain plastic zones in dimensionless form found using equation [2.25].

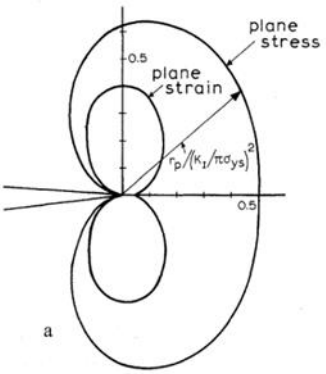

Fig 2.7: Plastic zone shapes according to Von Mises's yield criteria [90]

2.4 Plastic zone at various values of strain hardening exponent

Strain hardening exponent, represented by "n", approximates the relation between true stress and true strain during plastic deformation of a metal. Whenever stress is applied, number of dislocation increases in slip plane (Planes on which dislocation takes place, Fig 2.8) so enthalpy of lattice increases. When a metal is plastically deformed, dislocations move and

additional dislocations are generated. The more the dislocations in material, the more they will interact. As the dislocation density increases, the movement of the dislocations decreases and become pinned or tangled resulting in increasing random orientation between atomic planes. Due to random orientation of these planes movement of dislocation motion gets blocked at the barrier, such as a grain boundary, sub grain boundary, tangled cell, second phase etc. hence slip planes get arrested. This will result in a decrease in the mobility of the dislocations resulting in increased resistance to permanent deformation. So strength and hardness of material will increase and ductility will decrease. This increase in strength and hardness is known as strain hardening [94]. Materials with higher n values will have smaller plastic zone and will elongate more before fracture takes place.

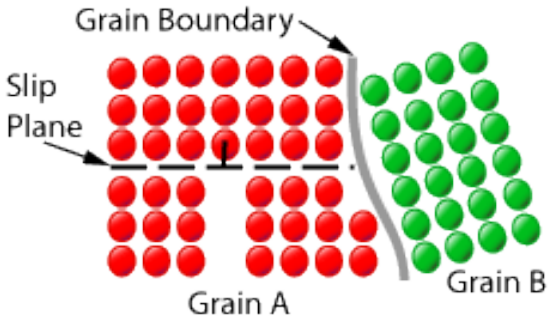

Fig 2.8 Characterization of a dislocation (Edge dislocation)

In 1968, Hutchinson [21] and Rice and Rosengren [22] independently evaluated the character of crack-tip stress fields in the case of strain hardening materials for both plane stress and strain and only for plane strain conditions respectively. Hutchinson, Rice and Rosengren showed that the strength of the near-tip field is the J-integral and the stresses, strain and displacements exhibit $\boldsymbol{r^{-1/(n+1)}}$, $\boldsymbol{r^{-n/(n+1)}}$ and $\boldsymbol{r^{1/(n+1)}}$ singularities, respectively. Equations (2.26-2.28) are known as HRR singularity fields for stress, strain and displacement fields respectively.

$$\boldsymbol{\sigma_{ij}} = \boldsymbol{\sigma_y}\left(\frac{\boldsymbol{J}}{\boldsymbol{\alpha\sigma_y\epsilon_y I_n r}}\right)^{\frac{1}{n+1}} \boldsymbol{\tilde{\sigma}_{ij}(\theta, n)} \quad \textbf{[2.26]}$$

$$\boldsymbol{\epsilon_{ij}} = \boldsymbol{\alpha\epsilon_y}\left(\frac{\boldsymbol{J}}{\boldsymbol{\alpha\sigma_y\epsilon_y I_n r}}\right)^{\frac{n}{n+1}} \boldsymbol{\tilde{\epsilon}_{ij}(\theta, n)} \quad \textbf{[2.27]}$$

$$\boldsymbol{u_i} = \boldsymbol{\alpha\epsilon_y}\left(\frac{\boldsymbol{J}}{\boldsymbol{\alpha\sigma_y\epsilon_y I_n r}}\right)^{\frac{n}{n+1}} \boldsymbol{r^{1/(n+1)}\, \tilde{u}_i(\theta, n)} \quad \textbf{[2.28]}$$

In the above equations, the dimensionless constant $\boldsymbol{I_n}$ and the dimensionless angular functions $\boldsymbol{\tilde{\sigma}_{ij}(\theta, n)}$, $\boldsymbol{\tilde{\epsilon}_{ij}(\theta, n)}$ and $\boldsymbol{\tilde{u}_i(\theta, n)}$ vary with the polar angle θ, the strain hardening exponent n and the state of stress (plane stress or strain). The Hutchinson, Rice and Rosengren solutions for crack tip stress distribution are either applicable to mode I loading or mode II loading conditions and not for combined loading conditions. The cracks in structural materials are however subjected to combined mode loading conditions. Using the HRR singularity as a foundation, Shih presented near-tip-fields solutions for mode I and mode II crack problems [23]. He characterised the stress intensity factors $\boldsymbol{K_I}$and $\boldsymbol{K_{II}}$ in terms of an elastic mixity parameter, $\boldsymbol{M^e}$ defined as,

$$\boldsymbol{M^e} = \frac{\boldsymbol{2}}{\boldsymbol{\pi}}\boldsymbol{tan^{-1}}\left(\lim_{\boldsymbol{r\to 0}} \frac{\boldsymbol{\sigma_{\theta\theta}(r,\theta=0)}}{\boldsymbol{\sigma_{r\theta}(r,\theta=0)}}\right) = \frac{\boldsymbol{2}}{\boldsymbol{\pi}}\boldsymbol{tan^{-1}}\left|\frac{\boldsymbol{K_I}}{\boldsymbol{K_{II}}}\right| \quad \textbf{[2.29]}$$

Where, $\boldsymbol{M^e = 0}$ for pure mode II, $\boldsymbol{M^e = 1}$ for pure mode I and $0 < M^e < 1$ for different mixities of mode I and II. Shih plotted the plastic zone contours as a function of strain hardening exponent n for pure mode II (mixity parameter $M^e = 0$) and mode I (mixity parameter $M^e = 1$) for plane stress loading as shown in Fig 2.9. He noted that the effect of plasticity is more directly evident from the Fig 2.9(a) where the plastic zone size in mode II loading is up to five times bigger than that in mode I. He concluded that any deviation of a fatigue crack from the mode I growth plane leads to an increase in, not only stress intensity factors but also, in plastic zone size ahead of crack tip. Shih only compared the mode I and mode II plastic zone contours

size but he didn't comment on the change in shape of mode I plastic zone at varying value of strain hardening exponent as shown in Fig 2.9(b). It is evident from the Fig 2.9(b) that for n=1 and 3 the plastic zone shape is a cardiac but for n=13 and 25, the shape becomes circular for mode I crack growth.

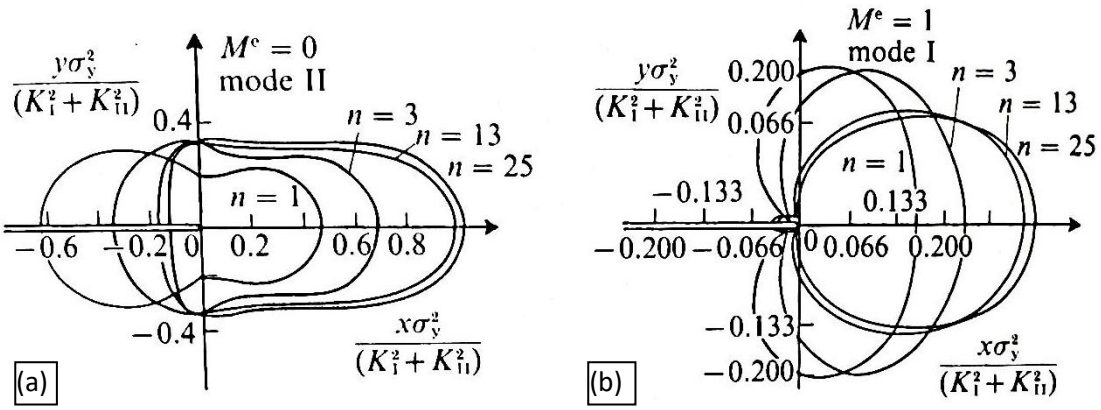

Fig 2.9: Contours of plastic zones for different values of strain hardening exponent n for mode I and mode II crack subjected to plane stress

To date, Shih's plastic zone contours at various values of strain hardening exponent have not been verified by experiments hence the in current research experimental plastic zones have been characterised at various value of strain hardening exponents.

2.5 Literature review on techniques to characterise the plastic zone

There are various tools and techniques available to experimentally measure the fatigue crack extension and plastic zone surrounding the fatigue crack as it is crucial for the determination of reliable crack growth rates. Some of these techniques include acoustic emission, electrical, and compliance methods [95]. Acoustic emission is a non-invasive technique that provides direct measurement of fatigue crack initiation and propagation with high sensitivity. The atomic rearrangement in materials and release of elastic strain energy during crack extension results in acoustic emissions [96]. Sensitive transducers located at the surface of the sample detect the sound waves. Each sensor output is amplified, filtered and analysed. Although acoustic emission has been used for about four decades, many problems

still exist such as it only gives a qualitative estimate of damage. So, other techniques are required to achieve quantitative results. Since the late 1950's, the eddy current method has been used for detecting surface cracks in aircraft structures and engines, and to obtain crack length and depth information. Portable eddy current instruments utilise phase or amplitude variations to estimate crack depth or length as the presence of a crack will change in the eddy currents. In eddy current measurements, there is always a compromise between high sensitivity at high frequencies and the ability to monitor deeper cracks at low frequencies [97].

Over the time, a substantial number of techniques have been developed to measure the plastic zone size at the crack tip. Micro hardness, etching, recrystallization and strain gauges are the classical techniques [98]. The micro hardness measurement technique involves taking hardness indentations ahead of or around a crack tip and determining the elastic-plastic boundary as a sudden variation in hardness [99, 100]. Hahn and Rosenfield used an etching technique and observed dark and light etched regions in deformed and undeformed regions of the material [98]. Even though the etching technique allowed direct measurement of the plastic zone size and shape, it is time consuming and etching conditions have to be determined separately for each material. The recrystallization method is based on the well-known principle that the recrystallization temperature depends on the amount of stored energy of deformation in a material. But this technique does not measure less than 2% deformation [101,102]. The deformed grain method is applicable to materials with very fine grains. The deformed grains are observed under an optical microscope and the change in the aspect ratios of the grains is used to calculate the amount of strain and the boundary of the plastic zone since the grains will be undeformed outside the plastic zone when a specimen is unloaded [98]. The strain gauge method can be used during an experiment but it has not been widely used to measure the strain field around the crack tip because of the finite dimensions of the gauges [103]. Due to this, the signal output represents the average strain over the gauge length and not to the specific point.

These measurements are very remote relative to the crack tip and their interpretation is not straightforward.

There are some non-contacting techniques that could be employed to find the plastic zone such as optical interference microscopy, moiré interferometry, laser speckle, diffraction peak broadening. Numerous investigators have utilised optical methods to characterize fatigue crack growth. In microscopy based optical method, a travelling microscope at 50x magnification is used to detect the crack growth. The crack length is measured as a function of cycles at intervals to obtain distribution of **da/dN** versus $\Delta \boldsymbol{K}$. The optical technique is simple, inexpensive and no calibration is required but it is time consuming and automation is expensive. This technique can only be performed if the specimen surface is easily accessible and free from corrosion or oxidation products [104]. Optical interference microscopy technique uses a laser beam to make direct measurements of the plastic zone based on out-of-plane deformations of the specimen but it requires a perfectly polished specimen without any discontinuity and with 95% reflectivity [105]. Chanani et al. used the optical interference microscopy technique to identify the crack growth behaviour as the crack progresses through the plastic zone under plane stress conditions, and they also confirmed that, the retardation occurs in the overload plastic zone during fatigue testing on a series of aluminium alloys [105].

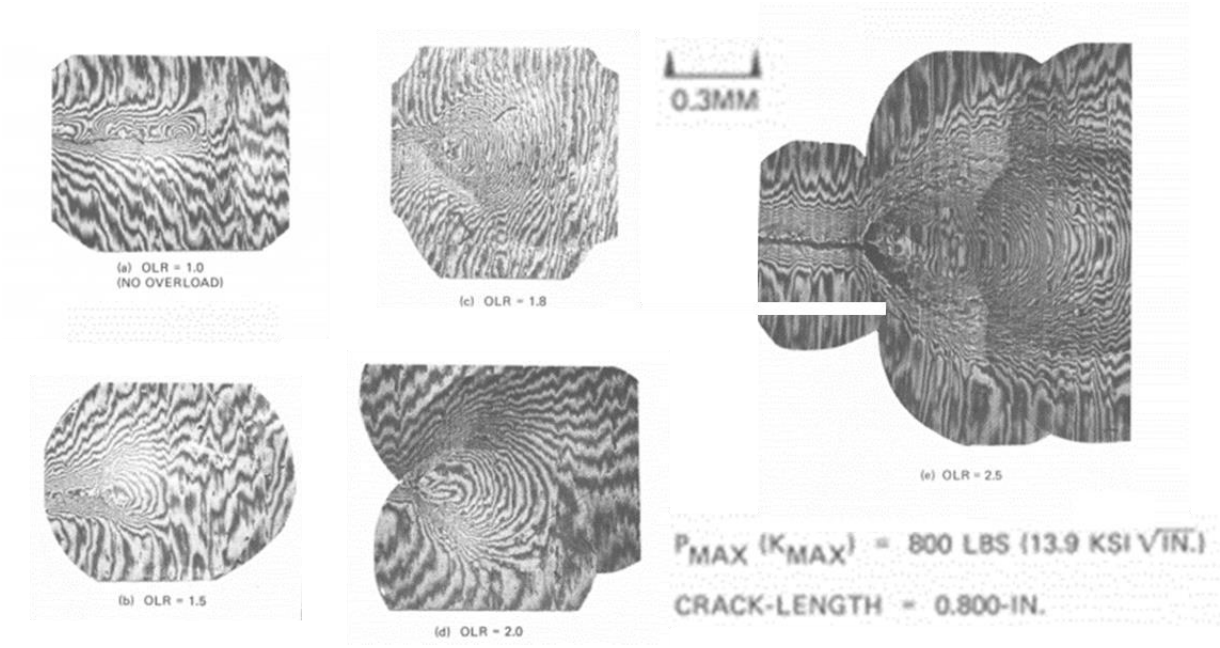

Fig 2.10: Optical interference patterns at the crack-tip of 7075-T6 SEN specimens after different overload cycles [105]

Geometric Moiré technique employs the principle of light interference which provides high enough sensitivity to measure small elastic strains by providing contour maps of in-plane displacement field; parallel and perpendicular to the crack. The technique is based on the interference of two regular gratings, a reference grating and a specimen grating. Simultaneous viewing of the two gratings produces an interference pattern known as fringes, which are contours of deformation perpendicular to the lines of the grating. Gianni employed Moiré technique in order to determine the extent of the monotonic plastic zone. The occurrence of cyclic plasticity upon unloading according to Rice's fatigue model was inferred from a sharp change in the type of deformation around a fatigue crack as shown in Fig 2.11. It was demonstrated that, quantitative observations of plastic zone size in front of the crack tip were consistent with Rice's estimate of the monotonic plastic zone size [106].

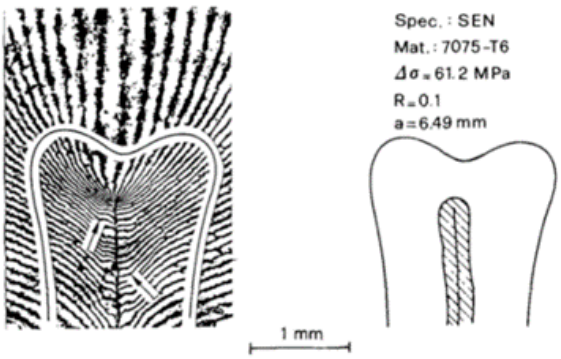

Fig 2.11: Live load *V*-displacement field and cyclic plastic zone boundary at x=0 [106]

In 1995 Tay et al. employed a laser speckle technique to measure the plastic zone which was first observed by Azushima in 1982. It is based on the phenomenon that plastic deformation changes metallic surface roughness [107, 108].

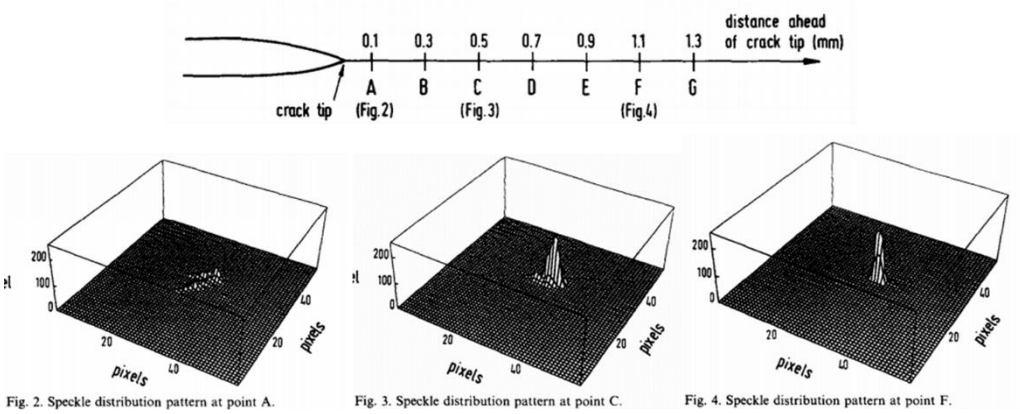

Fig. 2.12: Locations of various points where speckle patterns were recorded ahead of the crack tip (top). Corresponding speckle distribution pattern (bottom)

Tay et al. obtained a speckle patterns around crack tip as shown in Fig 2.12. They observed a low central peak intensity and a wide spectrum just ahead of the crack tip (Fig 2.12 location A), a wide spread of the spectrum with a sharp central peak intensity and low central peak intensity along with a narrow spread of spectrum away from the crack tip (Fig 2.12 location B and C). By employing the phenomena of "change in the intensity distribution of the speckle pattern as the level of strain decreases'', they calculated the measured plastic zone [107].

Steuwer et al. analysed the fatigue cracks using synchrotron X-ray tomography and diffraction technique [109]. Fig 2.13 shows the result of synchrotron X-ray tomography. Fig 2.14 represents the synchrotron X-ray diffraction images of residual strain in longitudinal and

transverse direction. They concluded that direct measurement of the residual strains accompanying a fatigue crack is possible using the Synchrotron facility.

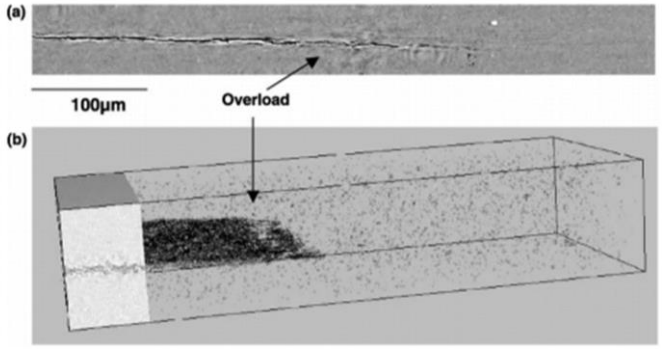

Fig 2.13 (a) A tomographic rendering of the crack tip, where only base material has been rendered transparent revealing the crack tip as well as other dispersions or inclusions. (b) The volume rendering indicates a region where the crack surface has closed.

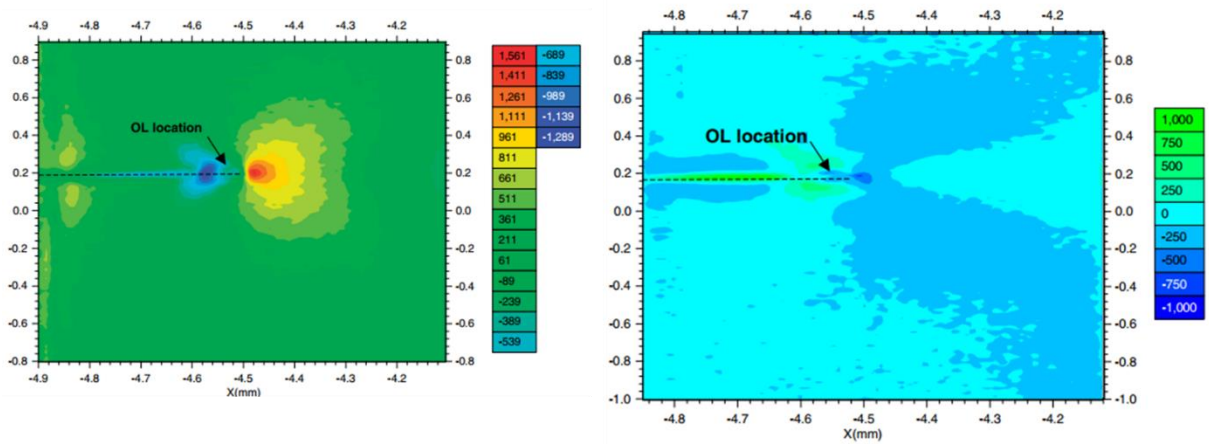

Fig 2.14: The residual strain in the longitudinal direction (left), the residual strain in the transverse direction (right) in units of micro-strain (10^{-6})

Patterson and Olden reviewed a range of non-contact optical techniques to investigate the displacement field around a propagating crack and the corresponding strain fields through the elastic component such as photoelastic stress analysis, thermoelasticity and caustics. In photoelastic stress analysis, fringes are observed in a stressed transparent body and viewed using polarized light [110]. Caustics usually use a laser but it is not adopted widely due to its complexity [111]. Thermoelasticity is the change in the size and shape of a solid object as the temperature of that object fluctuates. These temperature changes can be measured with a sensitive infrared detector and the signal from the detector is proportional to the sum of the principal stresses [112]. Thermoelastic Stress Analysis (TSA) is based on the principle of

thermoelasticity and has been used for studying fatigue cracks over the last four decades [113-119]. Patki and Patterson employed thermoelasticity to study the extent of the crack tip plastic zone based on the phase difference between the TSA and forcing signals [113]. Another widely used full-field measurement technique is Digital Image Correlation (DIC) which works by comparing the digital photographs of a component at different stages of deformation. Rossi et al. measured the strain field around the crack tip using stereo DIC to identify out-of-plane movements. Then, the Virtual Fields Method was used to identify the plastic zone, by identifying the parts of the specimen which deviates from the linear elastic behaviour [120].

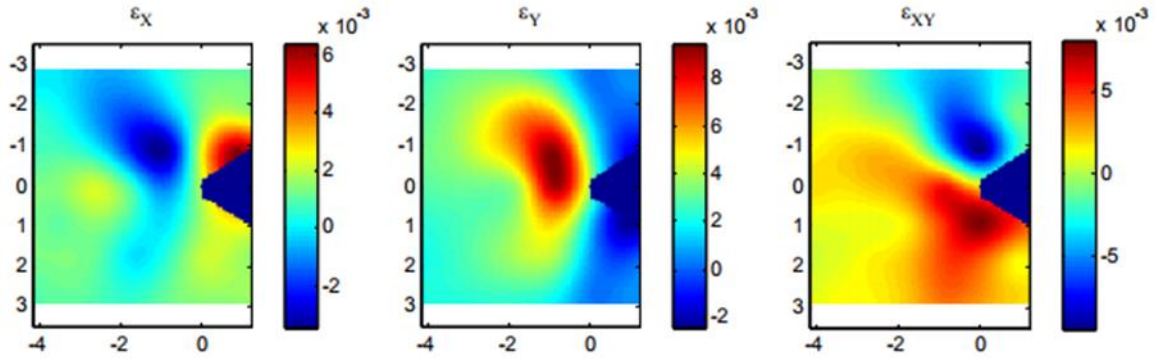

Fig 2.15: strain field measurement obtained by using stereo DIC

They introduced an error function that identifies the discrepancy between the elastic and plastic region. The error function obtained is plotted for different values of the tensile force as shown in Fig 2.16 (top image). Fig 2.16, bottom image represents the plastic zone obtained from FEM [120]. They claimed that qualitatively, a good match is found between the error maps and the plastic zone evaluated by FEM.

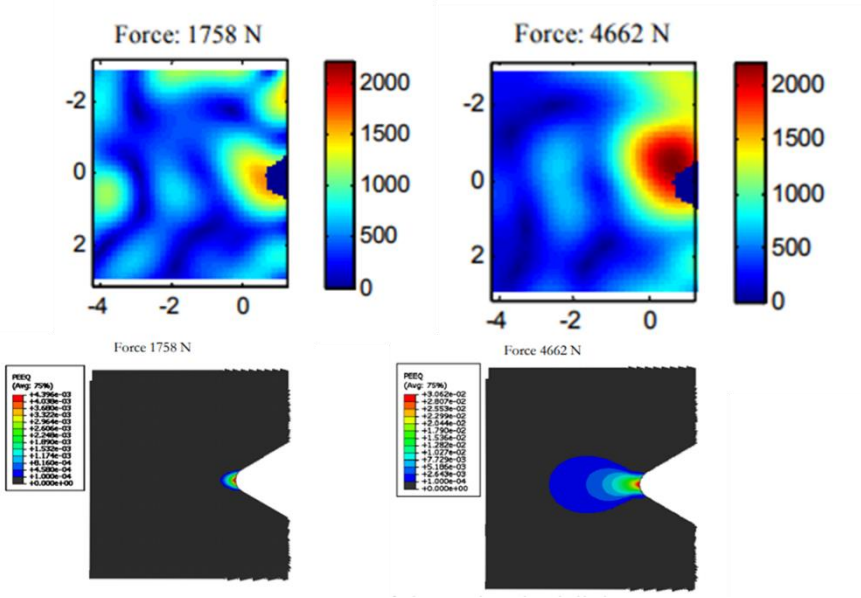

Fig 2.16: Top image represents identification of the plastic radius obtained from error function. The unit of this error is a specific energy. The Bottom image represents the plastic zone achieved from FEM [120]

The DIC method is robust and accurate to measure the strain and displacement fields in a variety of applications however it gives large errors and poor quality near displacement discontinuities such as cracks and shear bands as the subsets used for correlation requires spatial continuity [121]. To overcome this, the regions around the discontinuities are removed from the area of interest before analysis. For example, in Fig 2.15 and 2.16 (top image), the crack and the crack wake have been masked. This produces less than ideal results as it depends on how much area has been removed [122]. Moreover, it is not straightforward to identify the plastic zone from the DIC images. As to find a plastic zone, prior material knowledge is required and an assumption has to be made about the value and component of strain at which plasticity begins to occur. This may introduce significant uncertainty [123].

The rapid development of both the Transmission Electron Microscope (TEM) and the Scanning Electron Microscope (SEM) during mid-19th century provided new powerful tools to examine fracture surfaces with significantly improved resolution and depth of field [124]. In some ways, the ready availability of the SEM has limited detailed examination by TEM because of the ability to place large sections in the microscope for examination in conjunction

with reasonably high resolution and without the difficulties in specimen preparation such as cut into thin slices with thickness of the order of 250 μm, punch the specimen to maximum of 3 mm diameter discs [125]. Nowadays, SEM has become the most common instrument of use for high-magnification examination of fracture surfaces because of higher magnification. More recently, additional tools and techniques also have become available including Energy Dispersive x-ray Spectroscopy (EDS), the Auger microscope, the variable-pressure SEM, and the atomic-force microscope. Scanning electron microscopy has been employed for numerous studies to assess dislocations density at a micro scale [126-129]. A number of scanning electron microscopy approaches have examined how the local changes in lattice curvature and dilation associated with dislocations affect the lattice interaction with incident electron beams. The Selected Area Channel Pattern (SACP) method in scanning electron microscopy is a technique to characterize grain boundaries of polycrystalline materials and to detect plastic strain accompanying inter-granular fracture. Selected area channel pattern (SACP) generates a variation in intensity of backscattered electrons which deteriorates with increasing plastic strain [130-133]. Davidson and Lankford, who used SACP to measure the plastic zone size and strain distribution, concluded that plastic zone size is not proportional to the yield stress for fatigue cracks and that the stress intensity factor is correlated with work done in creating new crack surfaces. [134]

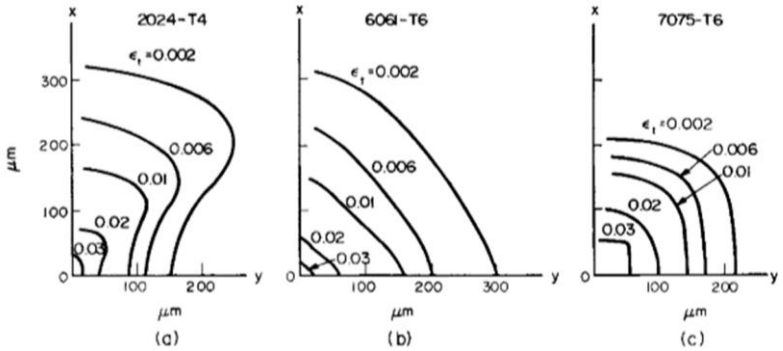

Fig 2.17: Plastic zone size obtained from Selected Area Channelling Pattern (SACP): (a) 2024-T4, (b) 6061-T6, (c) 7075-T6 [134]

The technique is limited to the study of grain sizes smaller than the selected area size and the fact that not all SEMs are capable of forming SACP. Moreover, most SEMs with SACP capacity can move the beam only about an area of a few millimetres in diameter due to spherical aberrations and focusing errors [135]. Wilkinson et al. successfully applied the Electron Channelling Contrast Imaging (ECCI) method by using a commercially available SEM fitted with field emission gun to reveal the formation of sub-grains due to deformation adjacent to the crack [136]. ECCI can reveal the distribution of dislocations and plastic strain around a fatigue crack but it requires Electron Back-Scattered Diffraction (EBSD) to measure the strains within the plastic zone. An EBSD pattern is a form of Kikuchi pattern which is seen in the angular distribution of backscattered electrons emitted from a crystal on which an incident electron beam is focused [137]. Quested et al. were the first to use EBSD for plastic strain measurement [138]. Jia et al. quantitatively elucidated the change in grain orientation dependent plastic behaviour in austenitic and ferrite steels during in-situ tensile tests and concluded that the plastic deformation of ferrite grains is triggered by dislocation accumulations in the neighbouring austenitic grains [139]. Even though EBSD is able to collect information from small areas of hundreds of nanometres in diameter under the electron beam, quantification becomes difficult at large strain levels.

Liu et al. developed a three-Dimensional X-Ray Diffraction (3D-XRD) technique in 2004 to characterize local orientations, stress states and grain boundary with micron scale resolution. They used the Laue diffraction method instead of the latest monochromatic diffraction to avoid the complications of sample rotation [140]. With the development of 3-D x-ray micro diffraction using polychromatic and monochromatic synchrotron radiation, Barabash et al. studied local 3-D lattice rotations and residual elastic strain simultaneously by characterizing the dislocation configuration in a nickel-based super alloy [141]. However, this technique is at a preliminary development stage and suffers from drawbacks of weak detectors, large X-ray

beam size, long data collection times and low spatial resolution. In 2014, Hruby et al. used X-ray synchrotron Laue microdiffraction and microtomography to examine the plasticity surrounding a fatigue crack in Al 7075-T651 alloy [142].

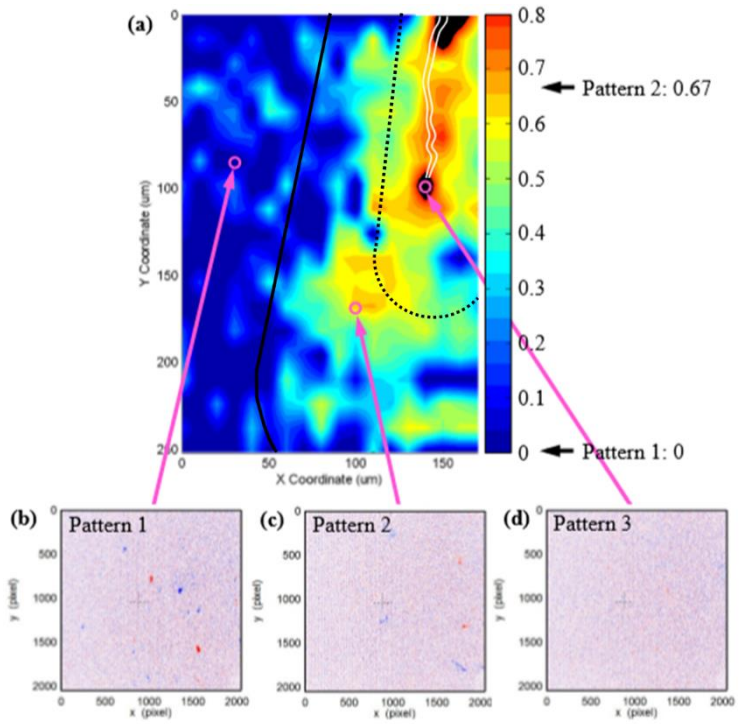

Figure 2.18. (a) Plot of the relative degree of peak broadening in a plane parallel to the specimen surface at a depth of 35 µm. Magenta circles indicate the locations of sample volumes from which Laue patterns were recorded. Relative FWHM values for the shown Laue patterns are indicated on the colour bar. Comparison of plastic zone size predicted by Irwin model to relative degree of peak broadening at depth of 35 µm predicted plastic zone for plane stress (solid) and plane strain (dashed). The crack location is outlined in white. Example Laue patterns exhibit (b) sharp, bright peaks, (c) broader peaks, and (d) absence of peaks [142].

Hruby et al. noted that numerous trial runs with varying box size selections were performed on patterns until an appropriate box size was chosen as the performance of the peak search routines was found to be largely impacted by the chosen box size. If the box size was too small, broad peaks may not be fitted and peaks may be fitted to noise, while if the box size was too large, sharp peaks may be excluded and computing time was greatly increased [142].

In 2015, Withers employed synchrotron X-ray diffraction and tomographic imaging to identify the elastic strain field by using the depths of the diffraction peak broadened region [143]. It is possible to apply the same technique using synchrotron X-rays, but the increased penetration of rays into the surface can complicate the depth analysis [143]. Nevertheless, there

are only few synchrotron radiation facilities available in the world for scientific research so it is out of the reach of a wide range of researchers.

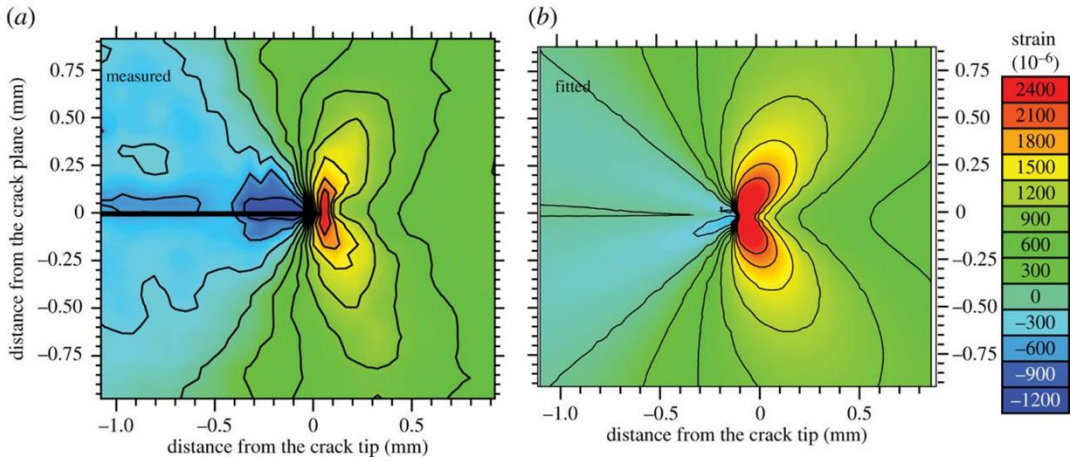

Fig 2.19: Elastic strain fields (10^{-6}) for the crack-opening (ε_{yy}) direction (a) The measured and (b) best-fit. The best-fit crack-tip strains correspond to a crack-tip effective stress intensity of K_{Imax}^{eff}=6.11 MPa√m and K_{IImax}^{eff}=0.33MPa√m [143]

Yang et al. used an electron backscattered diffraction technique to measure the residual strain distribution and plastic zone size around a fatigue crack tip and showed good agreement with the plastic zone size measured using Dugdale's theory. They also compared their results with another well-established TSA technique showing substantial agreement with TSA plastic zone demonstrating the great potential in identifying the role of the crack tip plastic zone in crack closure [144].

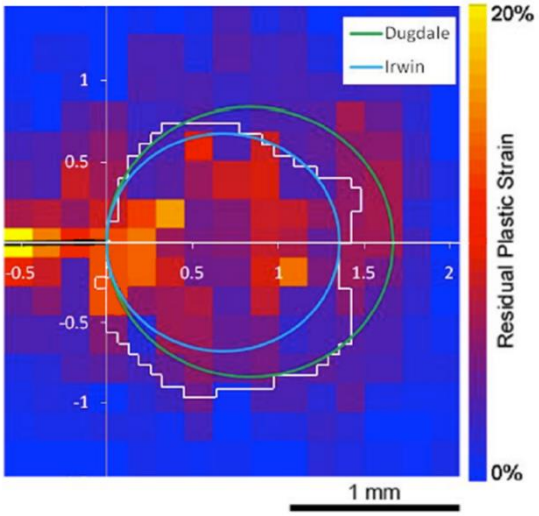

Fig 2.20: Map of plastic strain around the crack tip based on the FWHM of the DFTs of images from the region shown in Figure 5.1. The white line shows the measurement of plastic zone using TSA data. The green and blue solid lines indicate the theoretical estimations of the plastic zone size based on Dugdale's and Irwin's approaches, respectively [144]

Each technique discussed above has been able to perform measurements for the specific conditions, no single method can be recommended as being superior to all others for all materials and conditions. Thus, some of the techniques are applicable to materials of certain properties. For example, photoelasticity requires sensitive coatings on opaque materials, DIC requires discontinuity free area, interferometry methods have stringent stability requirements and synchrotron studies are less accessible. In the past, researchers have successfully employed the TSA technique to identify plastic zones. This technique does not require specific specimen preparation except easily available black paint. It is non-contact and non-invasive technique which does not require priori knowledge of material. The TSA measurements are based on applied stress which is the main driver of the fatigue related degradation. So, in the current project, TSA technique has been selected to measure the fatigue crack tip plastic zone size and shape at the macro scale. At micro scale, the BSEIA technique has been used to identify the plastic zone as no single technique is able to quantify the plastic strain distribution with ease and the clarity of resulting plastic zone is inferior for those techniques than that resulting from BSE image evaluation technique.

There are various measurements and inspections techniques available to identify the crack growth, evaluate the stress intensity factor and characterize the plastic zone. Several widely used contact and non-contact methods are described in the literature review are summarised in below table. The aim was to review all the techniques in terms of their sensitivity and spatial resolution. However, most of the researchers have not mentioned this crucial data in the research papers. Few of them have mentioned about the sensitivity in terms of qualitative terms, stating good sensitivity, higher resolution and so on. After studying several books and research papers below table has been compiled detailing as much information as possible.

Table 1: Summary of several widely used contact and non-contact methods to identify crack and plastic zone as described in the literature review

No	Technique	To identify	Limitation	Sensitivity and spatial resolution	Ref
1	Acoustic emission	Fatigue crack initiation and propagation	Only qualitative estimates of damage. Limited ability of precise identification of defect type. Difficult to detect the initiation of micro-cracks	Different piezoelectric sensors have different sensitivity depending on the type of material, frequency, length of cable	96
2	Eddy current method	Surface crack length and depth	Can't monitor deeper cracks at low frequencies. At high frequencies sensitivity is compromised	The eddy current sensors are sensitive to frequency and electrical conductivity of the material	97
3	Micro hardness	Hardness indentations around crack tip to determine elastic-plastic boundary	Improper specimen preparation, misaligned indenter and test piece could give erroneous result	The microhardness test is sensitive to number of variables such as indentation spacing, material segregation, inclusions, edge effects and cold working	98, 99, 100
4	Etching	Dark and light etched region in deformed & un-deformed region	Time consuming, different etching conditions for each material	The results of etching are sensitive to time for how long it has been etched and which etchant used.	98
5	Recrystalliza-tion	Deformed grains are observed under optical microscope to calculate the strain and the plastic zone boundary	Does not measure less than 2% deformation. It represents the maximum amount of plastic deformation and not the average deformation	Recrystallization technique is sensitive to the temperature and time to recrystalize. The very small plastic zone around the fatigue crack will not cause recrystallization so the technique is insensitive to strains around a small region of fatigue crack	98, 101, 102

6	Strain gauge	To measure strain field around the crack tip	Represents the average strain over the area and not at the specific point. Complicated interpretation	Strain gauges can measure the local strain precisely however the results are dependent on the placement of strain gauge which could not be placed exactly ahead of the crack otherwise crack will enter the gage and broke it. The gauges placed far from the crack does not reveal the accurate strain.	103
7	Optical microscopy	Crack growth is detected by travelling microscope	Time consuming and expensive automation. Needs accessible and corrosion free surface	Cannot detect very small crack or crack initiation. Requires calibration. Difficult to reach critical areas such as corners, bend	104
8	Optical interference microscopy	Measure of plastic zone based on out-of-plane deformations by using a laser beam	Requires perfectly polished specimen with 95% reflectivity. Requires stringent stability of the experimental set-up.	Measurements are not precise at slope changes of steeper flanks. So, the maximum tolerable surface slope should not be higher than the angle defining the numerical aperture of microscope objective.	105
9	Geometric Moir	Light interference to create contour maps of displacements fields	Insensitive to out of plane deformation including rotations. Challenging to use on composite material. Scratches or imperfections of the specimen considered as strain may lead to erroneous result.	The technique has 97.6% of the theoretical limit of sensitivity. 0.417μm per fringe order of sensitivity to in-plane displacements U and V. High magnifications and high spatial resolution is possible by placing camera lens very close to the replica	106,
10	Laser speckle	To observe the plastic zone by observing the	Speckle pattern intensity distribution varies as per the strain level. It	The threshold value of correlation parameter at which the plastic zone boundary is to be determined is chosen for each	107, 108

		surface roughness	depends on which correlation parameter threshold value has been chosen to determine the plastic zone	specific problem. Ref 107 chose plastic boundary corresponding to an effective residual strain of 0.2% while ref 108 determined plastic zone from the values above correlation parameter of 1.0% of effective strain	
11	Photo elastic stress analysis	To determine stress intensity factors. Plasticity could be identified from photoplastic stress analyses	The stress fringe values of model materials vary with time and from batch to batch. Hence, it is necessary to calibrate each sheet or casting at the time of the test to an accuracy of at least two or three decimal places, as it is the only parameter that links the optical information to the stresses	The sensitivity of the technique depends on the sensitive coatings on opaque material. To obtain strain information in photoplasticity the prototype and model materials must have the similar yield behaviour and the flow rules which is difficult. There are substantial number of methods available due to difference in the mechanical and optical behaviour of various models. The difference of analytical and experimental result was 5%	110, 215
12	caustics	To determine stress intensity factor	To analyse caustic data, the state of stress, plane stress, plane strain or three-dimensional, along the initial curve should be known beforehand. To estimate K_I by caustics, large loads should be applied to the specimen, creating values of KI close to the critical value K_{IC}	The caustic equations are the same for plane stress and plane strain. The values of the optical constants for the evaluation equation of caustics are quite different. Thus, substantial errors can be introduced when the proper values of the optical constants are not used. If ratios of radius of initial curve to plastic zone is smaller than 1.5, caustic method is insensitive.	111

13	Digital Image Correlation (DIC)	To evaluate stress intensity factor. Qualitative evaluation of plastic zone.	DIC method assumes that there is a direct correspondence between the motions of points in the image and on then object. This assumption is not true for discontinuity such as crack and hole. Second assumption is that each subset has adequate contrast which is not true during debonding/delamination of applied pattern	The plastic zone was qualitatively evaluated and not quantitatively. Ref 120 and 123 mentioned good agreement in experimental plastic zone with mathematical plastic zone until large scale plasticity occurred in later stage. Distortion, time variability, scan nonlinearities are the key factors affecting the accuracy of the DIC measurements.	120, 121,122, 123
14	Scanning Electron Microscope (SEM) Transmission Electron Microscope (TEM)	Dislocation density	SEM provides in-plane dimensional measurements which demands the precise knowledge of the sample viewing angle. Furthermore, high resolution SEM requires conducting surfaces. TEM operate at very high voltages	TEM study requires samples 0.1 nm or thinner AND could not find dislocation densities of greater than 10^{-15} m^{-2}. It could not find dislocations in samples with grain size lower than 100nm. SEM is used as an instrument for other technique such as ECCI, SACP, EBSD	126-129
15	Selected Area Channel Pattern (SACP)	Detect plastic strain accompanying inter-granular fracture	Limited to the study of grain size smaller than the area of observation. This method will not be applicable to the	The size of such a zone measured by the SACP method would be smaller than the total plastic zone size (where the position of the elastic-plastic	130-135

			study of polycrystalline specimens. The method can be applied to single crystals, or to coarsely multi-crystalline specimens with a known orientation	interface corresponds to strains of 0.1%).	
16	Electron Channelling Contrast Imaging (ECCI)	To reveal distribution of dislocations and plastic strain	Needs field emission gun and ECCI available to limited facilities. Quantification is difficult at large strain levels	ECCI technique allows the imaging of local changes in orientation only qualitatively, but with a high lateral resolution of up to 1 μm	136-139
17	3D XRD	Identify residual elastic strain by characterizing dislocation configuration	Preliminary stage of research, long data collection time, low spatial resolution, weak detectors.	XRD analysis of defect structures requires the use of a well-justified underlying model that connects a certain dislocation density and distribution with a total displacement gradient field	140, 141, 142
18	SXRD	To examine the plasticity	Box size selection is critical. only few facilities available around the world	Middle energy synchrotron X-ray radiation in reflection mode can measure surface stresses to a depth of ~200 μm while High-energy synchrotron radiation in transmission mode can penetrate up to 15 mm. Ref 216 indicated the instrumental resolution of $6.9x10^{-4}$ micro strain.	109, 143, 216

2.6 Crack closure

The phenomenon of crack closure was first studied and documented by Elber [32] in the 1970s. Since then various methods including direct observation, measurement of compliance, and indirect (non-compliance) thickness averaging techniques have been developed to study the phenomenon of crack closure [145,146]. Crack closure is a phenomenon in fatigue loading, during which the crack remains in a closed position even though some external load is acting on the material and crack faces contact prematurely during cyclic loading. Crack closure provides a longer life for fatigued material than expected, by slowing the crack growth rate. Elber suggested that crack closure decreased the fatigue crack growth rate by reducing the stress intensity range.

The possible driving mechanisms of crack closure are plasticity, flank roughness, oxides, viscous fluid and phase-transformation [35]. Roughness induced crack closure is influenced by micro-structure. Crack deflections due to microstructure heterogeneity leads to mixed mode loading conditions on the microscopic level causing a mismatch between the upper and lower crack faces resulting in crack closure [147]. Oxide induced crack closure is associated with corrosion products that become wedged between crack faces [35]. A stress-induced martensitic phase transformation at the crack tip results in process zone wake. Residual stresses in the transform zone can lead to crack closure [148]. Plasticity-induced closure results from compressible residual stresses developing in the plastic wake. During loading, a plastically transformed area is formed at the crack tip which leaves a wake of plastically deformed zone along the crack length. This zone has residual compressive stresses induced by the elastic and plastic deformation of the material during unloading. During the next cycle, while loading, the crack tip does not open unless the applied load is enough to overcome the compression of the flanks resulting in lowered effective stress at the crack tip [69].

2.6.1 Plasticity induced crack closure

In 1970, Elber reported that a fatigue crack in a centre-cracked-tension (CCT) panel of Al 2024-T3 subjected to zero-tension loading was fully open for only a part of the loading cycle. Elber ascribed this to contact of residual plastic deformation in the wake of the crack tip and realised that these faces would be subjected to considerable compressive stresses. He noted that at the tip of the growing fatigue crack generates a monotonic plastic zone during each loading cycle and much smaller reversed plastic zone during unloading. As the crack grows, the residual plastic deformation left in the a wake of crack extension causes the crack closure during unloading by reducing the crack opening as shown schematically in Fig 2.21 [19].

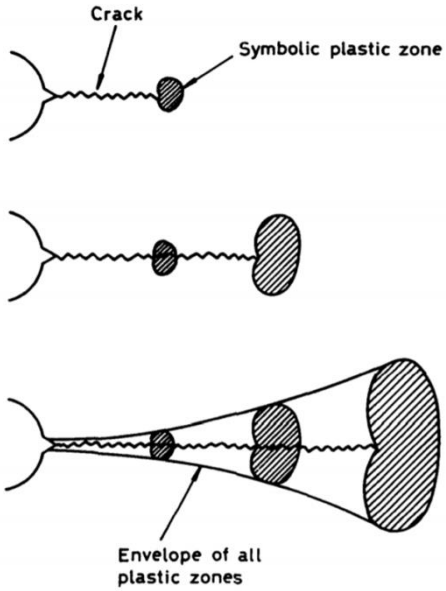

Fig 2.21: Development of a plastic zone envelope around a fatigue crack, after Elber [19]

The principle of crack closure can be explained with the help of Fig 2.22. Fig 2.22(a) shows the variation in the nominal stress intensity factor, $\boldsymbol{K}$ with applied stress $\boldsymbol{\sigma}$. Fig 2.22(b) shows that during unloading part of the fatigue cycle, as the applied stress decreases from $\boldsymbol{\sigma_{max}}$ the crack tip opening angle decreases due to elastic relaxation of the cracked body. However, the crack surfaces are prevented from becoming parallel because the stretched material along

the flanks causes closure before zero load is reached. This closure results in increased mode I stress intensity as the applied stress decreases.

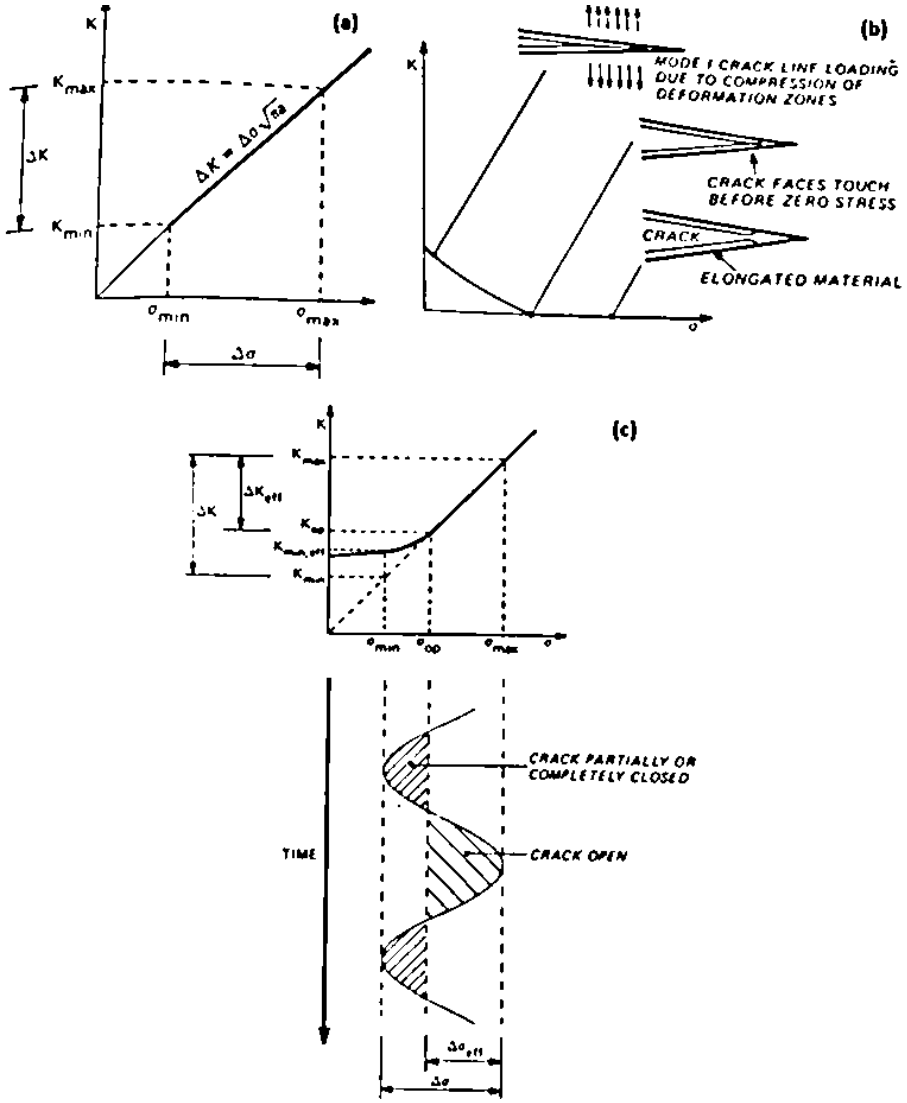

Fig 2.22: Principle of crack closure: (a) nominal stress intensity factor, K-σ plot, (b) residual deformation due to crack tip plasticity results in increased mode I stress intensity as the applied stress decreases (c) superposition of K values at various stress at a fatigue loading-unloading cycle showing the effect of crack closure [19].

Fig 2.22(c) shows the concept of crack opening stress, $\boldsymbol{\sigma_{op}}$, defined as the value of applied stress for which the crack is just fully open. It can be determined experimentally from the change in compliance: crack closure results in an increase of stiffness and decrease in compliance. Elber suggested that, for the fatigue crack growth to occur the crack must be fully open. Thus an effective stress intensity factor range, $\boldsymbol{\Delta K_{eff}}$ is smaller than nominal $\boldsymbol{\Delta K}$ and can be defined as,

$$\Delta \boldsymbol{K_{eff}} = \boldsymbol{K_{max}} - \boldsymbol{K_{op}} \qquad \textbf{[2.30]}$$

In short, crack closure implies that the crack tip is shielded from the complete loading cycle, leads to reduced stress intensity values and hence improved fatigue life by causing the retardation of crack growth.

2.6.2 Literature review on crack closure

Many attempts have been made to model crack closure usually by greatly simplifying the analysis to that of a plane stress or plane strain problem. One of the first and most well-known is the Budiansky and Hutchinson analytical model for plasticity-induced closure in fatigue cracks. Based on the Dugdale hypothesis and the theory of complex potentials, they demonstrated the concept of plasticity-induced crack closure under small-scale yielding conditions for plane stress. Budiansky and Hutchinson presented a complex function-analytical solution to determine the residual stress and the crack opening and closure loads for R≥0 loading. Fig 2.23 represents the opening and contact load ratios with respect to R. Their analytical solution can predict the influence of stress ratio on fatigue crack closure.

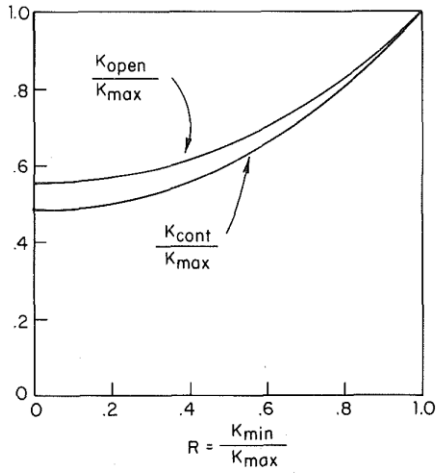

Fig 2.23: Opening and contact load ratios versus R

Budiansky and Hutchinson proposed analytical solution of crack closure but they do not include the interaction of a plastic zone with the surrounding elastic field and in particular any compatibility-induced stresses at the elastic–plastic boundary [149].

Various experimental techniques that were described in the previous section to measure the plastic zone can also be used to measure the crack closure effect. However, most of them have specific limitations in practical engineering applications as discussed earlier. Two non-contacting techniques named TSA and DIC have been increasing in popularity in experimental mechanics, especially for stress and strain analysis, due to their capability for full-field, non-contact measurement, and relative ease of implementation. In this section these two techniques have been compared to select the most suitable technique for the experimental research.

A number of investigators have studied plasticity-induced closure with finite element analysis [145-150] in 20th century. Most of the numerical studies from the 21st century focused on the optimization of the large number of numerical parameters and on the influence of physical parameters such as crack shape, stress state, or variable amplitude loading [151-157]. Zapatero et al. developed 2D plane stress and plane strain numerical model to check the effect of the maximum load, the crack length and the stress ratio on crack closure. They found that the results are independent of maximum load and the crack length, and there was a direct influence of the stress ratio [158]. Lopez-Crespo et al. combined experimental data measured by digital image correlation with an analytical model based on Muskhelishvili's formulation for the evaluation of crack closure [159]. They used aluminium alloy 7071 centre-cracked plate (CCP) specimens to identify the crack closure. It can be seen in Fig that the slope of the experimental curve is smaller than the nominal one suggesting a closure.

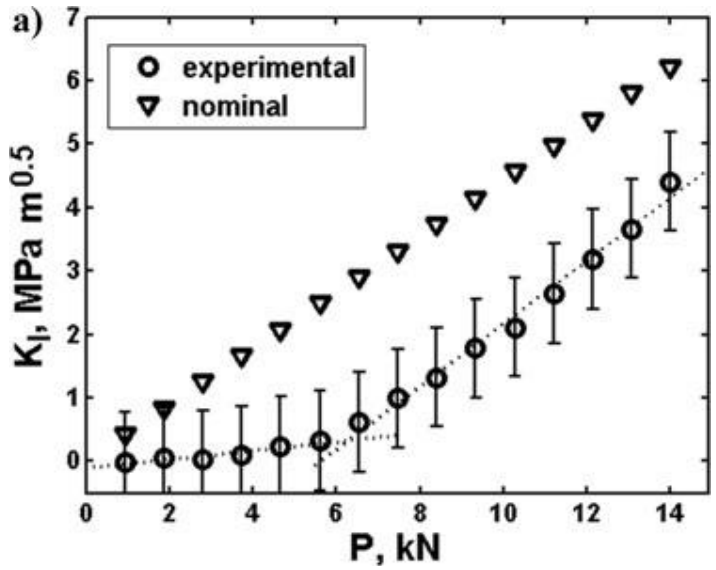

Fig 2.24: Opening (*K*I) mode stress intensity factors measured during the loading portion of a fatigue cycle ($R = 0$) with $\theta = 30^\circ$ on a 7010 aluminium alloy centre-cracked plate [159].

Christopher, James, and Patterson developed a new mathematical model (CJP model) of stresses around the crack tip by considering the effect of plasticity and its effect on crack tip shielding using the complex potentials of the Muskhelishvili approach. They noted that crack tip shielding not only includes the plasticity induced crack closure effect but also compatibility effects at the elastic–plastic boundary [160]. The stresses included in the CJP model are represented in the free body diagram shown in Fig. 2.25.

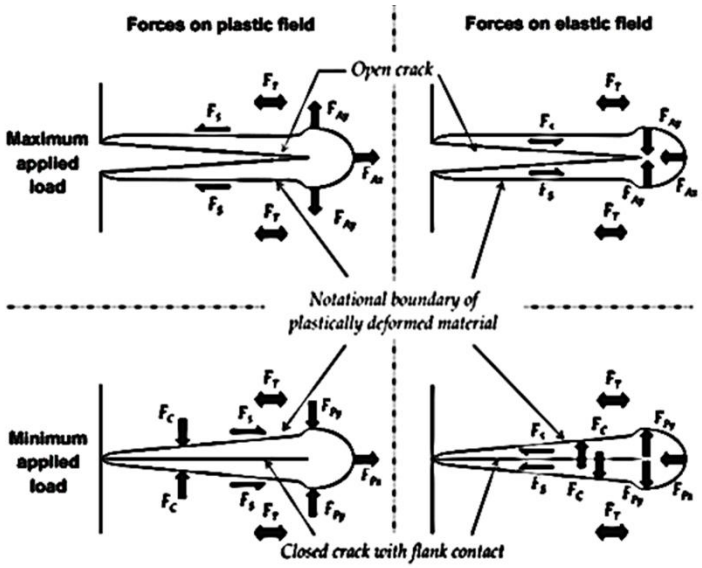

Fig 2.25: Schematic idealisations of forces acting at the interface of the plastic enclave and the surrounding elastic material, where F_A is the applied force generating the crack tip stress field characterised by K_I, F_T represents the force due to the T-stress shown in this example as positive, F_S is the interfacial shear force between the elastic and plastic zones, F_C and F_P together create the shielding effect. F_P is the force generated by the constraint of compatibility on the plastically deformed material and F_C is the contact force between the flanks of the crack generated by the interference of the plastic zones along the flanks [160]

Recently, Vasco-Olmo et al. employed four different mathematical models describing crack tip displacements field (Westergaard, Williams, Muskhelishvili equations and the CJP model) and compared them with experimental results obtained from digital image correlation and other compliance-based methods. They observed reverse plasticity influences plasticity-induced crack shielding in the case of the specimen tested at R = 0.1. They analysed the data from the CJP model for K_F (Free body diagram Fig 2.25) obtained from specimen CT1 (R = 0.6, a = 9.20 mm) and CT2 (R = 0.1, a =9.40 mm). As shown in Fig 2.26, the specimen tested at high R-ratio (0.6), the K_F values closely follow the trend in the nominal K_I values. In contrast, in the case of the specimen tested at low R-ratio (0.1), K_F deviates above the nominal K_I. This analysis of the trends in the stress intensity factor defined in the CJP model indicates that it is possible to identify the portion of the load cycle where there is a plasticity-induced shielding effect on the elastic crack tip field ahead of the crack tip hence CJP model is capable to evaluate the crack tip shielding during fatigue crack growth [161].

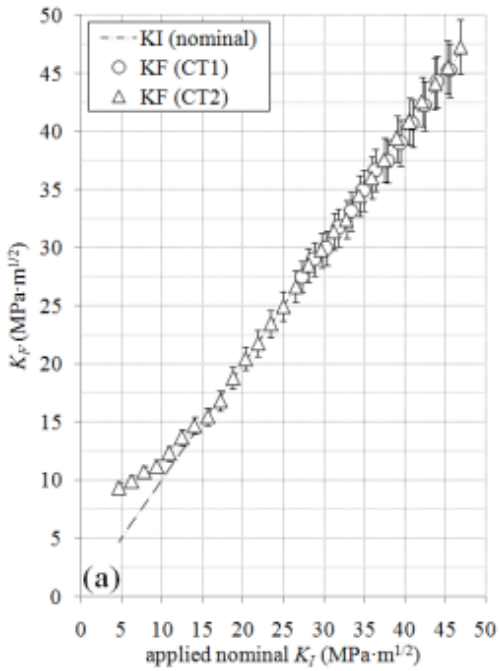

Fig 2.26: Values of K_F (a), K_R and K_S (b) obtained during a loading half-cycle as a function of the applied nominal K_I for the final crack length measured in each specimen, CT1 (R = 0.6, a = 9.20 mm) and CT2 (R = 0.1, a =9.40 mm)

Antunes at el. investigated crack closure numerically and experimentally. They employed middle-tension specimens of AA6016-T4 aluminium alloy and a pin micro-gauge to record the opening load and showed a good agreement between experimental and numerical results [162]. The use of Digital Image Correlation (DIC) has become very popular to study crack closure experimentally. Becker et al. presented a combined experimental–numerical technique for the calculation of the J-integral based on full-field displacements measurements using DIC [163]. They transformed the displacement vectors into FE domain through a MATLAB implemented routine (JMAN) to obtain the J-integral as an area integral and JMAN methodology was verified using an ABAQUS model and a weight function calculated SIFs [163]. Song et al. conducted a crack propagation analysis and a damage evaluation study in sandstone specimens using DIC [164]. By analysing the DIC images of horizontal displacement contours and equivalent strain field, they found that the damage spreads diffusely over the specimen at an early loading stage, and then, it concentrates in local region having significantly larger value than other region. With increment of stress, the concentration of the damage leads to the nucleation of a macro crack leading the crack propagation to the bottom of the specimen. Nowell et al. employed Moiré interferometry and DIC to measure in-plane displacements close to the crack tip to determine the presence of crack closure in propagating fatigue cracks [165]. They observed that even though the load varies sinusoidally, the relative displacement does not, it remains constant for some period of loading and they concluded that it is due to crack closure. They also studied the thickness effect in plasticity-induced fatigue crack closure using DIC and traditional compliance techniques [166]. They plotted the opening load as a function of crack length for three specimens of different thickness (3 mm, 10 mm and 25 mm thick) measured by compliance method and DIC. Their investigation showed that the opening load for compliance measurements is sensitive to thickness of specimen while DIC gives same opening load for all three specimens of different thickness. So, they summarised that for the

plane strain condition, the compliance method was more suitable than DIC to measure effective crack closure. In a displacement-based technique (i.e. DIC), any plastic deformation at the crack tip will affect the data over the whole field, since displacements in the plastic zone effectively generate a rigid body motion of the material at a distance from the crack tip so the area in the immediate vicinity of the crack needs to be excluded as the displacement field equations being employed are based on linear elastic fracture mechanics. However, TSA method does not suffer from this because it measures effects produced by strain which is a derivative of displacement, eliminates the rigid body motion so that the effect of plastic deformation are limited to plastic zone and does not affect the data collected from outside the plastic zone [167]. Using DIC technique, the plastic zone can be estimated from the strain values by assuming that strains greater than the material yield strain were plastic. This approach is potentially less reliable than the Thermoelastic Stress Analysis method because it is dependent on a reliable material data and high-resolution digital image correlation data [168]. Though it is possible to identify crack closure using DIC, straightforward evaluation of plastic zone is difficult and less reliable compared to the TSA technique. Considering all these aspects, the TSA technique has been employed for the current research.

2.7 Literature review on Thermoelastic stress analysis

In 1986, Stanley and Chan developed a method to characterize the stress field ahead of the crack tip by determining the stress intensity factors from the thermoelastic images under mode I and mode II loading using the first two terms of Westergaard equation [114]. In 1996, Lesniak et al. fitted Williams' stress field equations to thermoelastic data using a least squares optimization method [115] and they were the first to witness the crack closure effect using TSA followed by Leaity and subsequently by Fulton et al [169-170]. They found that the evaluated stress intensity factors were considerably lower than the values expected from theory. Nurse and Patterson fitted the Muskhelishvili-type stress descriptor using the multi-point over

deterministic method (MPODM) to develop photoelastic characterisation of fatigue crack [117]. Tomlinson et al. performed further experiments with a TSA system and detected lower values of ΔK_I when compared with those calculated using analytical methods and assumed that crack closure was responsible for the same [118]. Subsequently, Dulieu-Barton et al. improved their computational techniques for calculating stress intensity factors from contours of constant first stress invariant around the crack tip which was done manually in their earlier work [171]. These improvements gave better agreement between their experimental and theoretical values including mixed mode cracks. They were also able to detect the effects of closure with as much as a 12% reduction in the value of ΔK_I. Diaz et al. located the crack tip in recorded thermal images of the specimen and identified plasticity from the map of phase difference between the applied load and surface temperature obtained from TSA signals [172]. They demonstrated the sensitivity of TSA, showing a reduction in the difference between the experimental and theoretical stress intensity values with increased load ratios (R-ratio). This has been developed further by Patki and Patterson who studied the effect of overloads on stress intensity factors and plastic zone size for the first time. They developed a technique to measure the radius of the plastic zone directly from the phase information; and for constant amplitude loading; their results were consistent with estimates from theory. They concluded that immediately post-overload the plastic zone increased in size by up to 50% whereas the amplitude of the stress intensity factor and the crack growth rate decreased until the crack grew through the plastic region created by the overload when the pre-overload value of the crack growth was re-attained [113]. All these experiments suggest TSA is good choice to study fatigue cracks with crack closure.

It has been known for more than five decades that overload cycles of sufficient magnitude can result in retardation of fatigue crack growth [173]. It is also well-established that this retardation is closely related to the residual compressive stress field induced in the

vicinity of the crack tip [59]. Since the 1960s several models have been proposed to predict the crack growth associated with overloads and underload. The most common are Elber [154] and Wheeler [174] growth prediction models based on the Paris law [87]. Wheeler assumed that, following an overload, a retardation process occurs as the crack propagates through the plastic zone produced by the overload. In a similar manner to Elber, Lu et al. developed a model by modifying the range of mode I stress intensity factor, ΔK_I with an empirical constant which was based on the crack length and the size of the crack tip plastic zone so that the model has the potential to account for some of the effects on ΔKI of closure induced by plasticity [175]. Lopez et al. validated the Wheeler model for the prediction of fatigue crack growth retardation in welded steel joints and showed good agreement with the experimental observation [176]. Wheeler model requires an evaluation of the stress intensity factor and then derived from it, the radius of the crack tip plastic zone. As has been discussed earlier, using TSA the stress intensity factor can be evaluated directly and the radius of the plastic zone ahead of the crack tip can be measured directly with a high level of reliability so TSA was first choice to identify crack closure in the presence of overload.

2.8 Aims of the research

In this study fatigue cracks were propagated in pure Titanium, Al2024-T3 and Al6061-T6 Compact Tension (CT) specimens to study the effect of various values of strain hardening exponent on crack closure by determining the stress intensity factor range and crack growth rate by employing TSA technique. The crack tip plastic zone was characterised experimentally for all three materials having a range of strain hardening exponents to identify the effect of value of strain hardening exponent on plastic zone size and shape. Multiple cycles overloads with a range of magnitudes at various load ratios were applied to specimens at the same nominal crack length to study the effect of value of strain hardening exponent on crack growth after

application of overload by analysing the size of the crack tip plastic zone, the stress intensity factor and crack growth retardation. The methodology proposed by Yang et al. [151] to characterise plastic zone of a fatigue crack by evaluating backscattered electron images by applying Discrete Fourier Transform (DFT) has been carried forward to quantify the plastic zone of a fatigue crack subjected to overload. To validate the plastic zone predicted numerically by Hutchinson (1971) and Shih (1973), their proposed plastic zone contours were compared to the experimental plastic zone contours at various values of strain hardening exponent. Finally, a novel method to characterise the plastic zone size using a mathematical function has been developed.

Chapter 3

Experimental Procedure

3.1 Material selection

Titanium has high tensile strength to density ratio, high corrosion resistance, fatigue resistance and ability to withstand moderately high temperatures without creeping, so it is widely used in aircraft, armour plating, naval ships, spacecraft, and missiles [177]. Titanium is alloyed with aluminium, zirconium, nickel, vanadium, and other elements to manufacture a variety of components including rotors, compressor blades, critical structural parts, exhaust ducts (helicopters), propeller shafts, fire walls, landing gear, and hydraulic systems. About two thirds of all titanium metal produced is used in aircraft engines and frames. For example, estimated 59 metric tons (130,000 pounds) are used in the Boeing 777 and an Airbus A380 uses 77 metric tons [178]. Titanium containers have been studied for the long-term storage of nuclear waste, because of its excellent corrosion resistance [179]. Titanium products are widely used in aerospace, industrial, marine, medical and nuclear industry. In the current project, Titanium has been chosen as a material in which the plastic zone has been characterised, considering its applications as detailed above.

Aluminium plays a critical role in a number of different industries including aerospace, transportation, construction, medical devices, and general manufacturing. Aluminium alloys 2024-T3 and 6061-T6 possess high fracture toughness, high fatigue performance, high formability, and superplasticity to meet the needs for lower structural weight, higher damage tolerance, and higher durability [180]. Al 2024-T3 is alloyed with copper and heat-treated and cold-worked while Al 6061-T6 is alloyed with magnesium and silicon and heat-treated and

artificially aged. These Aluminium alloys also offer good electrical and thermal conductivity, as well as having the ability to be superconductors. Moreover, they have high strength and their ductility does not decrease significantly during strengthening heat treatments [181]. These unique properties made aluminium alloys suitable for lowering costs of aircraft manufacturing while upholding stringent specifications required in the industry. Previous literature suggests that Aluminium 2024-T3 and 6061-T6 have value of strain hardening exponent of 8 and 14 respectively [69]. Hence, the Aluminium alloys 2024-T3 and 6061-T6 have been selected to characterise plastic zone experimentally as they not only offer range of strain hardening exponents but also extensively used by aviation industry.

3.2 Calculation of Strain hardening exponent

Strain hardening also known as work hardening is the term used to describe the phenomenon that most metals become stronger when plastically deformed. This strengthening occurs because of dislocation movements and dislocation generation within the crystal structure of the material [182]. The strength, ductility, toughness, and deformability of materials are intimately related to their strain–hardening characteristics. The strain–hardening exponent (n) is important indicator of the strain–hardening properties of metallic materials [182]. It characterises the amount of uniform plastic strain the material can undergo during a tensile test before strain localization or necking leading to failure. The value of strain hardening exponent n has been determined from the tensile stress-stain data obtained in a uniaxial tension test by following the BS EN ISO 10275:2007 standard [183]. A standard test tensile test specimen of gauge length 50 mm and width 12.5 mm were prepared for the test (Fig 3.1).

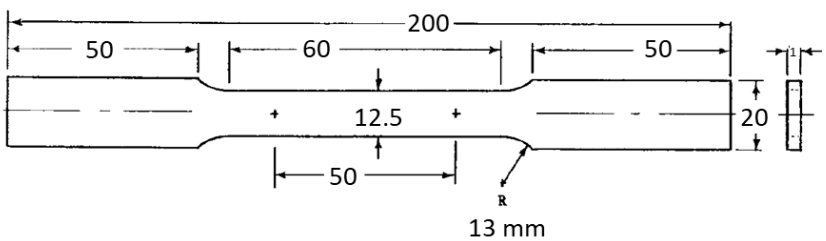

Fig 3.1: Standard tensile test specimen BS EN ISO 10275:2007 standard [183]

Tensile data were obtained in a continuous and rate-controlled manner via strain control. The strain-hardening exponents are determined from an empirical representation over the range of interest of the true-stress versus true-strain curve. The mathematical representation used in this method is,

$$\boldsymbol{\varepsilon = \frac{\sigma}{E} + K\left(\frac{\sigma}{E}\right)^{n}} \quad \textbf{[3.1]}$$

where, $\boldsymbol{\varepsilon}$ is the uniaxial strain, $\boldsymbol{\sigma}$ is uniaxial stress, $\boldsymbol{E}$ is Young's modulus, $\boldsymbol{K}$ is a constant and n is the value of strain hardening exponent. A minimum of four tensile tests were performed to determine n reliably (to ensure repeatability and consistency). The value of strain hardening exponent n from the four tensile tests for each material is listed in Table 2.

Table 2: The value of strain hardening exponent-n for 3 different materials calculated from 4 tensile tests

Material	n - Test 1	n- Test 2	n- Test 3	n - Test 4	Average(n)
Pure Ti	6.14	6.09	6.11	6.22	6.14
Al 2024-T3	8.27	8.41	8.19	8.13	8.25
Al 6061-T6	14.17	14.37	13.97	14.32	14.21

The three test materials - Titanium, Al 2024-T3 and Al 6061-T6 were found to possess the value of strain hardening exponent, n of 6, 8 and 14 respectively. Fig 3.2 shows the stress and strain curves for the three materials.

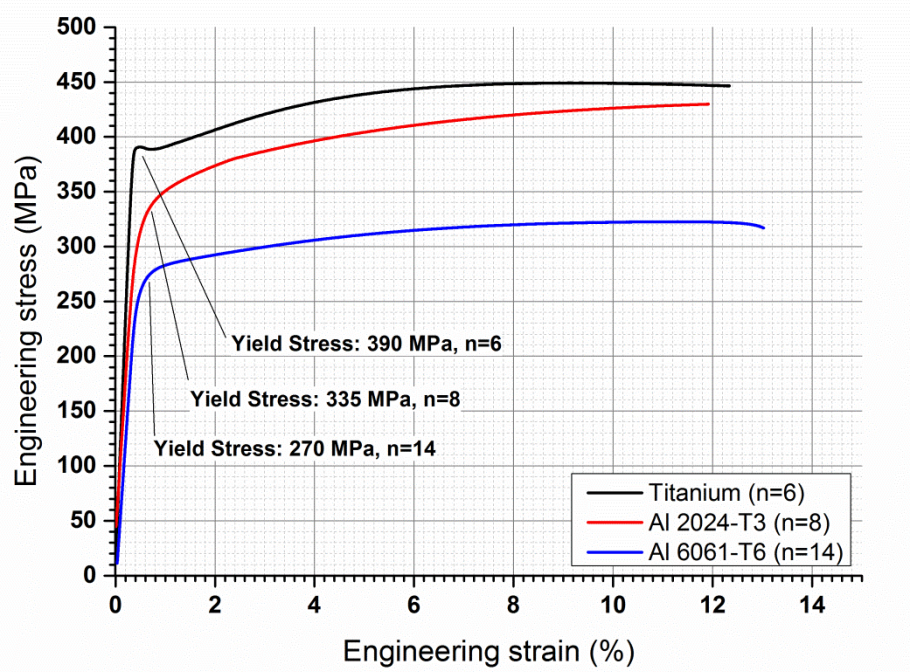

Fig 3.2: Engineering stress-strain curve obtained for pure Titanium, Al 2024-T3 and Al 6061-T6

3.3 Specimen preparation

There are several standard fatigue test specimens suggested by BS ISO 12108:2012 standard to analyse the fatigue crack growth rates, such as, the Middle Tension (MT), Compact Tension (CT), Double Cantilever Beam (DCB), and Single Edge Notched Bend Specimen (SENB). One of the widely used specimen is the Compact Tension (CT) specimen [91]. The benefits of using CT specimen are (a) they require less material due to its compact design and (b) can be prepared in smaller sizes so can be easily accommodated in the chamber of scanning electron microscope. For these reasons, a CT specimen has been selected as a test specimen for this research.

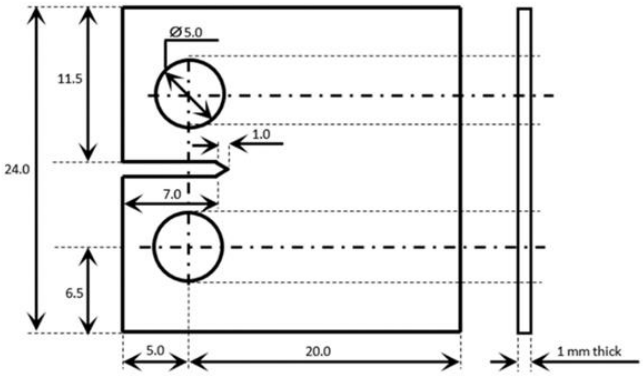

Fig 3.3: CT specimen geometry (all dimensions are in mm)

The CT specimens used in the research had a height of 24 mm, width from the loading holes of 20 mm and a notch which is at 3 mm distance from the loading holes as shown in Fig 3.3. All the specimens were nominally 1 mm thick. The fatigue cracks developed in the CT specimens were observed using a Thermoelastic Stress Analysis (TSA) system on one side during experiment and using a FE SEM (Field Emission Scanning Electron Microscope) on the other side after completion of each experiment. TSA requires little or no preparation on the specimen surface. A thin and uniform layer of matt black paint was sprayed on one side of each specimen in order to achieve a high and uniform emissivity and to reduce surface reflectivity to avoid unwanted reflections entering the infrared camera from the test specimen. The surface of the specimen for SEM observation should be without scratches, deformation and foreign particles. The surface of a specimen was prepared metallographically i.e. by grinding, polishing and electropolishing to achieve a plane and highly reflective specimen surface to observe under the SEM. The CT specimen was mounted on a brass bar using picien wax and polished using 800, 1200, 2500, 4000 grit SiC paper successively, followed by direct polishing with colloidal silica in order to achieve a 0.05 μm finish. The specimen was electropolished using Struers LectroPol-5 equipment and with A2 electrolyte (5-15% Butoxythanol, 65% ethyl alcohol, 60% perchloric acid and water). All the electropolished specimens were stored in airtight containers with silica gel desiccant bag inside to preserve them from contamination and corrosion.

3.4 Thermoelastic Stress Analysis (TSA)

Thermoelastic stress analysis (TSA) is a non-destructive and non-contact experimental technique that provides full-field stress maps on the surface of a mechanical component in real time based on the principle of the thermoelasticity.

3.4.1 Thermoelasticity

Any substance in nature becomes slightly cooler or warmer when its volume is changed by force; this is known as thermoelastic effect or thermoelasticity. It can be produced either by a compressive load which heats the substance or by a tensile load which cools the substance [184]. The thermoelastic effect was first recognised by Weber in the 18th century [185]. Lord Kelvin established the theoretical foundations of thermoelasticity in the 1850s [186] and it was confirmed experimentally in 1915 by Compton and Webster [187]. Lord Kelvin derived a linear relationship between the temperature change of a solid and the change in the sum of the principal stresses for isotropic materials based on the assumption of reversible and adiabatic conditions denoted by [186],

$$\Delta \boldsymbol{T} = -\frac{\boldsymbol{T}}{\boldsymbol{\rho C_p}} \sum \frac{\boldsymbol{\partial \sigma_{ij}}}{\boldsymbol{\partial T}} \boldsymbol{\varepsilon_{ij}} + \frac{\boldsymbol{Q}}{\boldsymbol{\rho C_\varepsilon}} \quad \textbf{[3.2]}$$

Where $\Delta \boldsymbol{T}$ is the temperature change, $\boldsymbol{T}$ is absolute temperature of the material, $\boldsymbol{\rho}$ is the density, $\boldsymbol{C_p}$ is the specific heat, $\boldsymbol{\sigma_{ij}}$ is the stress tensor, $\boldsymbol{\varepsilon_{ij}}$ is the strain tensor, $\boldsymbol{Q}$ is the heat input and $\boldsymbol{C_\varepsilon}$ is the specific heat at constant strain. When a material is subjected to a cyclic load, the strain produces a cyclic variation in temperature. To ensure that no heat conduction takes place within the object it is necessary to apply cyclic loads of suitable frequencies to maintain adiabatic conditions, in that case the second term on the right-hand side of expression [3.2] can be neglected and the equation can be rewritten as [19],

$$\Delta \boldsymbol{T} = -\frac{\boldsymbol{\alpha T}}{\boldsymbol{\rho C_p}} \boldsymbol{\Delta} (\boldsymbol{\sigma_x} + \boldsymbol{\sigma_y}) \quad \textbf{[3.3]}$$

By using a suitable infrared detector, it is possible to record a minute variation in temperature of the object surface in terms of a voltage output, $\boldsymbol{S}$. All objects emit spectral radiant photons based on their temperature and the amount of radiation emitted increases with temperature. This emittance depends on the object's surface emissivity $\boldsymbol{e}$ and the absolute temperature of the object $\boldsymbol{T}$. The emissivity of the surface can be maintained constant by applying a thin and

uniform coat of flat black paint that also reduces unwanted reflections into the infrared camera from the test specimen. Then under reversible (system will be returned to its original state if the stress is removed) and adiabatic (no heat is gained or lost by the system) conditions for isotropic material, equation [3.3] can be stated as thermoelastic expression,

$$\Delta(\boldsymbol{\sigma_x} + \boldsymbol{\sigma_y}) = \boldsymbol{AS} \quad \textbf{[3.4]}$$

where $\boldsymbol{S}$ is the signal recorded by the infrared detector and $\boldsymbol{A}$ is the thermoelastic constant which depends on the material properties of the object such as, the coefficient of thermal expansion, density, specific heat capacity under constant pressure and the surface temperature.

$$\boldsymbol{A} = \boldsymbol{f}(\boldsymbol{\alpha}, \boldsymbol{\delta}, \boldsymbol{C_p}, \boldsymbol{T}) \quad \textbf{[3.5]}$$

3.4.2 Equipment

The TSA system consists of two key parts: a camera unit (infrared photon detector) to capture data and DeltaVision software for data handling, viewing and processing the thermal images. The schematic is shown in Fig 3.4. Fig 3.5 shows an image of a specimen mounted on a loading rig and a photon detector (FLIR camera) fixed on a damped optical table. The FLIR SC7650 photon detector employed has an Indium Antimonide (InSb) detector. It is capable of capturing 400 frames per second for up 640 x 512 pixels array (or 320x256) for various frequencies (0.5Hz to 200 Hz). The system has a thermal sensitivity of 20 m°K and a spatial resolution of 60μm at its maximum optical magnification [188].

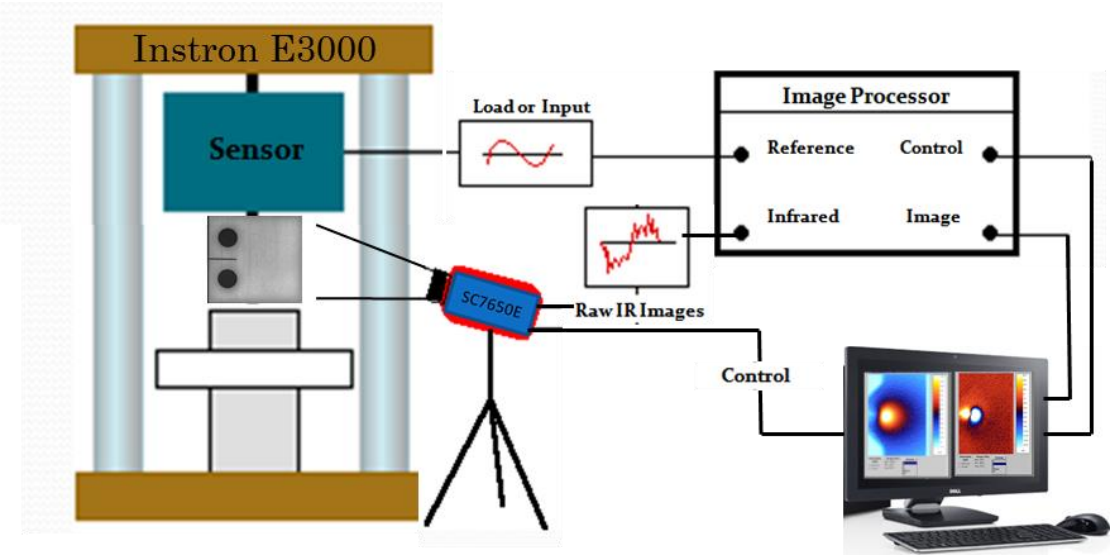

Fig 3.4: Schematic representation of TSA system and a loading rig

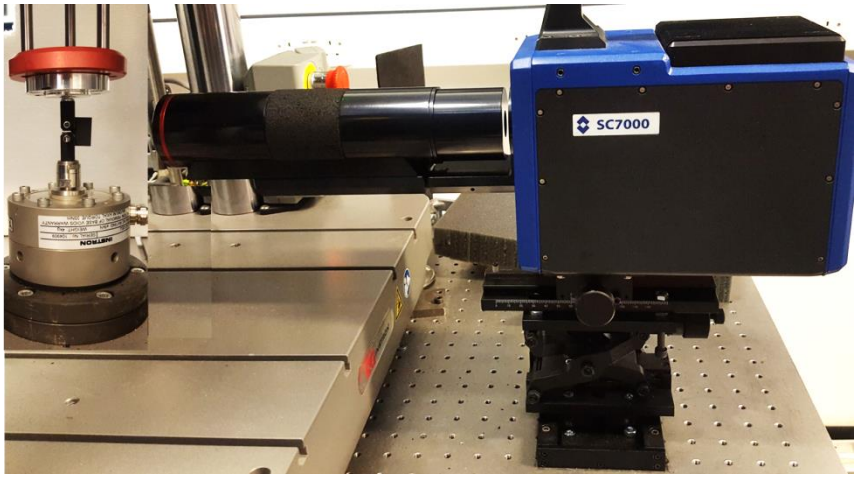

Fig 3.5: TSA FLIR camera and a CT specimen loaded on Instron Electropulse E3000 test machine

For current research, the zoom lens was used to detect the crack growth. The zoom lens operates at working distance of 5cm and has x5 magnification compared to normal lens. It has spatial resolution of 22 µm and thermal sensitivity of 1 mºK [188]. The array of detectors in the FLIR SC7650E is cooled by a closed cycle cooling system based on Stirling cycle [188]. To measure small temperature changes generated by the thermoelastic effect, a lock-in amplifier was fitted in the TSA system to filter out the signal noise. In the lock-in analyzer, a reference signal (often the load cell signal) is used to provide a band-pass filter. The infrared (IR) signal is then filtered, relying on the reference signal to extract only the temperature changes at the reference frequency (i.e. the loading frequency). Lock-in analyzers separate the detector output into two

components, (I) in-phase and (II) 90◦ out of phase with respect to the reference signal. The adiabatic structural response will be in-phase with the reference loading frequency but heat conduction in regions of high stress gradients or an insufficient loading frequency causes a phase shift from the reference frequency and will be evident as an out-of-phase detector signal.

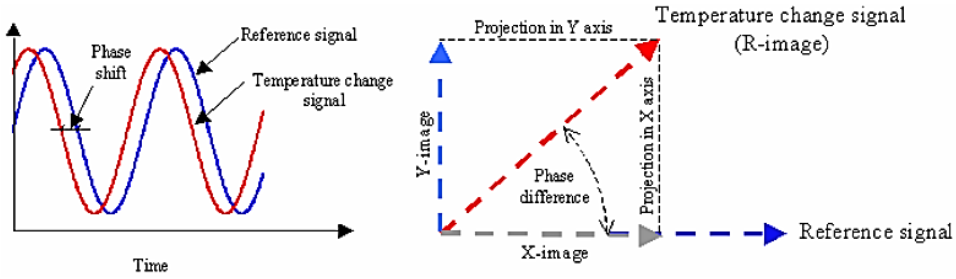

Fig 3.6: Schematic representation of thermoelastic information. Temporal variation of temperature change and reference signals (left). Vectorial representation of temperature change and reference signals (right) [172]

Fig 3.6 represents the TSA image as a temporal representation of temperature change and a reference signal along with the vector with magnitude (R-image) and phase. The phase denotes the angular shift between the thermoelastic and reference signals. The Cirrus software is used to set various camera configurations such as, non-uniformity correction, the frame rate and integration time (exposure time). DeltaVision software controls the FLIR camera and saves the thermal images and allows further processing of the images.

3.4.3 Calibration

For quantitative analysis, it is necessary to calibrate the thermoelastic signal ***S*** in terms of stress or strain. There are several different techniques listed in the literature to perform calibration but the most commonly used method is bonding a strain gauge rosette in a region of uniform stress at the back of a plane specimen where the corresponding thermoelastic signal from the front of the specimen can be obtained [189, 190]. According to equation [3.3], the sum of principal stresses is proportional to temperature change. According to Hooke's law the strain in a solid is proportional to applied stress within the elastic limit of that solid,

$$\frac{E}{(1-\nu)}\Delta(\varepsilon_x + \varepsilon_y) = \Delta(\sigma_x + \sigma_y) \quad \textbf{[3.6]}$$

Comparison of equation [3.4] and [3.6] gives,

$$AS = \frac{E}{(1-\nu)}\Delta(\varepsilon_x + \varepsilon_y) \quad \textbf{[3.7]}$$

where E is Young's modulus, ν is Poisson's ratio, ε_x and ε_y are the principal strains in two orthogonal directions. The calibration constant, A can be calculated by correlating the thermoelastic signal from the strain gauge location with the signal from the strain gauge rosette. In the current project, the TSA data were calibrated using an orthogonal strain gauge rosette (FCA-2-23 for Titanium and FCA-2-11 for Aluminium 2024-T3 and 6061-T6) bonded to the reverse of ta tensile specimen (gauge length 50 mm, width 12.5 mm, thickness 1 mm) in a region of uniform stress. The tensile specimen used for the calibration is shown in Fig 3.7.

Fig 3.7: Titanium tensile specimen showing the strain gauge rosette which was bonded on one side and black paint on the other side for TSA experiment

3.4.4 Thermoelastic data processing

The TSA image captured during a fatigue test was an AC image which is a differential thermal image that shows temperature variations over time. The information in AC images is presented as a vector through four different images. The R-image, which is the magnitude of IR signal and express the variation of temperature on the specimen. The Phase-image refers to the difference between the reference signal and the temperature variation on the specimen. The X-image (Fig 3.8 (a)), and Y -image (Fig 3.8 (b)) are the projections of R-image (Fig 3.8 (c))

on X and Y axes of a given coordinate system (Fig 3.6). The data from the TSA image is in the units of thermoelastic signal output which was converted to °C using a temperature calibration curve obtained using a black body at various temperatures.

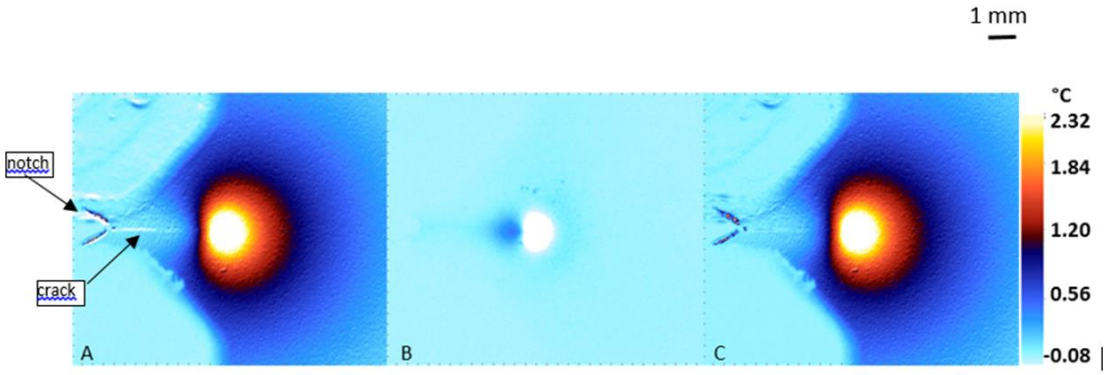

Fig 3.8: Thermoelastic response of a CT specimen (mounted between clevis grips) during a fatigue test showing a notch and a crack. (A)Thermoelastic X-image, showing a large positive response ahead of the crack (B) Thermoelastic Y-image, showing an approximately null field except ahead of the crack (C) Thermoelastic R-image, it is a sum of X-image and Y-image and Y-image is null so R-image is similar to X-image

3.4.5 Methodology for extracting SIF from TSA data

The full-field stress maps around the crack tip were processed using a freely available software package, FATCAT (www.experimentalstress.com) To evaluate the stress intensity factor, the Multi-Point Over Deterministic Method (MPODM) is used in the software to fit Muskhelishvili's complex stress descriptors to describe the crack tip stress field using the methodology of Diaz et al. which is based on the formulation developed by Tomlinson et al [118, 119].

3.4.5.1 Mathematical model

Westergaard equations are based on the assumption of a uniform passing stress field, i.e. in the absence of the crack the stress field is uniform, whereas the Muskhelishvili's approach removes this assumption which means it can be used for cracks in the presence of other stress raisers including those arising from geometry and loading.

Muskhelishvili's complex representation of the stresses

The one caveat to note is that Westergaard solution applies to an infinite plate in equal-biaxial, not uniaxial, tension. They are based on the assumption of a uniform passing stress field, i.e. in the absence of crack the stress field is uniform, whereas Muskhelishvili's approach removes this assumption which means it can be applied for the cracks in the presence of other stress raisers including those arising from geometry and loading [191].

According to Muskhelishvili's complex function, stresses for two-dimensional equations of elasticity can be defined in terms of two functions, Airy stress function $\boldsymbol{\Phi}$ and function $\boldsymbol{\psi}$. The functions $\boldsymbol{\Phi}$ and $\boldsymbol{\psi}$ are given in terms of two analytical functions $\emptyset(\boldsymbol{z})$ and $\boldsymbol{\chi}(\boldsymbol{z})$ of the complex variable $\boldsymbol{z} = \boldsymbol{x} + \boldsymbol{iy}$. So, the stress function takes the form,

$$\boldsymbol{\Phi} = \boldsymbol{Re}\{\bar{\boldsymbol{z}}\emptyset(\boldsymbol{z}) + \boldsymbol{\chi}(\boldsymbol{z})\} \quad \textbf{[3.8]}$$

and,

$$\boldsymbol{\psi} = \boldsymbol{Im}\{\bar{\boldsymbol{z}}\emptyset(\boldsymbol{z}) + \boldsymbol{\chi}(\boldsymbol{z})\} \quad \textbf{[3.9]}$$

where $\boldsymbol{Re}$ and $\boldsymbol{Im}$ denote the real and imaginary parts in complex notation respectively, and the bar over $\boldsymbol{z}$ denotes the conjugate.

Substituting equation [3.8] and [3.9] in equation [2.11], the stress fields in terms of functions $\emptyset(\boldsymbol{z})$ and $\boldsymbol{\chi}(\boldsymbol{z})$ are given by,

$$\boldsymbol{\sigma_x + \sigma_y} = \mathbf{2}\left[\emptyset'(\boldsymbol{z}) + \overline{\emptyset'(\boldsymbol{z})}\right] = \mathbf{4}\boldsymbol{Re}\{\emptyset'(\boldsymbol{z})\} = \mathbf{4}\boldsymbol{Re}\{\phi(\boldsymbol{z})\}$$

where $\phi(\boldsymbol{z}) = \emptyset'(\boldsymbol{z})$, with the prime denoting differentiation with respect to $\boldsymbol{z}$. By substituting equation [3.8] in equation [2.10] gets,

$$\boldsymbol{\sigma_y - \sigma_x + 2i\sigma_{xy}} = \mathbf{2}[\bar{\boldsymbol{z}}\emptyset''(\boldsymbol{z}) + \boldsymbol{\chi}''(\boldsymbol{z})] = \mathbf{2}[\bar{\boldsymbol{z}}\phi'(\boldsymbol{z}) + \boldsymbol{\psi}(\boldsymbol{z})] \quad \textbf{[3.10]}$$

where, $\boldsymbol{\psi}(\boldsymbol{z}) = \boldsymbol{\chi}''(\boldsymbol{z})$. The functions $\phi(\boldsymbol{z})$ and $\boldsymbol{\psi}(\boldsymbol{z})$ are known as Muskhelishvili's complex potentials.

FATCAT uses Muskhelishvili's mathematical model to evaluate stress field. Based on this approach, the state of stress can be derived from the mathematical theory of elasticity for isotropic materials using two analytical complex functions $\emptyset(\boldsymbol{z})$ and $\boldsymbol{\psi}(\boldsymbol{z})$ with $\boldsymbol{z = x + iy}$.

$$\left.\begin{aligned} \boldsymbol{\sigma_{yy}} &= \boldsymbol{Re}[\emptyset(\boldsymbol{z})] + \boldsymbol{2yIm}[\emptyset'(\boldsymbol{z})] + \boldsymbol{Re}\left[\overline{\boldsymbol{\psi}(\boldsymbol{z})}\right] \\ \boldsymbol{\sigma_{xx}} &= \boldsymbol{3Re}[\emptyset(\boldsymbol{z})] - \boldsymbol{2yIm}[\emptyset'(\boldsymbol{z})] - \boldsymbol{Re}\left[\overline{\boldsymbol{\psi}(\boldsymbol{z})}\right] \\ \boldsymbol{\tau_{xy}} &= \boldsymbol{-2yRe}[\emptyset'(\boldsymbol{z})] + \boldsymbol{Im}\left[\overline{\boldsymbol{\psi}(\boldsymbol{z})}\right] - \boldsymbol{Im}[\emptyset(\boldsymbol{z})] \end{aligned}\right\} \quad \textbf{[3.11]}$$

where x and y are Cartesian co-ordinates, the prime denotes differentiation and the overbar denotes the complex conjugate [192]. It is assumed that the state of stress at a crack tip in the cracked body can be represented by the state of stress at the tip of a centre crack in an infinite plate in a generalised state of stress as shown in Fig 3.9(a) [193]. To determine the generalised state of stress at the crack tip, the complex stress functions $\emptyset(\boldsymbol{z})$ and $\boldsymbol{\psi}(\boldsymbol{z})$ are written in a series form. Then, the boundary conditions for the crack surfaces are satisfied through the use of conformal mapping in which a circle in the mapping plane is mapped onto a geometrical shape in the physical plane through the mapping function,

$$\boldsymbol{z = \omega(\xi) = R\left(\xi + \frac{m}{\xi}\right)} \qquad \boldsymbol{(0 \le m \le 1)} \qquad \textbf{[3.12]}$$

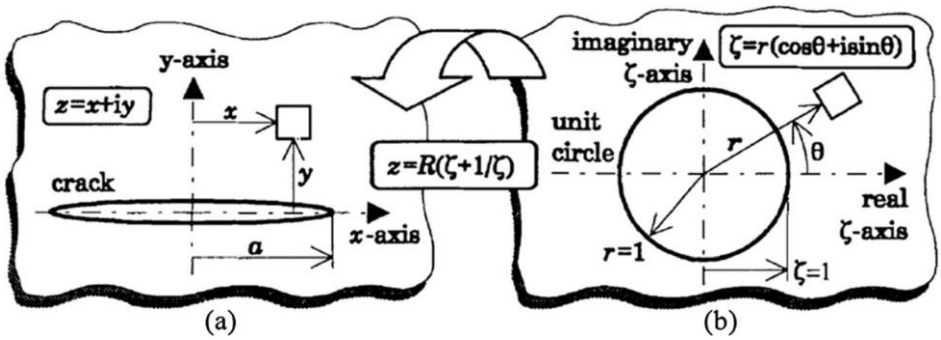

Fig 3.9: Crack coordinates system in (a) physical and (b) mapping planes [192]

where $\boldsymbol{\xi}$ is a complex variable in the mapping plane, $\boldsymbol{R}$ represents a length parameter, and $\boldsymbol{m}$ describes the shape of the mapped circle. The complex variable $\boldsymbol{\xi}$ is calculated from a system of polar co-ordinates ($\boldsymbol{r}$, $\boldsymbol{\theta}$) in the mapping plane using:

$$\xi = r\phi = r(cos\theta + isin\theta) \quad \textbf{[3.13]}$$

where ϕ is the complex co-ordinate of the unit circle ($r = 1$).

The principal stress sum can be found from equations **[3.4]** and **[3.7]** as

$$\Delta(\sigma_{xx} + \sigma_{yy}) = AS = 4Re[\emptyset(z)] \quad \textbf{[3.14]}$$

So, the problem is reduced to finding $\emptyset(z)$, which was achieved by Nurse and Patterson using a general form of the Fourier series and by satisfying boundary conditions explained above, they found, [192]

$$\emptyset(z) = A_0 + \frac{A_0+\bar{A}_0+\bar{B}_0}{\xi^2-1} + \sum_{N=1}^{\infty}\left(\frac{2N}{\xi^{2N}}\right)\left(\frac{\xi^2+1}{\xi^2-1}\right)\bar{A}_N - \frac{\bar{A}_N}{\xi^{2N}} - \frac{\bar{B}_N}{\xi^{2N}} + A_N\xi^{2N} \quad \textbf{[3.15]}$$

where ξ is a complex variable in the mapping plane related to the physical plane by the conformal mapping function (Fig 3.9),

$$\xi(Z) = \frac{z}{a} + \sqrt{\left(\frac{z^2}{a^2} - 1\right)} \quad \textbf{[3.16]}$$

A_N and B_N are unknown series parameters that are used to describe the generalised state of stress around the crack tip. The real parts A_N and B_N describe a mode I stress field and the imaginary parts describe a mode II stress field. The complex stress intensity factor $K_I + iK_{II}$ is calculated in the normal manner using the limiting value of $\emptyset(z)$ as $\xi \rightarrow \pm 1$,

$$\Delta(K_I + iK_{II}) = A_0 + \bar{A}_0 + \bar{B}_0 + 4\sum_{N=1}^{\infty}(A_N) \quad \textbf{[3.17]}$$

By solving Equations [3.13] and [3.14], FATCAT evaluates stress intensity factors from thermoelastic data in the form of ΔK_I and ΔK_{II} in MPa$\sqrt{\text{m}}$. Thermoelastic data is collected in the form of an array of approximately 100 data points surrounding the crack tip. The mapping function $\xi(Z)$ is used to convert the data into ξ −co-ordinates for the mapping plane. The series of coefficients A_N and B_N are solved using a least squares approach which minimises the

difference between the data and the stress field equations. Statistical calculations are performed and the mean ($\boldsymbol{\mu}$) and variance ($\boldsymbol{s}$) of the least-squares fit of the solution to the data points are found. By using this mean ($\boldsymbol{\mu}$) and variance ($\boldsymbol{s}$), the stress intensity factors were calculated with 95% confidence limits,

$$(\mathbf{1}+\boldsymbol{\mu}-\mathbf{2}\boldsymbol{s})\boldsymbol{K_S} \leq \boldsymbol{K} \leq (\mathbf{1}+\boldsymbol{\mu}+\mathbf{2}\boldsymbol{s})\boldsymbol{K_S} \quad \textbf{[3.18]}$$

where $\boldsymbol{K_S}$ is the solution of least square method.

3.4.5.2 Crack tip position

Direct observation of the crack tip is often difficult since data very near the crack tip tend to be blurred as a result of plasticity and the presence of high stress gradients. To find the crack tip from TSA data, two methods have been implemented in FATCAT. The first method considers the crack tip co-ordinates as two unknowns in the equations and solves the equations to determine both the Fourier series coefficients and the crack tip position using a Downhill Simplex method [194]. The other method is based on a Genetic Algorithm (GA) optimization in which a point in the image was used as an initial value for the GA [195]. Then the crack tip position found using GA was used in the algorithm to find the stress intensity factors.

3.4.5.3 Selection of data points

To calculate $\boldsymbol{\Delta K}$ using TSA, it is required to obtain a thermoelastic map of the region near the crack tip. Subsequently, a set of data points has to be collected in the region surrounding the crack tip. It is important to avoid collecting data points at those locations affected by near crack tip plasticity. To identify such a region, Stanley and Chan's methodology was employed [196]. Their method combines equation **[3.4]** with a mathematical expression describing the sum of principle stresses derived from Westergaard's model (equations **[3.17(a)]** and **[3.17(b)]**).

$$\Delta(\boldsymbol{\sigma_x}+\boldsymbol{\sigma_y}) = \boldsymbol{AS} = \frac{\mathbf{2}\boldsymbol{\Delta K_I}}{\sqrt{\mathbf{2}\boldsymbol{\pi r}}}\boldsymbol{cos}\left(\frac{\boldsymbol{\theta}}{\mathbf{2}}\right) - \frac{\mathbf{2}\boldsymbol{\Delta K_{II}}}{\sqrt{\mathbf{2}\boldsymbol{\pi r}}}\boldsymbol{sin}\left(\frac{\boldsymbol{\theta}}{\mathbf{2}}\right) \quad \textbf{[3.19]}$$

In pure mode I loading conditions, Stanley and Chan observed that the maximum thermoelastic signal, S_{max}, occurred at a 60° angle with respect to the crack. Considering this criteria, equation **[3.19]** can be rearranged into a linear equation relating the distance from the crack tip,

$$y = \left(\frac{2\sqrt{3}K_I^2}{4\pi A^2}\right)\frac{1}{S_{max}^2} \qquad \textbf{[3.20]}$$

This relationship is linear only in the singularity dominated elastic field which defines the region over which data can be collected to fit the stress field equations described by Muskhelishvili's model. The thermoelastic image is plotted using the above relationship where three different regions can be identified as shown in Fig 3.10. A pair of red lines is superimposed on these data points to identify the linear region of the plots which corresponds to the singularity-dominated elastic field. The far-left region has no linear behaviour since there is a loss of adiabatic conditions due to high stress gradients and crack tip plasticity (denoted as the plastic region in Fig 3.10). The middle region shows the linear behaviour and the mathematical model prevails in this region and so the data points were selected from this region. The far-right region is a non-singularity dominated elastic region where the proposed mathematical model is not valid because the mathematical model assumes that the singular term is dominant.

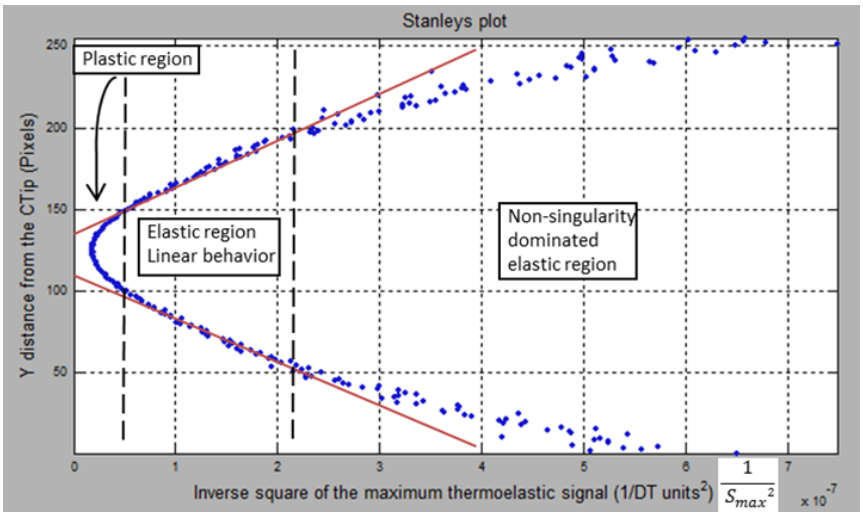

Fig 3.10: Graph showing the linear relationship between the vertical distance from the crack tip and $\frac{1}{S_{max}^2}$ employed in the methodology of Stanley and Chan for the calculation of the stress intensity factor from thermoelastic data

3.4.5.4 Location of crack tip based on phase angle data

Fig 3.11(a) represents the TSA phase image showing the distribution of the phase angle in the vicinity of a crack tip. Phase angle values along a line through the crack path shown by the arrow in the 3.11(a), are plotted in the graph of 3.11(b). It is noticeable from the figure that the phase angle is reasonably uniform in the far-field and deviates around zero satisfying the adiabatic condition. The phase angle shows shifts from zero to positive and negative along the crack and a small region ahead of the crack respectively.

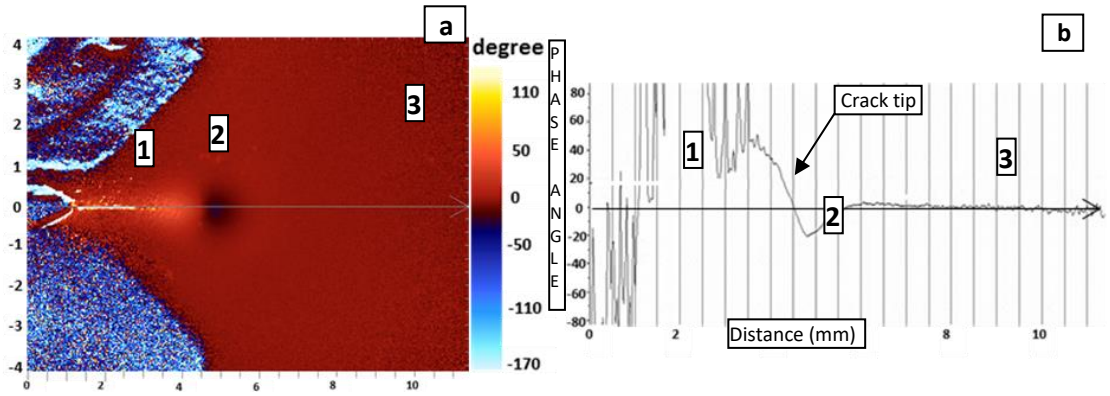

Fig 3.11: (a) Phase difference of a CT specimen, most of the area is in phase and the crack and a small region ahead of crack is out of phase. (b) A line profile passing through the crack reveals the positive phase [1], negative phase [2] and zero phase [3] area in the right image indicating crack wake, cyclic plastic zone and elastic region respectively

There are three regions evident in the Figure 3.11[b],

1) Region of positive phase: The region [1] showing positive phase attributed to crack wake. These positive values of phase angle are associated with a loss of adiabatic conditions caused by contact between the residual plastic materials in the crack wake. Contact between the crack flanks will generate heat due to friction causing the loss of adiabacity.
2) Region of negative phase: The region [2] has negative phase attributed to the cyclic plastic zone. The change in the phase angle indicates a loss of adiabatic conditions in this region due to heat generation associated with plastic work. The dislocation movement in the plastic region ahead of the crack will generate heat during the loading

part of the fatigue cycle. During the unloading part of the cycle, frictional heating due to contact of the crack flanks causes the loss of adiabacity. Since these two instances of heat generation occur in opposite parts of the loading cycle, they would be expected to produce phase deviations of opposite signs. The point at which the phase angle changes from negative to positive was taken to be a first approximation of the crack tip location by Diaz et al. [172]

3) A region of zero phase: The far field region [3] shows that the phase angle is reasonably uniform which is associated with the elastic field.

3.4.6 Characterisation of plastic zone

The TSA phase image achieved from fatigue test of CT specimen is shown in Fig 3.12(a). It is possible to identify the plastic zone by applying a binary filter to the phase image to indicate the negative phase region as proposed by Patki and Patterson [113].

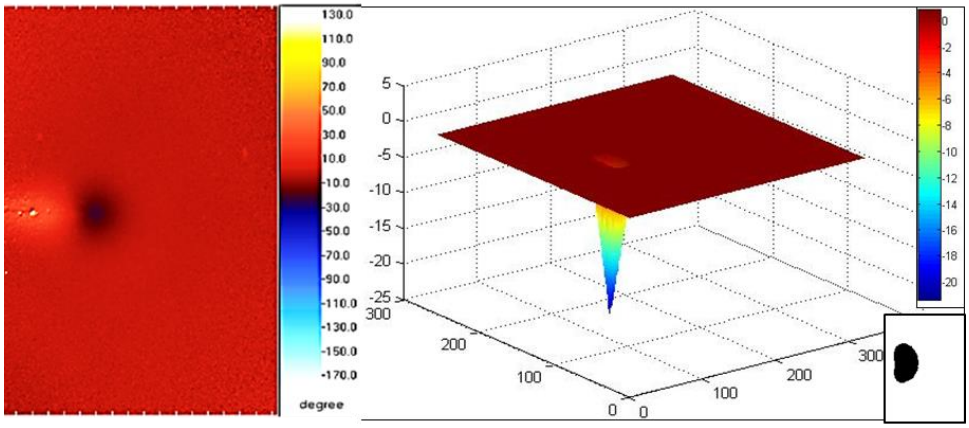

Fig 3.12: (a) TSA phase image and (b) 3D representation of plastic region after applying a binary filter ahead of the crack. The inset shows the plastic zone in 2D

The black region of the binary image (Fig 3.12(b) inset) corresponds to the plastic zone at the crack tip and was used to calculate the area of the plastic zone and an experimental value for the radius of plastic zone, which was taken as the distance across the area from the crack tip in the direction of crack growth. Fig 3.12(b) represents the plastic zone in 3D.

3.5 Back-Scattered Electron image Analysis (BSEIA)

The scanning electron microscope (SEM) is one of the most versatile instruments for investigating the microstructure of metallic materials. Accelerated electrons in an SEM carry significant amounts of kinetic energy, and this energy is dissipated as a variety of signals produced by electron-sample interactions when the incident electrons are decelerated in the sample. These signals include secondary electrons (that produce SEM images), backscattered electrons (BSE), diffracted backscattered electrons (EBSD that are used to determine crystal structures and orientations of minerals), photons (characteristic X-rays that are used for elemental analysis and continuum X-rays), visible light (cathodoluminescence–CL), and heat [197]. Among these, secondary electrons and backscattered electrons are commonly used for imaging samples. The primary backscattered electrons (BSE), undergo elastic Rutherford scattering from the nuclei of the atoms of the sample. As the size of the nuclei gets larger, the BSE emission increases in a nearly linear fashion. Thus, for a flat polished sample containing numerous phases, secondary electrons produce little or no contrast (as the scattering is not from nuclei but from surrounding protons and electrons), while the primary BSE signal could produce high contrast. Small surface features that are indistinct in a secondary image can be viewed clearly in a BSE image. So, BSE images are selected to quantify the plastic zone.

Scanning electron microscope is an emerging tool for mapping elastic strains at mesoscopic and microscopic scales and to reveal microstructural mechanisms of deformation [198-201]. The generation and motion of dislocations close to fatigue cracks controls the cyclic propagation of fatigue crack so these dislocations have fundamental importance. This local plastic deformation modifies the stress intensity experienced by the crack tip, either by blunting the crack or through the action of the dislocation stress fields which can shield the crack from the external load [202]. Joy and Bieber et al. observed the phenomenon of a contrast change

in BSE images during plastic deformation in 1975 and 2009 respectively [203, 204]. Even though this phenomenon has been speculated about previously, it has never been used to quantify the strain levels associated with localized plastic deformation. Yang et al. observed a gradual change in the sharpness of the BSE images with distance from the crack tip and they quantified the plastic strain distribution at the tip of a fatigue crack by processing an array of BSE images as son in Fig 3.13 [144]. Similar results were evident while observing an array of BSE images captured for the current research. At large distances from the crack tip, the BSE images displayed sharp, well-defined features allowing easy identification of the individual grains. In BSE images acquired close to the crack tip, however, large variations in brightness were evident within individual grains, making the individual grains less distinct and with lower contrast as a result of residual plastic strain within these grains. These contrast changes in BSE images can eventually lead to a change in the signal frequency distribution of features within the corresponding images. Therefore, by quantifying the frequency distribution of the BSE images, it is possible to relate it directly to the extent of plastic deformation (detailed in following sections). In the current project, features of the Fourier transform of backscattered electron (BSE) images have been used to characterise the plastic zones before, during and after the application of overload.

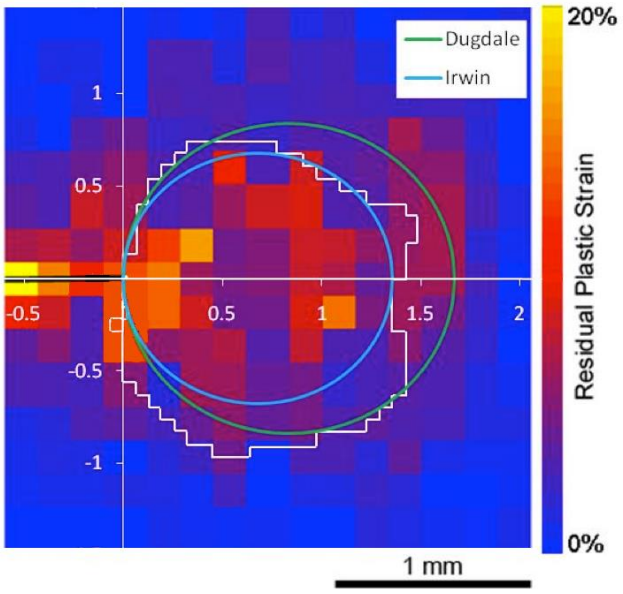

Fig 3.13: Map of plastic strain around the crack tip based on the FWHM of the DFTs of images. The white line shows the measurement of plastic zone using TSA data. The green and blue solid lines indicate the theoretical estimations of the plastic zone size based on Dugdale's and Irwin's approaches, respectively [144].

3.5.1 Equipment

The JEOL JSM-7001F field emission ultra-high resolution scanning electron microscope located in the Electron Microscopy Centre, Plymouth University was used to capture the BSE images. Backscattered electrons (BSE) were accelerated with a voltage of 20 kV, over a working distance of 15 mm. BSE images (640 × 480 pixels) were captured using an external computer. Fig 3.14 shows the JEOL JSM-7001F field emission scanning electron microscope situated at Plymouth University.

Fig 3.14: JEOL JSM-7001F field emission scanning electron microscope [205]

3.5.2 BSE Image Analysis – Fourier Transform

The BSE images were analysed using the Fourier Transform. The Fourier Transform is a function derived from a given function and representing it by a series of sinusoidal functions. It can decompose an image into its sine and cosine components. The output of the transformation represents the image in the Fourier or frequency domain, while the input image is the spatial domain equivalent. DFT is the Discrete version of Fourier Transform that transforms a signal from Time Domain representation to its Frequency Domain representation, while Fast Fourier Transform (FFT) is an algorithm for the calculation of DFT. In the Fourier domain image, each point represents a particular frequency contained in the spatial domain image. The DFT is the sampled Fourier Transform and therefore does not contain all of the frequencies forming the image, but only a set of samples which is large enough to describe the spatial domain image. The number of frequencies corresponds to the number of pixels in the spatial domain image, i.e. the image in the spatial and Fourier domain are of the same size. For a square image of size N×N, the two-dimensional DFT is given by

$$F(k,l) = \sum_{i=0}^{N-1} \sum_{j=0}^{N-1} f(i,j) e^{-i2\pi(\frac{ki}{N}+\frac{lj}{N})} \quad \textbf{[3.21]}$$

where the exponential term is the basis function corresponding to each point $F(k,l)$ in the Fourier space. The equation can be interpreted as, the value of each point $F(k,l)$ obtained by multiplying the spatial image with the corresponding base function and summing the result. The base functions are sine and cosine waves with increasing frequencies, i.e. $F(0,0)$ represents the DC-component of the image which corresponds to the average brightness and $F(N-1,N-1)$ represents the highest frequency. The Discrete Fourier Transformation of a two-dimensional image gives complex-number images, i.e. two images are generated, the magnitude map and the phase map. Fig 3.15(a) is the original BSE image of the Titanium CT specimen. The images were cropped in the centre region to eliminate the edge effect (the electron beam diffracted by sharp edges causing a decrease in focus). The image was cropped to square shape in order to allow the origin in the centre. For non-square image, the FFT will be isotropic (X and Y scales the same) but truncated in one dimension which will introduce noise. To eliminate the edge effect and noise, the BSE image was cropped to a square of 345x345 pixels from the centre region Fig 3.15 (b). Fig 3.15(c) and (d) show the magnitude map and phase map respectively.

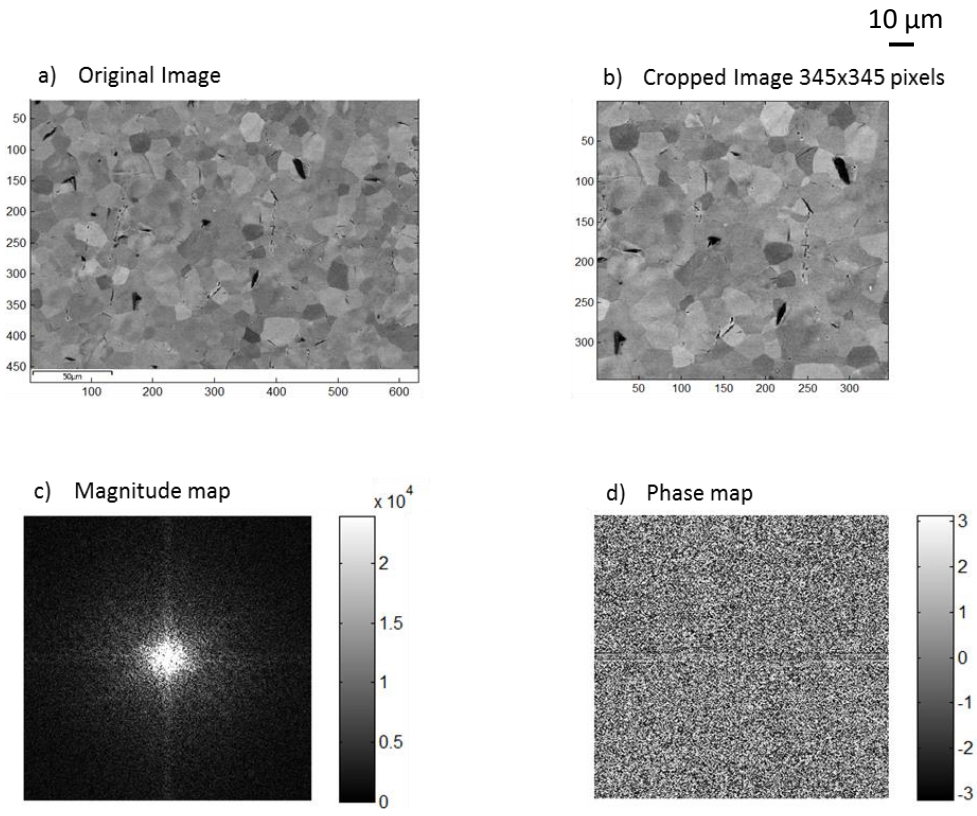

Fig 3.15: (a) Original BSE image of Ti CT specimen (b) Image was cropped from centre region to run the FFT algorithm (c) Resulting magnitude map after running FFT (d) resulting phase map of the image

The magnitude of a DFT provides the distribution of the frequency components in the original image, while the phase of the DFT gives the locations of frequency components in the original image.

DFT was conducted on all BSE images using MATLAB built-in functions. First, the MATLAB function ‘fft2’ was used to compute the complex-number DFT images of the BSE images using the fast Fourier transformation (FFT) algorithm. Fig 3.16 shows the resulting images after applying the particular function to the BSE image displayed in Fig 3.16(a). The first function applied was ‘fft2’ resulting in the image as shown in Fig 3.16(b).

The resulting image in Fig 3.16(b) has zero- frequency components at the corners of an image so the function ‘fftshift’ was applied to improve the output image quality i.e. shifting

the zero frequency to the DFT image centre. Fig 3.16(c) has the scale of $x10^4$, so the 'log2' function was applied to enlarge the detailed frequency information (Fig 3.16(d)).

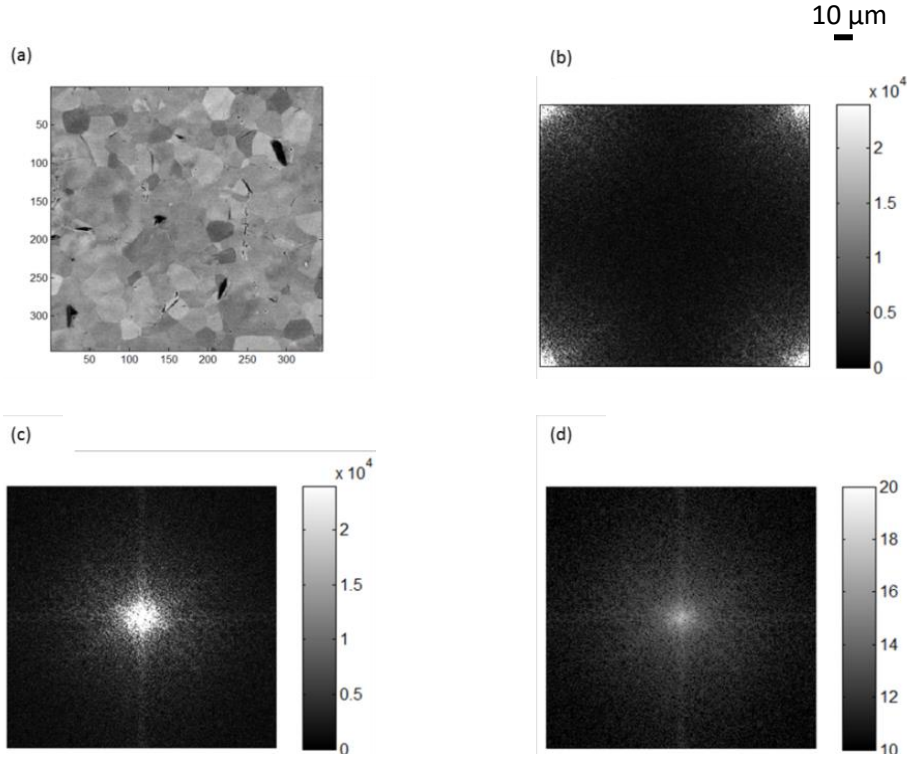

Fig 3.16: (a) A square BSE image with 345x345 pixels (b) Magnitude map of the image after applying 'fft2' MATLAB function (c) Magnitude map of the image after applying 'fftshift' MATLAB function shifting the zero frequency in centre (d) Magnitude map of the image after applying 'log2' MATLAB function enlarging the frequency information

Fig 3.17 shows the process to find the Full Width at Half Maximum (FWHM) which is the difference between the two extreme values of the independent variable at which the dependent variable is equals to half of its maximum value. Fig 3.17(a) and (b) shows the BSE image and its corresponding FFT respectively. Fig 3.17(c) represents the profile of a line passing through the centre of the FFT image.

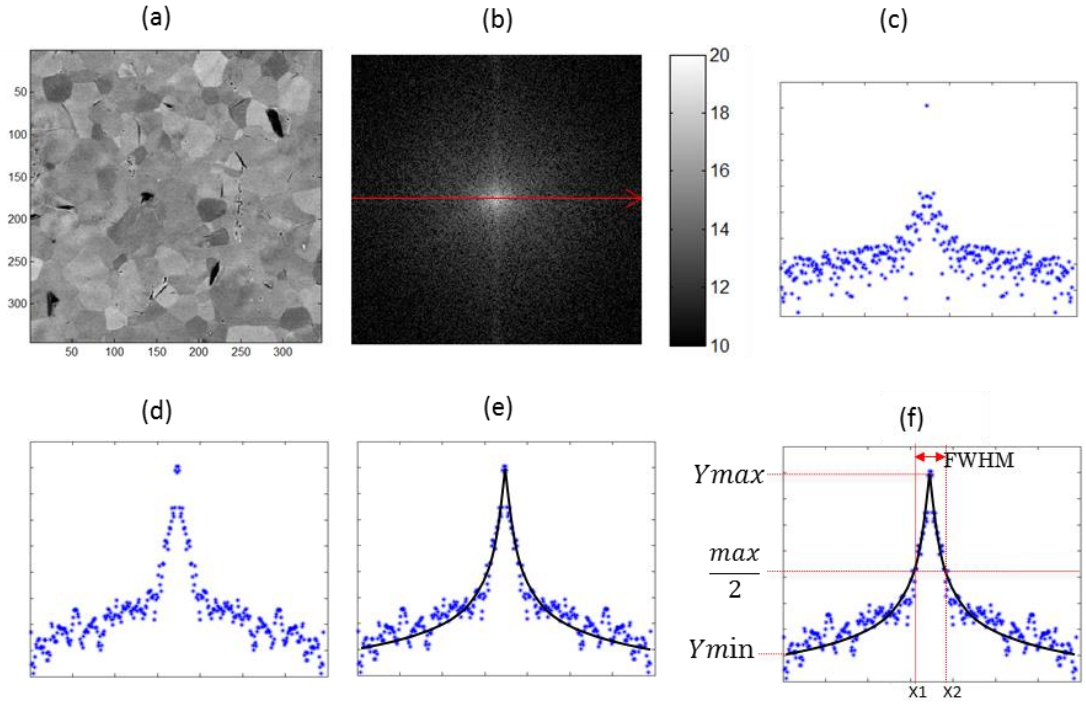

Fig 3.17: (a) A square BSE image with 345x345 pixels (b) FFT of the image. A red arrow shows the line profile across the centre of the image (c) the original FFT of line profile (red line in previous image) (d) the line profile was smoothed using a MATLAB 'moving average' filter (e) the exponential curves were then fitted to each side of the image. (f) The FWHM was found by calculating the distance between the X1 and X2 points

It is evident from the image that the line profile is symmetric so it is possible to consider the symmetry and find the FWHM manually as detailed in previous research where the FWHM of each image was found individually adding a considerable amount of time and labour [144]. This process also includes the selection of a baseline manually that introduced a manual error. To eliminate all these disadvantages, a special MATLAB program was developed to find the FWHM of all the images. The FWHMs achieved using the program was compared to the FWHMs found manually for several images and the results were same, so FWHM of rest of the images were found using the MATLAB program. The program took only a couple of minutes to find the FWHM of 100 images. First, the FFT of the image was calculated followed by a line profile passing through the centre of each image. The line profile was then smoothed using the MATLAB 'moving average' filter for span of 5, i.e. the data were smoothed by replacing each point with the average of the neighbouring 5 data points where the data point was at the centre of the span. This process enables the creation of an approximating function

that attempts to capture the important patterns in the data, while leaving out noise. Fig 3.17(d) shows the smoothed data with a considerable reduction in noise. Finally, an exponential curve was fitted to the data on each side of the image as shown in Fig 3.17(e). To find the FWHM, the maximum value of *Ymax* was selected and subtracted from the *Ymin* to get the half value (max/2) as shown in Fig 3.17(f). The value max/2 corresponds to the X1 and X2 points on the exponential curves. The difference between the X1 and X2 points gives the FWHM.

3.5.3 Calibration

To quantify the relationship between the residual plastic strain level in a BSE image and the FWHM of its DFT magnitude, the in-situ uniaxial tensile test was performed on the tensile specimens of three different materials. Fig 3.18 shows the GATAN Microtest™2000EW tensile loading stage with specimen mounted on the sample grips angled at 70 degrees [206]. The standard grips in a horizontal position were available but there was not enough working distance between the detector and the specimen to capture the BSE images so, the angled grips were selected for the tensile tests. The tensile specimens were metallographically prepared in the same manner as the CT specimens as explained earlier in the specimen preparation section.

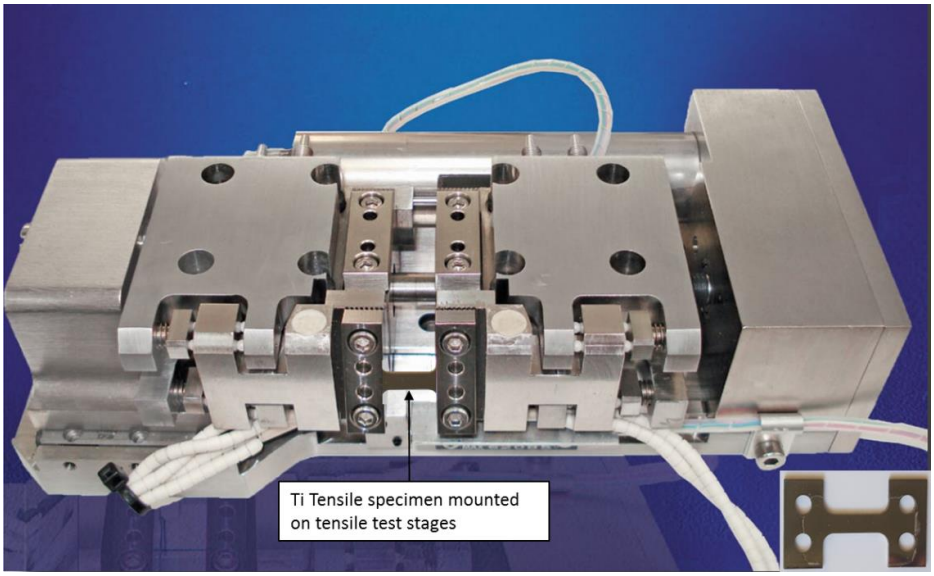

Fig 3.18: GATAN Microtest™2000EW tensile loading stage showing the tensile specimen mounted on the 70-degree angled grips [206]

The tensile specimen was 3 mm wide and had a 6.5 mm gauge length with 8 mm of reduced section length as shown in Fig 3.19. The tensile test was performed in force control mode with a motor velocity of 0.4 mm/min at room temperature.

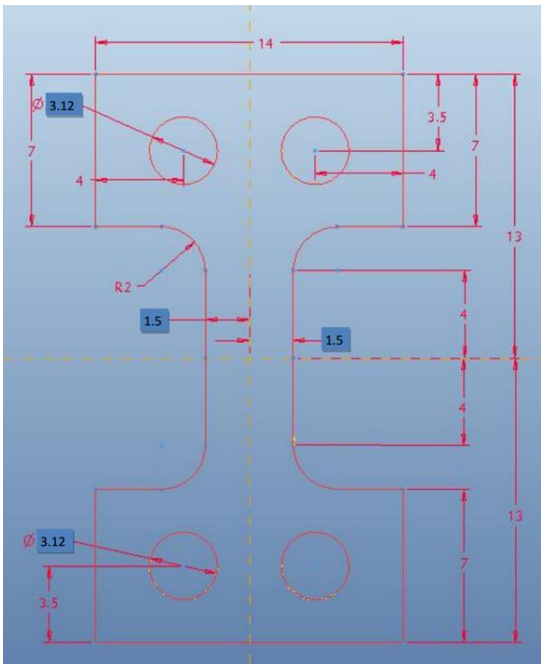

Fig 3.19: Geometry of in-situ tensile test specimen (all dimensions are in mm)

The extension between the jaws was measured by the extensometer mounted on the stage. The BSE images were captured for 8 strain increments i.e. 0%, 4%, 8%, 11%, 14%, 16.5%, 18.5% and 24.5% under the identical imaging conditions (brightness, contrast, magnification, and working distance) as those for the fatigue specimen.

Fig 3.20 shows the engineering stress-strain curve of a Titanium tensile specimen. The blue crosses denote the strain increments at which the in-situ test was interrupted and BSE images were captured. At zero strain, 8 BSE images were captured from the centre section of the tensile specimen as shown in Fig 3.21. At each increasing strain, 8 BSE images were captured at the same location resulting in 64 BSE images in total.

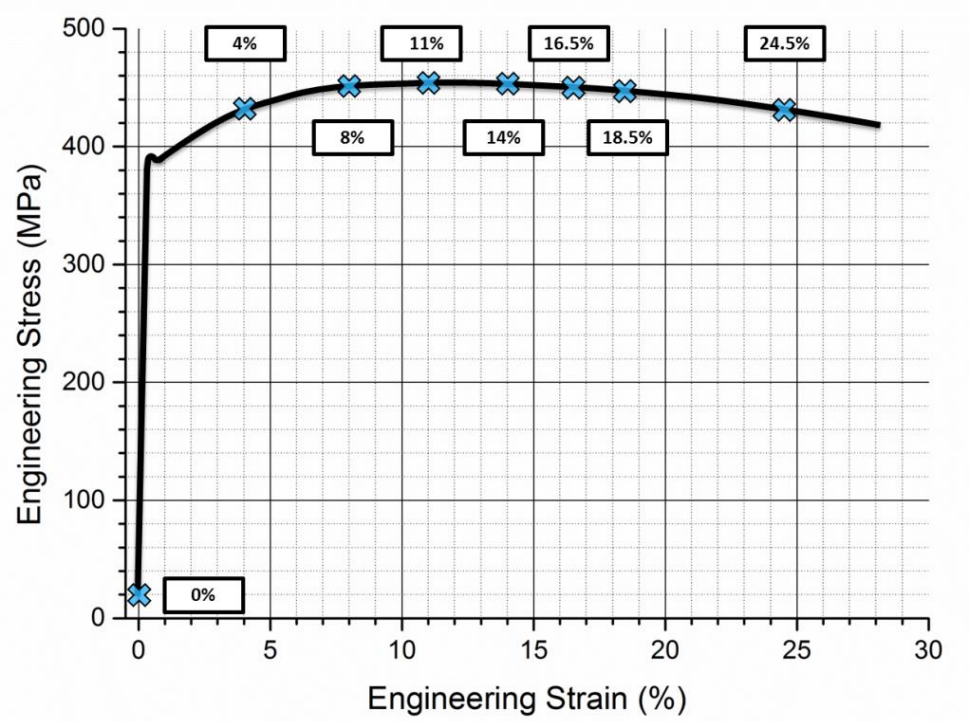

Fig 3.20: Engineering stress-strain curve obtained for the pure Titanium. The blue cross indicates the strain increment at which the in-situ uniaxial tensile test was interrupted to collect the BSE images.

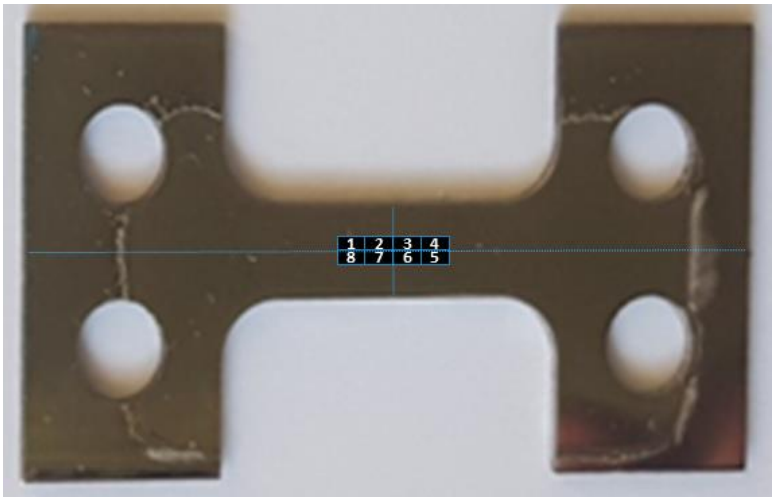

Fig 3.21: In-situ tensile specimen showing the location from where the BSE images were captured at each strain level (for illustration purpose only not to the true scale)

Fig 3.22 shows the BSE images from position 1, 2 and 3 from Fig 3.21 at different strain levels. The evolution of microstructural features is evident from the figure. As the strain level increases, the contrast within the grains increases.

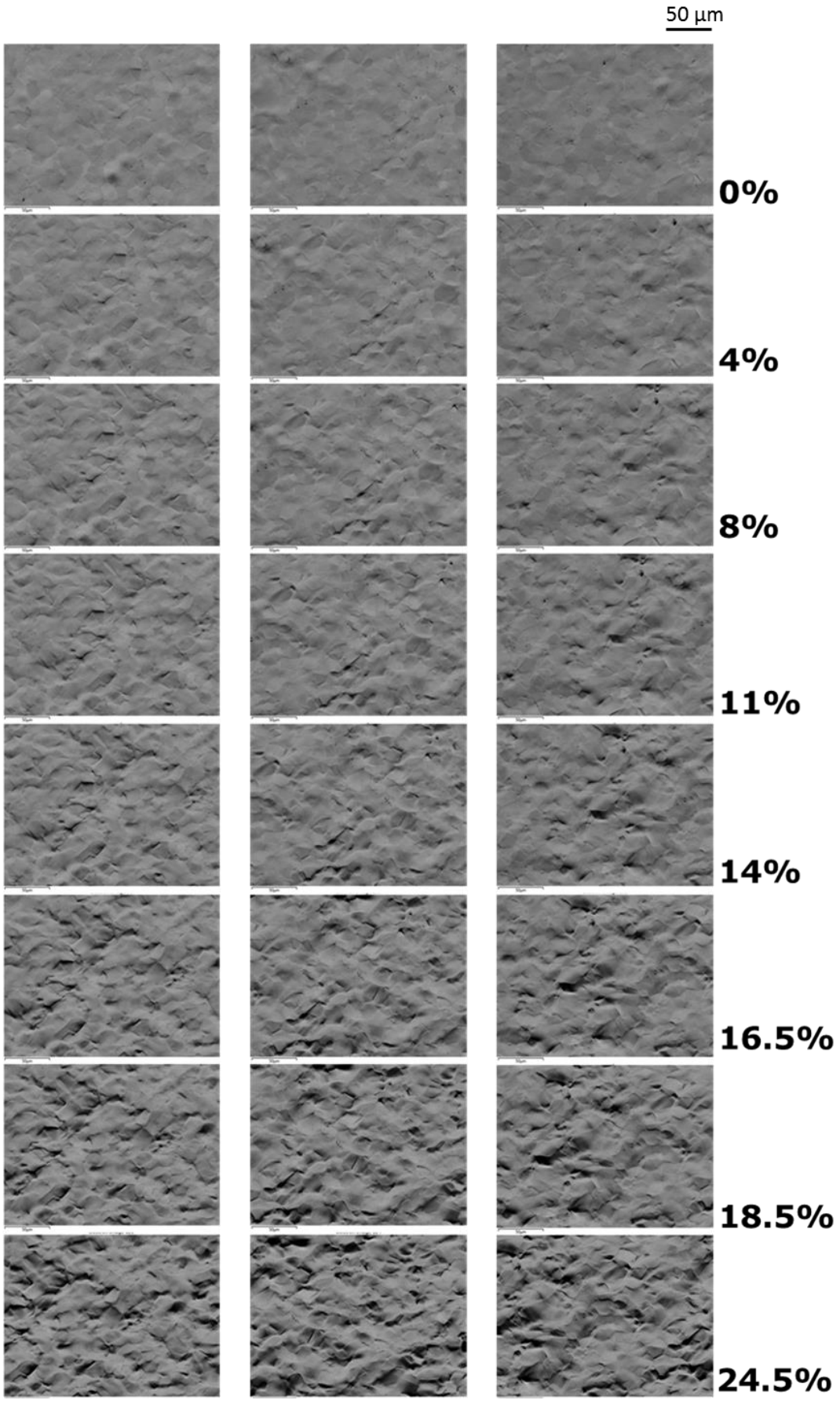

Fig 3.22: BSE images at different strain levels during in-situ tensile test indicating evolution of microstructure features at 3 different locations

All the 64 images at increasing strain levels from 8 different locations were processed using the procedure described in the previous section (calculation of FWHM). The mean FWHM of the DFT from eight BSE images at each strain increment were plotted, as shown in Fig 3.23 and a polynomial fitted to create a calibration curve that was used to determine the residual plastic strain field of the fatigued specimen. The error bars represent the standard deviation of FWHM from the mean FWHM calculated at each strain from 8 BSE images.

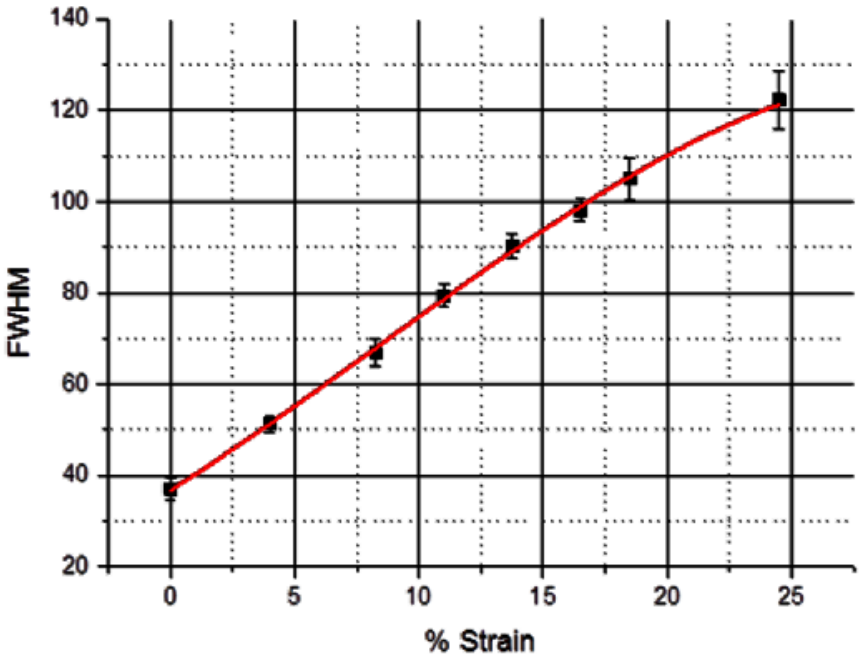

Fig 3.23: The full width of half the maximum of the DFT as a function of the engineering strain based on BSE images captured at various plastic strain during an in-situ tensile test.

The top row of Fig 3.24 represents the BSE images at 0%, 8%, 11%, 16.5% and 18.5% strain levels at location 1 from Fig 3.24. The middle row of Fig 3.24 shows the corresponding DFT of the images and with lines passing through their centres. The bottom row indicates corresponding line profile of DFT image (black squares), smoothed data (red squares) and an exponential curve (green curve) fitted to the smoothed data to find the FWHM. It is evident from the figure that as the % strain increases the DFT profile changes. The contrast of the images increases from zero strain to higher strain levels which results in the distinct centre of the DFT profiles. The observation of the line profiles indicate that, at zero strain, the distance

between the data points is less which increases at higher strain levels resulting in a higher FWHM.

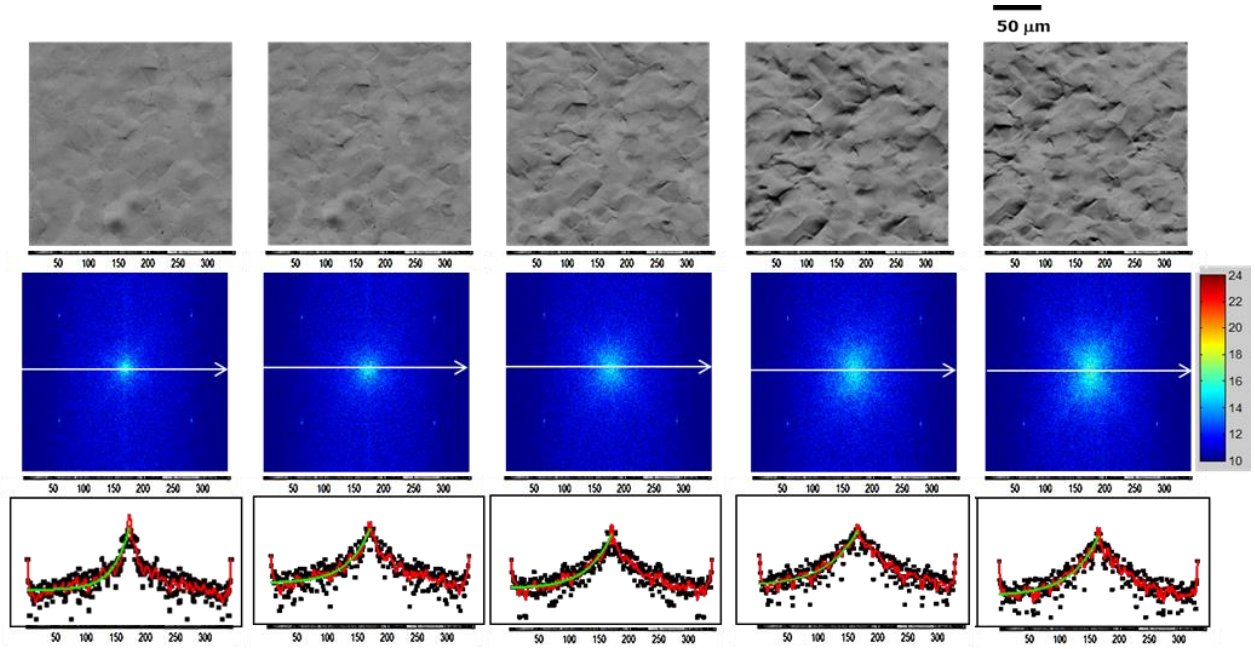

Fig 3.24: Top row reprints the BSE images at 0%, 8%, 11%, 16.5% and 18.5% strain levels. Middle row shows the DFT profiles of BSE images. The bottom row shows the data points for the line profile (black dots), smoother data points (red dots) and an exponential curve (green). The distance between the two data sets increases at higher strain levels resulting in higher FWHM

Chapter 4

Results and Discussions

4.1 Thermoelastic Stress Analysis (TSA)

In the current research, the previously well-established techniques – TSA and BSEIA have been employed [113, 144, 172, 211]. The use of phase data to identify the plasticity in TSA method has been used in the past by several researchers. Diaz et al. located the crack tip in recorded thermal images of the specimen and identified plasticity from the map of phase difference between the applied load and surface temperature obtained from TSA signals [172]. Tomlinson et al. used the TSA phase data to quantify the size and shape of the crack-tip plastic zone in two different aerospace materials at a range of frequencies [211]. Patki and Patterson studied the effect of overloads on stress intensity factors and plastic zone size for the first time. They developed a technique to measure the radius of the plastic zone directly from the phase information [113]. Yang et al. used the BSEIA method to identify the plastic strain map and verified the results using the TSA technique [144]. The same experimental techniques and methodology have been employed in current research for varied materials having different strain hardening exponents at different loading conditions.

CT specimens of 3 different materials – pure Titanium, Al 2024-T3 and Al 6061-T6 were manufactured based on the BS-ISO 12108:2012 standard as described in the previous section (section 3.2 and 3.3) whose value of strain hardening exponent was 6, 8 and 14 respectively. The specimens were loaded in a uniaxial INSTRON ELECTROPULSE-E3000 loading frame. A cyclic load with a mean of 92% of yield stress was applied at a frequency of 20 Hz for each material at varying load ratio. The crack was initiated from the notch and TSA

data were collected after crack growth of 3.0 mm. Fifteen different specimens were tested using the parameters provided in Table 3. The full-field stress maps around the crack tip were processed using a freely available software package, FATCAT (www.experimentalstress.com) to evaluate the range of stress intensity factor, ΔK_I.

The experimental results from specimen numbers 4, 5 and 6 from table 3 are shown in Figs. 4.1 and 4.2. Fig 4.1 shows a comparison of theoretical and experimental plastic zone radius as a function of crack length. The theoretical radius of the crack tip plastic zone, r_p was calculated using, [19]

$$r_p = \frac{1}{\pi}\left[\frac{\Delta K_I}{\sigma_y}\right]^2 \qquad \textbf{[4.1]}$$

where σ_y is yield stress. The experimental crack tip plastic zone radius was estimated from the phase information as described earlier using a specially written MATLAB program. The experimental plastic zone was calculated by following the methodology in previous chapter demonstrated by Fig 3.11 and 3.12. A simple threshold was applied to the phase data to identify crack tip plastic zone which in the set-up used in these experiments always exhibited a negative phase difference. The error bars in figure 4.1 represents ±2 times the standard deviation, i.e. 95 per cent confidence limits, based on evaluations of the plastic zone radius obtained from three different threshold values (1 degree, 2 degree & 3 degree (Ref Fig 3.11)) Fig 4.1 suggests that the experimental plastic zone radius are in agreement with those calculated from theory for all three values of strain hardening exponent suggesting a high level of confidence in the method of determination of plastic zone radius found from TSA phase information. It is noticeable from Fig 4.1 that the difference between the theoretical and experimental plastic zone radius starts decreasing as the value of strain hardening exponent decreases. This phenomenon can be explained using Fig 4.2 which shows the experimental plastic zone radius at various values of strain hardening exponent at crack lengths of 6.4 mm, 6.7 mm, 7.0 mm and 7.3 mm.

Table 3: List of fatigue tests performed at various load ratios for constant amplitude loading and overload

Specimen	Loading Mean load = $\left[\frac{min+max}{2}\right]$ N	Load ratio R = $\frac{min}{max}$	Overload (% of amplitude)
1. Pure Ti	360	0.1	No overload
2. Al 2024-T3	309	0.1	
3. Al 6061-T6	249	0.1	
4. Pure Ti	360	0.33	No overload
5. Al 2024-T3	309	0.33	
6. Al 6061-T6	249	0.33	
7. Pure Ti	360	0.5	No overload
8. Al 2024-T3	309	0.5	
9. Al 6061-T6	249	0.5	
10. Pure Ti	360	0.33	50%
11. Al 2024-T3	309	0.33	50%
12. Al 6061-T6	249	0.33	50%
13. Pure Ti	360	0.33	10%
14. Al 2024-T3	309	0.33	10%
15. Al 6061-T6	249	0.33	10%

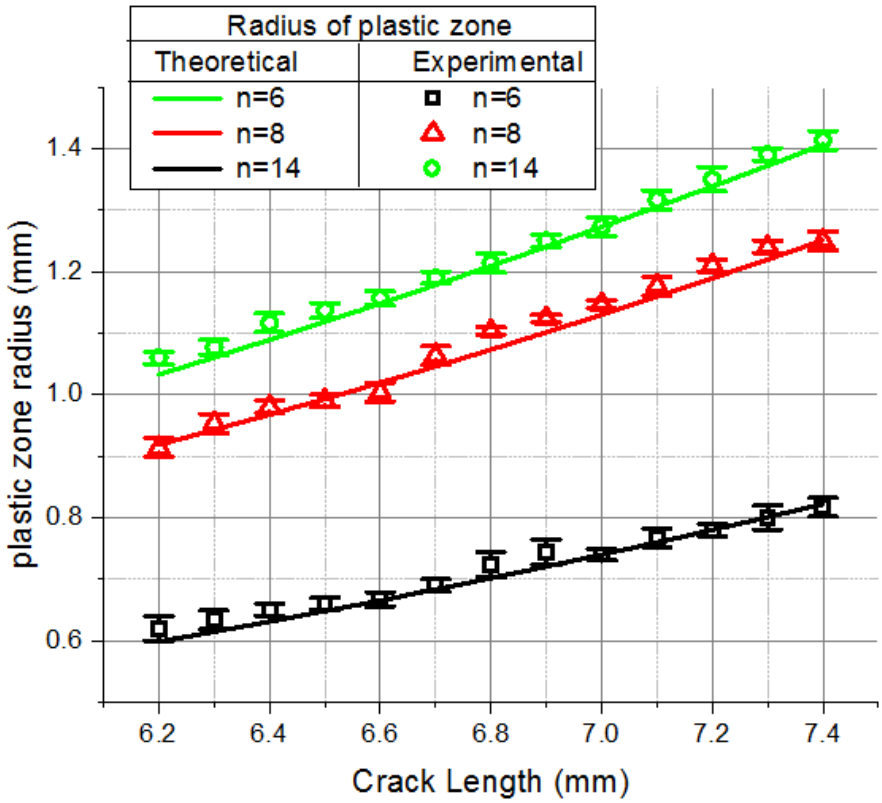

Fig 4.1: Comparison of experimental and theoretical plastic zone radius as a function of crack length for constant amplitude loading for value of strain hardening exponent n= 6, 8, 14

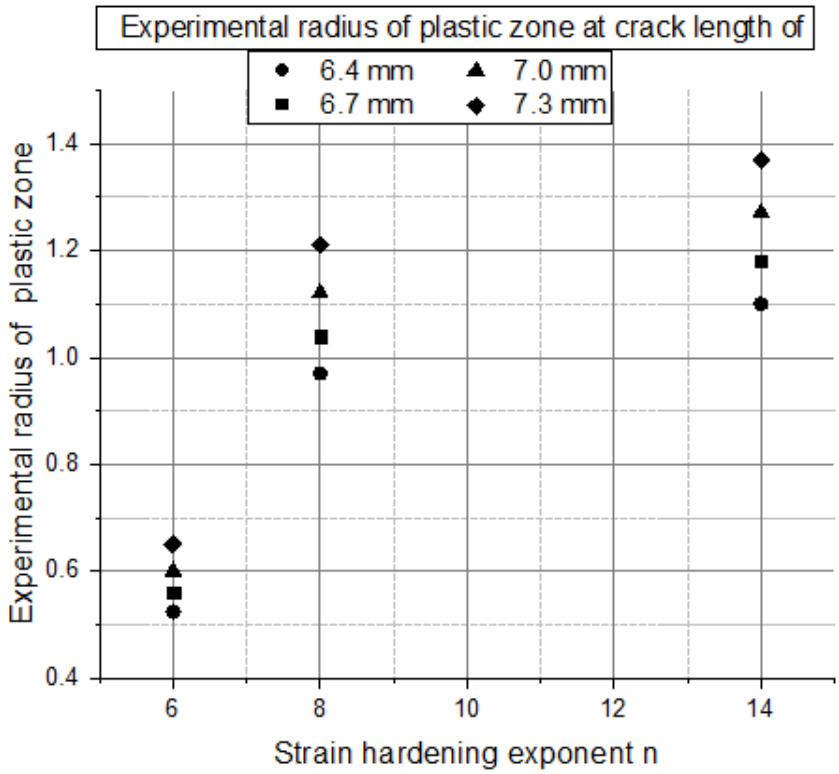

Fig 4.2: The experimental radius of plastic zone as a function of crack length for constant amplitude loading for value of strain hardening exponent n= 6, 8, 14

It is evident from the Fig 4.2 that at a higher value of strain hardening exponent (n=6), the radius of the plastic zone is smaller than for a lower value of strain hardening exponent (n=14) for the same crack length. Also, the size of plastic zone radius increases rapidly at the lower value of strain hardening exponent (n=14) than that at the higher n-value (n=6). It is apparent from the Figure that value of strain hardening exponent has a major influence on plastic zone size.

Fig 4.3 compares the theoretical and experimental stress intensity factor range as a function of crack length for constant amplitude loading at value of strain hardening exponent ranging from 6 to 14. The experimental stress intensity factor range was plotted with 95% confidence limits calculated using, [192]

$$(1+\mu-2s)K_S \leq K \leq (1+\mu+2s)K_S \qquad \textbf{[4.2]}$$

Where, μ and s are the mean and variance of the least square difference between the stress field equations and the experimental data and K_S is solution from the MPODM. The 95% confidence limits shown in Fig 4.3 are small suggesting that the accuracy of the data obtained from the TSA is high. For the constant amplitude case, the ΔK_I value was calculated from theory using a plane stress empirical formulation, [19]

$$\Delta K_I = \frac{\Delta P}{t\sqrt{W}} f\left(\frac{a}{W}\right) \qquad \textbf{[4.3]}$$

$$f\left(\frac{a}{W}\right) = \frac{\left(2+\frac{a}{W}\right)\left[0.886+4.64\left(\frac{a}{W}\right)-13.32\left(\frac{a}{W}\right)^2+14.72\left(\frac{a}{W}\right)^3-5.6\left(\frac{a}{W}\right)^4\right]}{\left(1-\frac{a}{W}\right)^{3/2}}$$

Where, ΔP is the load range, $a, W,$ and t are the crack length, specimen width and specimen thickness respectively.

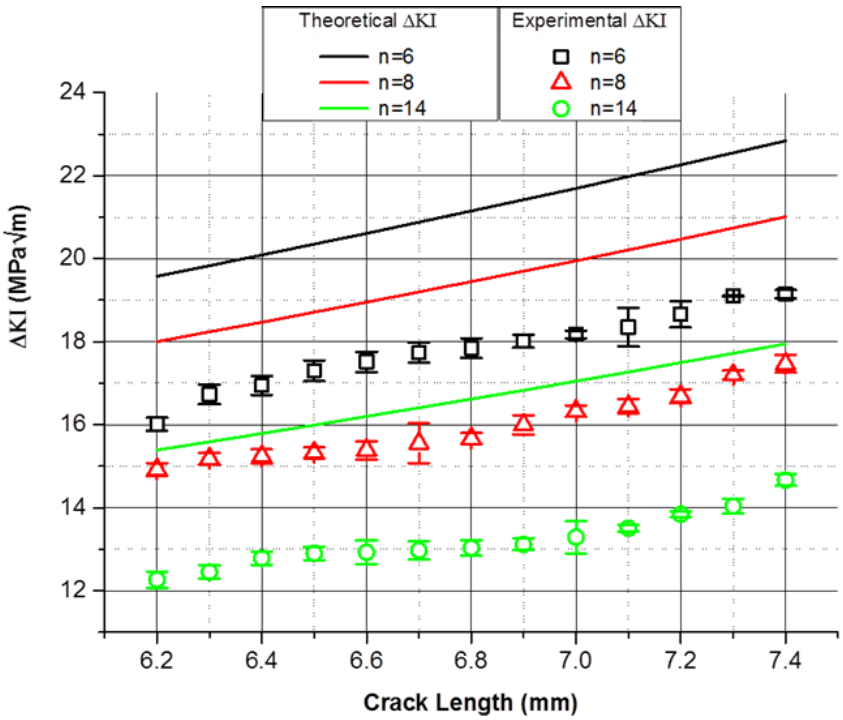

Fig 4.3: Comparison of experimental and theoretical stress intensity factor range as a function of crack length for constant amplitude loading for value of strain hardening exponent n= 6, 8, 14

It is apparent from Fig 4.3 that for constant amplitude loading, the experimental ΔK_I values are lower than those predicted from classical fracture mechanics theory suggesting the effect of closure in the experimental results. To justify this, it has been argued that plasticity at the crack tip and along the flanks shields the crack tip from the complete loading cycle which means it experiences only a part of the peak-to-peak stress amplitude resulting in a lower value of ΔK_I. The loss of adiabatic conditions demonstrated in TSA phase image (showing the difference measured between the temperature signal from the material and the forcing signal) confirms the presence of plasticity in the specimens (Figs 3.11 and 3.12). The effects of crack closure were not accounted for in the theory, so it is reasonable to attribute the difference between values for the amplitude of the stress intensity factor, ΔK_I obtained from TSA and theory to the presence of plastic shielding of the crack tip in a behaviour associated with crack closure. These observations agree the previous work of Patki et al., Tomlinson et al., Diaz et al. and Fulton et al. [113, 118, 119, 170]. Several experiments were performed at different load

ratios to identify the crack closure phenomena as shown in Fig 4.4. The crack closure effect is evident in the figure for all three load ratios (0.1, 0.33, and 0.5) where the values of experimental ΔK_I are less than the theoretical values of ΔK_I. Fig 4.4(a) suggests that at higher value of strain hardening exponent, the values of ΔK_I are higher. The same phenomena is observed in Fig 4.4(b) and (c) at load ratios 0.33 and 0.5 respectively. Fig 4.4(c) shows that there is little crack closure at load ratio of 0.5. To measure crack closure, it was tried to apply the strain gauge on the back of the CT specimen however due to finite dimension of the specimen, it was not possible to locate the strain gauge at desired location so the compliance method was not used. In the literature suggesting the crack closure levels, the material was different, and if the material is similar than the loading conditions and size of the specimen were different [113, 118, 119, 170].

(a)

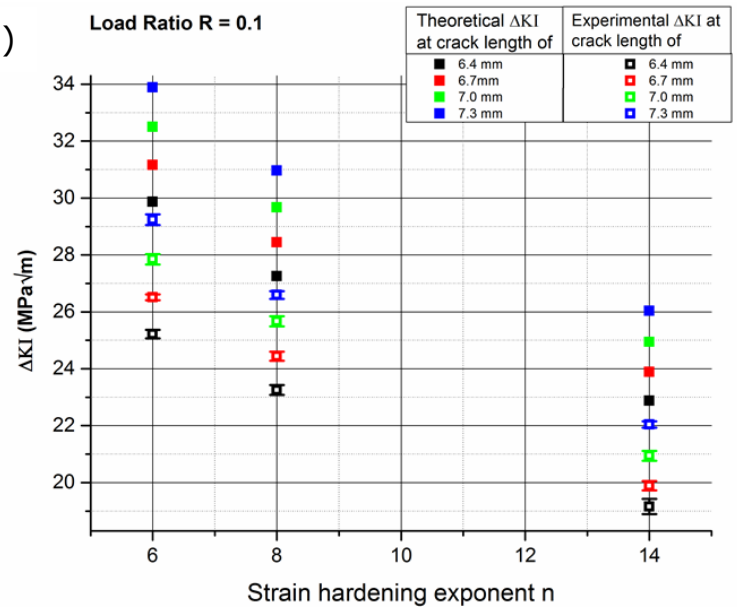
Load Ratio R = 0.1
Theoretical ΔKI at crack length of
6.4 mm
6.7mm
7.0 mm
7.3 mm
Experimental ΔKI at crack length of
6.4 mm
6.7 mm
7.0 mm
7.3 mm
ΔKI (MPa√m)
Strain hardening exponent n

(b)

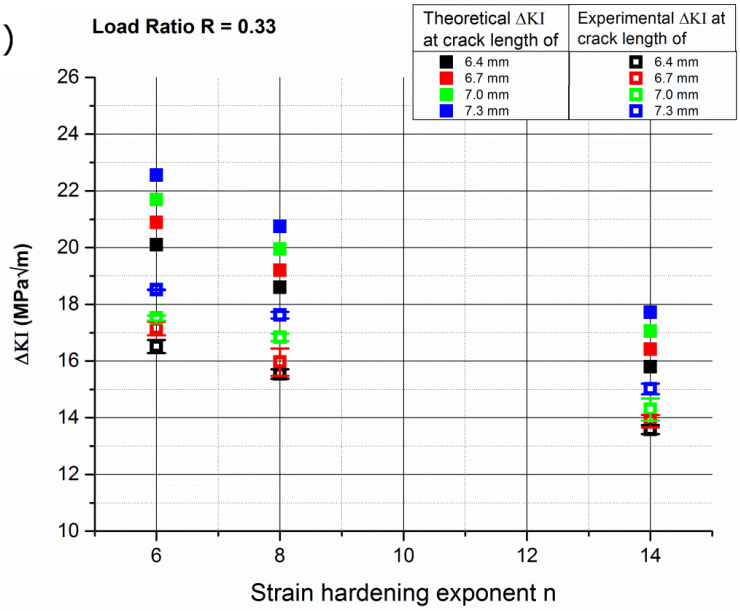
Load Ratio R = 0.33
Theoretical ΔKI at crack length of
6.4 mm
6.7 mm
7.0 mm
7.3 mm
Experimental ΔKI at crack length of
6.4 mm
6.7 mm
7.0 mm
7.3 mm
ΔKI (MPa√m)
Strain hardening exponent n

(c)

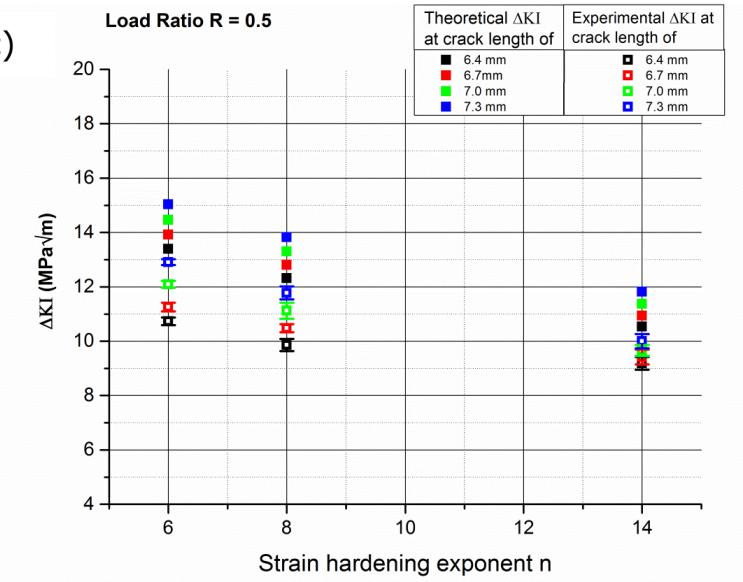
Load Ratio R = 0.5
Theoretical ΔKI at crack length of
6.4 mm
6.7mm
7.0 mm
7.3 mm
Experimental ΔKI at crack length of
6.4 mm
6.7 mm
7.0 mm
7.3 mm
ΔKI (MPa√m)
Strain hardening exponent n

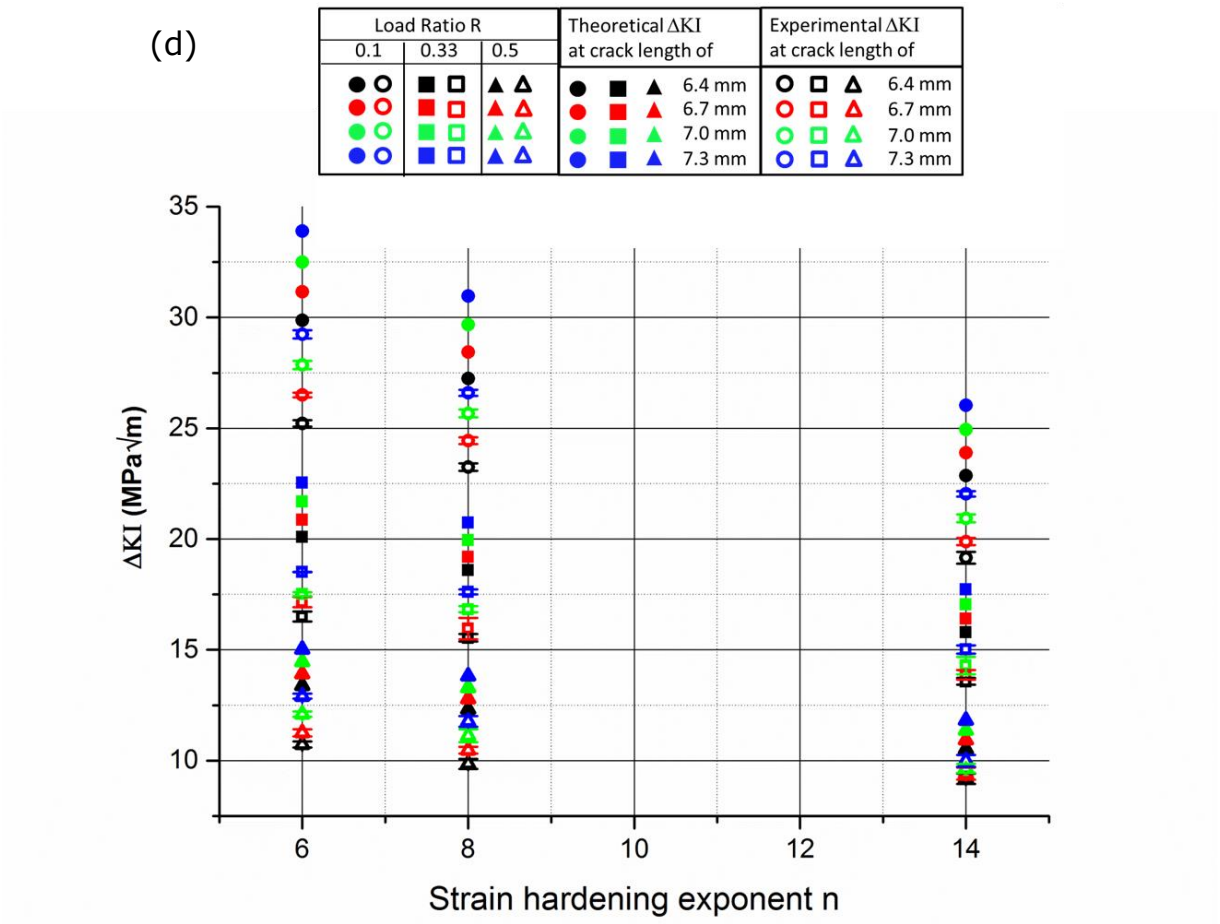

Fig 4.4: Comparison of experimental and theoretical stress intensity factor range as a function of crack length for constant amplitude loading for value of strain hardening exponent n= 6, 8 , 14 at (a) load ratio R=0.1 (Table 3-specimens 1, 2, 3) (b) load ratio R=0.33 (Table 3-specimens 4, 5, 6) (c) load ratio R= 0.5 (Table 3-specimens7, 8, 9) (d) combined data of (a), (b) and (c) for comparison (Table 3-specimens 1 to 9)

Fig 4.4(d) represents the values of experimental and theoretical ΔK_I together with the various load ratios at crack lengths of 6.4 mm, 6.7 mm, 7.0 mm and 7.3 mm over a range of strain hardening exponents. Fig 4.4(d) suggests that, as the load ratio increases, the value of ΔK_I from the TSA tends to approach the theoretical values of ΔK_I, showing a reduction in the closure level. The difference between the values of experimental and theoretical ΔK_I tend to decrease at lower value of strain hardening exponent at all load ratios suggesting a reduction in the level of crack closure at lower value of strain hardening exponent. It can be concluded that the value of strain hardening exponent has a notable influence on crack closure phenomena. The value of strain hardening exponent is related to plastic deformation of the material. When external load is applied, the dislocations move along slip planes. Dislocations interact with each other through their associated stress fields and dislocation movement is also prevented

due to the presence of barriers such as grain boundaries, sub grain boundaries, secondary phases of the material or the presence of other dislocations. This leads to pile ups of dislocations, which limit the further generation and movement of dislocations and ultimately the material fails. As a result of these dislocations, the stress required to deform the specimen increases. At a higher value of strain hardening exponent, more stress is required to deform this material resulting in the higher values of ΔK_I. ($K = \sigma_\infty \sqrt{\pi a}$) leading to significant crack closure. The current experiments prove that the value of strain hardening exponent significantly affects the crack closure phenomena.

The experimental data in Fig 4.5 was obtained from specimens 11, 12 and 13 listed in Table 3 to which the most aggressive overload of 50% was applied for 10 cycles at a crack length of 6.7 mm. It is possible to find out plastic zone area by straight forward evaluation of TSA images. To identify the effect of overload on plastic zone area, the area was also plotted alogwith the ΔK_I. Prior to the overload the values of ΔK_I was relatively stable. Upon application of the overload, ΔK_I rapidly decreased to a minimum value, and then increases gradually. It is important to notice that once the value of ΔK_I decreases, it did not increase with the same rate of decrease, but on the contrary increases slowly after some crack growth. It is suggested that, the first cycle of overload induces the enlarged plastic zone and this enlarged plastic zone shields any further enlargement of the crack tip plastic zone from the remaining overload cycles (9 cycles). It has been established that the crack closure is governed by the crack tip plasticity [207] and an increase in the crack tip plastic zone size due to the application of an overload would intensify the effect of plasticity-induced crack closure. As the crack grows into the compressive residual stress field formed by the overload cycle it encounters increased levels of plasticity. This increased residual wake of plastic deformation on the crack flanks causes the crack to shut at higher load. This results in a gradual increase in the value of ΔK_I. As the crack grows outside the zone of largest plastic deformation, ΔK_I gradually

approaches its pre-event value. It has been demonstrated that the largest residual compressive stresses occur in the immediate vicinity of the crack tip resulting in an instantaneous retardation [44] which is in accordance with the experimental observations in Fig 4.5. It has been concluded that the plasticity induced crack closure is the main mechanism causing retardation in all three materials.

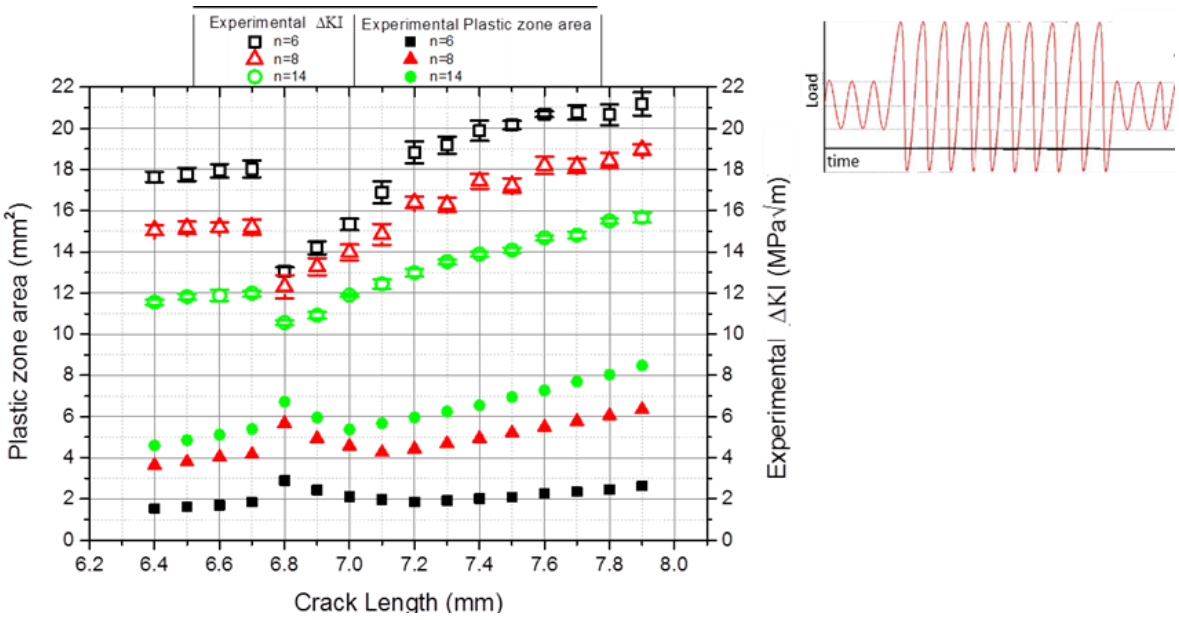

Fig 4.5: Plastic zone area and experimental stress intensity factor range as a function of crack length for 50% overload (specimen 10,11,12 from Table 3) for value of strain hardening exponent n= 6, 8, 14

Fig 4.6 shows the theoretical radius of plastic zone without overload along with the experimental measurement of plastic zone radius and area for the 50% overload case. The values from experiments for both radius and area of the plastic zone exhibit a large step when the overload is applied for all three value of strain hardening exponent. The values for both the radius and area return to the approximate pre-event values after some additional crack growth.

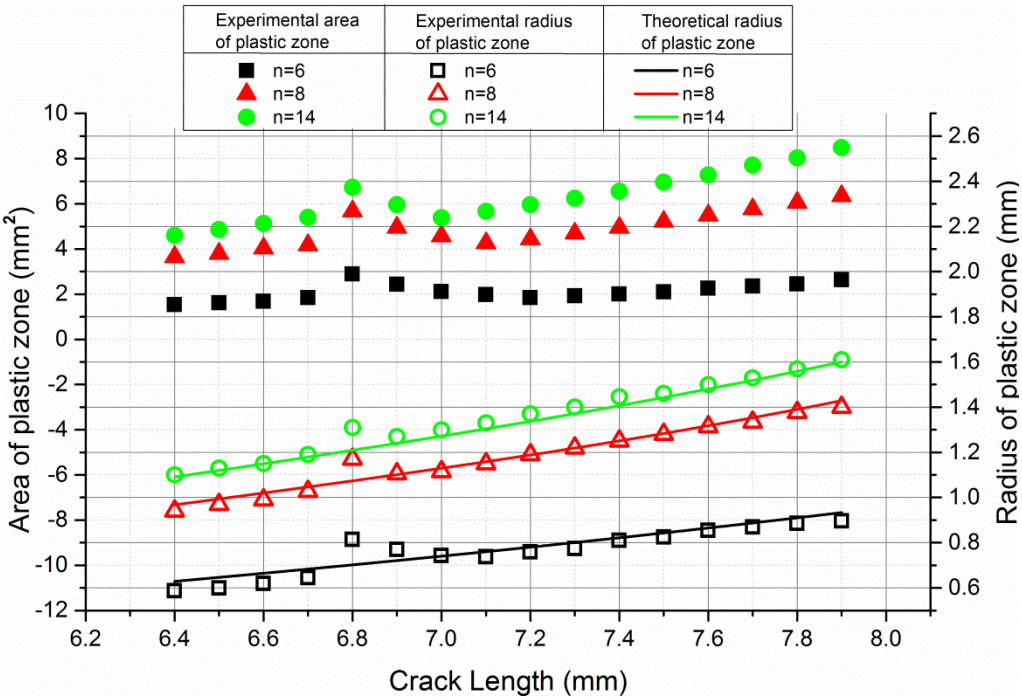

Fig 4.6: Plastic zone area and radius as a function of crack length for 50% overload (specimen 10,11,12 from Table 3) for value of strain hardening exponent n= 6, 8, 14

Fig 4.7 and Fig 4.8 reveal the effect of the value of strain hardening exponent on the stress intensity factor range ΔK_I after the application of 50% and 10% overloads respectively. The numbers 1 to 4 in Fig 4.7 indicate the crack length increasing from 6.6 mm to 7.3 mm indicating the crack length at normal crack growth, after the application of overload, within overload and after resuming the pre-event crack growth respectively. It is evident from the Fig 4.7 that at higher value of strain hardening exponent (n=6) the difference of ΔK_I between the point 4 and 2 is higher and it starts decreasing for lower value of strain hardening exponent. The similar trend is visible in Fig 4.8 but the difference of ΔK_I is less compared to 50% overload case (Fig 37). Fig 4.9 shows a comparison of the effect of % overload on the values of ΔK_I at various values of strain hardening exponent. It can be observed that ΔK_I decreases more rapidly after a 50% overload at n=6 than for n=14. There is significant reduction in ΔK_I after a 10% overload for higher value of strain hardening exponent however the reduction in ΔK_I at low value of strain hardening exponent is not substantial but still noticeable. Fig 4.7 to 4.9 support the conclusion that, at a higher value of strain hardening exponent (n=6), the

decrease in ΔK_I is more significant than that for the lower value of strain hardening exponent (n=14).

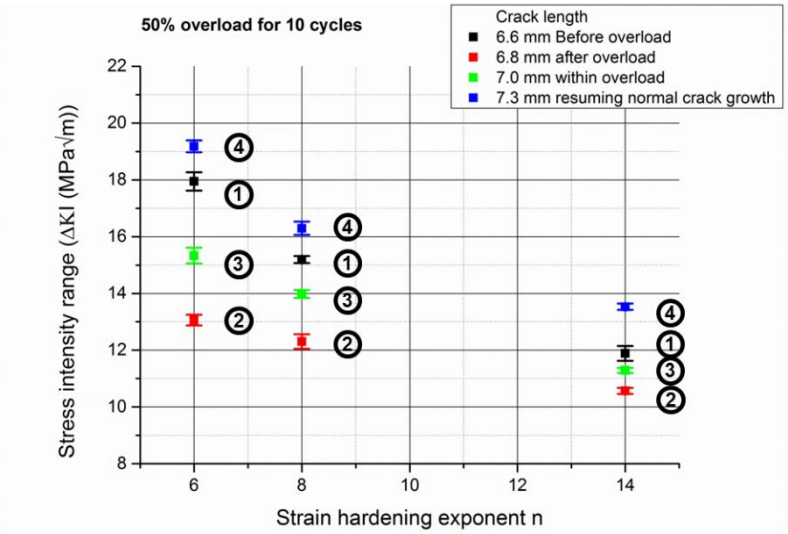

Fig 4.7: Stress intensity factor range ΔK_I as a function of crack length subjected to 50% overload (specimen 10, 11, 12 from Table 3) for value of strain hardening exponent 6, 8 and 14. Numbers 1 to 4 represents the crack length in ascending order

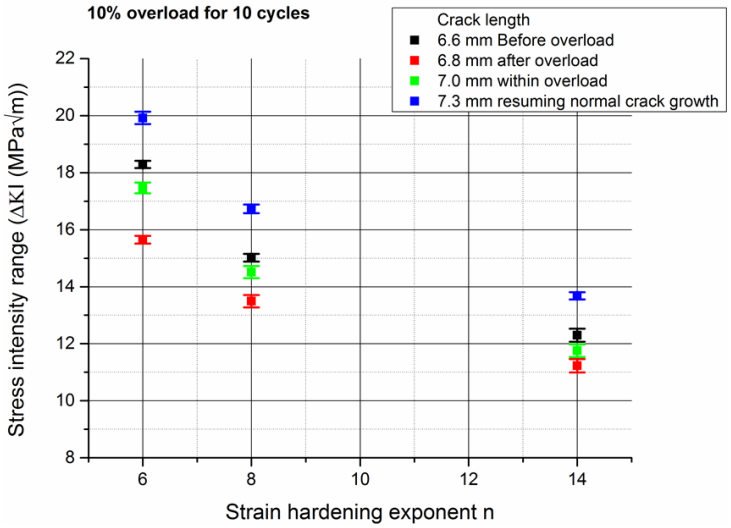

Fig 4.8: Stress intensity factor range ΔK_I as a function of crack length subjected to 10% overload (specimen 13, 14, 15 from Table 3) for value of strain hardening exponent 6, 8 and 14

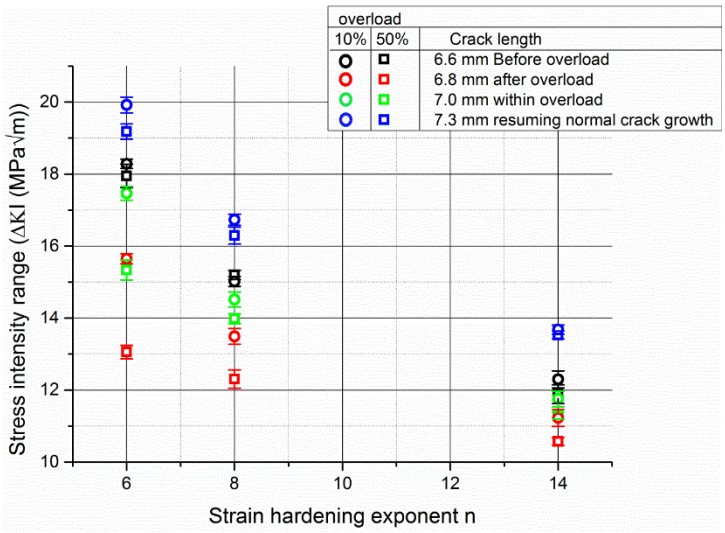

Fig 4.9: Stress intensity factor range ΔK_I as a function of crack length subjected to 50% and 10% overload (specimen 10 to 15 from Table 3) for value of strain hardening exponent 6, 8 and 14

Fig 4.10 displays % increase in plastic zone, % decrease in value of ΔK_I at different value of strain hardening exponent. Fig 4.10 indicates that after the application of a 10% overload, ΔK_I decreases by 17%, 10% and 8% while after 50% overload, ΔK_I decreases by 28%, 19% and 12% for value of strain hardening exponent of 6, 8 and 14 respectively. Also, the area of the plastic zone increases by 33%, 21% and 15% after the application of a 10% overload compared to 57%, 36% and 25% after application of a 50% overload at values of n of 6, 8 and 14 respectively. By comparison, the % decrease in the ΔK_I is almost half the % increase in the area of plastic zone for all value of strain hardening exponent. Fig 4.11 displays the crack growth retardation after the application of a 50% and 10% overload for various values of strain hardening exponent. It is evident from the figure that crack growth retardation is higher for higher value of strain hardening exponent at higher overload (50%). Fig 4.5 to 4.11 suggests that the decrease in the values of ΔK_I and increase in the size of plastic zone area and radius is proportinal to the % overload.

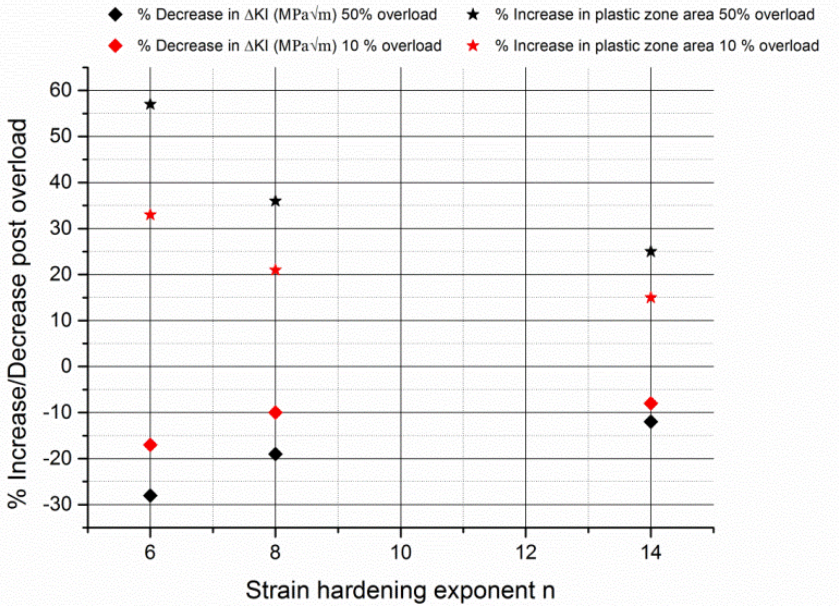

Fig 4.10: % increase in plastic zone area and % decrease in ΔK_I after application of 50% and 10% overloads at various values of strain hardening exponent (specimen 10 to 15 from Table 3)

Crack Growth retardation

Crack closure is known to cause crack growth retardation. Following an overload, a retardation process occurs as the crack propagates through the plastic zone produced by the overload. Fig 4.11 represents the crack growth curve for specimen 10. The curve has clearly visible three portions, crack growth- before, during and after overload. A straight line was fitted to the portion of the crack growth curve immediately prior to the application of the overload as shown in Fig 4.11 and a parallel line was fitted to the post-overload data in order to identify the cycle (≈11000) at which the crack growth rate returned to its pre-event value. The gap between these parallel lines indicated the period of crack retardation, which corresponds to about 0.4 mm of crack growth (≈2500 cycles). The crack growth retardation for all specimens in Fig 4.12 has been calculated in similar manner.

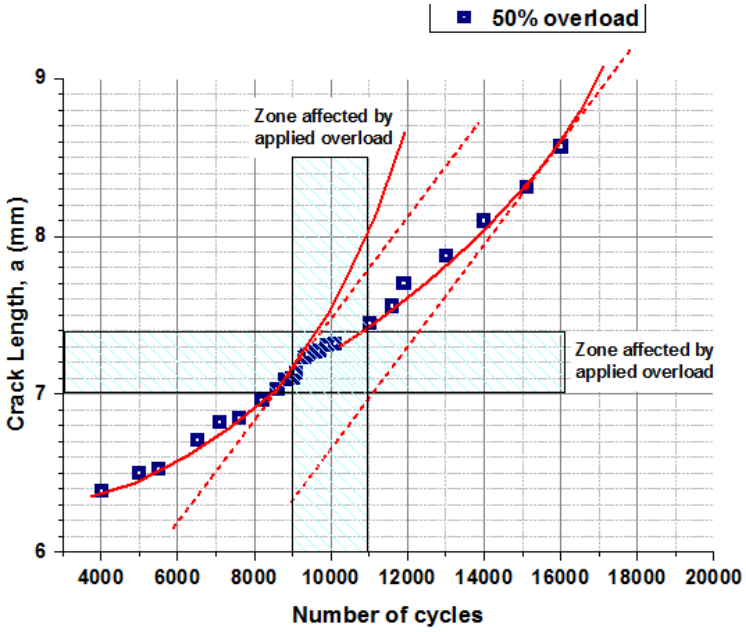

Fig 4.11: Crack growth curves for specimen 10 subjected to a 50% overload with data before and after the application of the overload fitted with trend lines to highlight crack growth retardation.

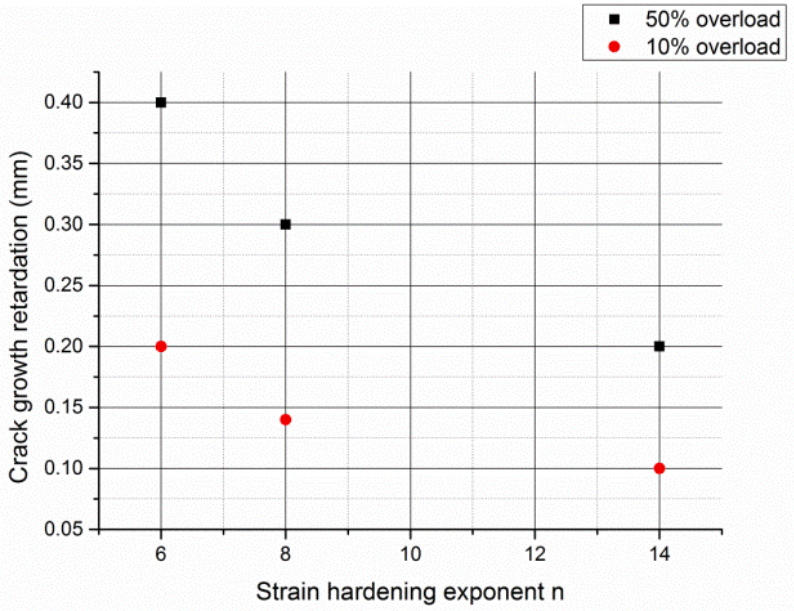

Fig 4.12: Crack growth retardation after the application of 50% and 10% overload for n= 6, 8 , 14 (specimen 10 to 15 from Table 3)

Fig 4.12 displays the crack growth retardation after the application of a 50% and 10% overload for various values of strain hardening exponent. It is evident from the figure that crack growth retardation is higher for higher value of strain hardening exponent at higher overload (50%). It can be concluded that the value of strain hardening exponent plays a major

role on size of the plastic zone, values of ΔK_I and crack growth retardation demonstrating that it is an important material parameter.

4.2 Backscattered Electron Image Analysis (BSEIA)

CT specimens of pure Titanium manufactured based to BS-ISO 12108:2012 standard as shown in Fig 3.3 were employed for the fatigue experiments. One side of a specimen was prepared metallographically i.e. by grinding, polishing and electropolishing to observe under the SEM while on the other side thin black matt paint was applied in order to record data for TSA experiments. The specimens were loaded in a uniaxial INSTRON ELECTROPULSE-E3000 loading frame with a mean load of 526 N at 0.33 load ratio at a frequency of 20 Hz. The crack was initiated from the notch and TSA data were collected after the crack growth of 3.0 mm on one side of the specimen followed by observation in the SEM and BSE image capturing on the other side after completion of each experiment. Four different specimens were tested using the parameters provided in Table 4.

Table 4: Fatigue test parameters and numbers of BSE images captured to charecterise the plastic zone at various locationa of crack growth

Specimen	Overload (% of amplitude)	crack length at which experiment ended to collect BSE images	Location of BSE images captured	Number of BSE images captured
CT1	No	6.6 mm	Before overload	13 x 13
CT2	50%	6.8 mm	At overload	13 x 15
CT3	50%	7.0 mm	Within overload	13 x 15
CT4	50%	7.2 mm	Beyond overload when crack growth rate returned to pre-event value	13 x 15

The TSA observation of plastic zone of the fatigue cracks were at the macro scale, while BSEIA technique was employed to observe the same zone at the micro scale. Yang et al. applied this technique to identify a plastic strain map for a fatigue crack of length of 5.88 mm subject to constant amplitude loading in 2011 [144]. In the current project, the same idea has carried forward to analyse the plastic zone of a fatigue cracks subjected to overload. To capture the BSE images for a particular crack length, the specimen needs to be unloaded, if the same specimen is loaded again, the crack path, crack growth, stress intensity factors and residual plasticity will not be same as a specimen which was constantly loaded without interruption. So, four identical specimens were prepared. For the first to fourth specimen, the experiment was stopped at crack lengths of 6.6 mm (before overload), 6.8 mm (after application of overload), 7.0 mm (within the overload), 7.2 mm (beyond the overload effect is vanished and crack growth resumed its predicted path) respectively. After the fatigue loading all 4 specimens were observed in the FE-SEM to capture the BSE images. Fig 4.13 shows the schematic of array of images of 115 x 115 μm around the crack tip consisting of 15 x 13 (195 in total) images at a centre to centre distance of 171 μm.

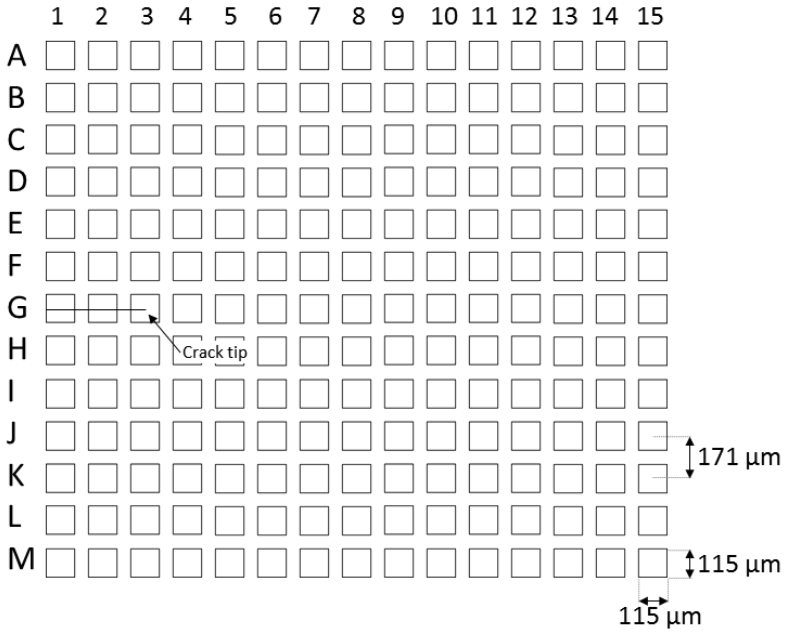

Fig 4.13: A schematic of the array of images around the crack tip. Each square is 115 x 115 μm with a centre-to-centre sacing of 171 μm

Fig 4.14 shows the upper half of the array of BSE images surrounding the fatigue crack in specimen CT2. The BSE images were collected at an instrument magnification of 500x (equivalent to 3 pixels per μm) using a Jeol FE-SEM 7001 scanning electron microscope (Plymouth University, UK) so that each image was 115 × 115 μm with a centre-to-centre distance of 171 μm. Figure 4.14 reveals a gradual change in the sharpness of the BSE images with distance from the crack tip. At large distances from the crack tip, e.g. at position 15A-15G in figure 4.14, the images display sharp, well-defined features, allowing easy identification of the individual grains, which tend to exhibit uniform brightness levels that are distinctly different to their neighbours. Images acquired closer to the crack tip show a significant variation in brightness within the grains, making the individual grains less apparent and the overall image less sharp. This is a result of significant crystal rotations and residual plastic strain within these grain patches. Grain boundary edges, slip lines and secondary grain boundary cracks are visible in the grains close to the fatigue crack as shown in Fig 4.15 A specially written MATLAB program was employed to find FWHM of all the images as mentioned in previous section. In order to quantify the changes in image characteristics, a calibration curve from Fig 3.20 was used to estimate the % strain of the BSE images.

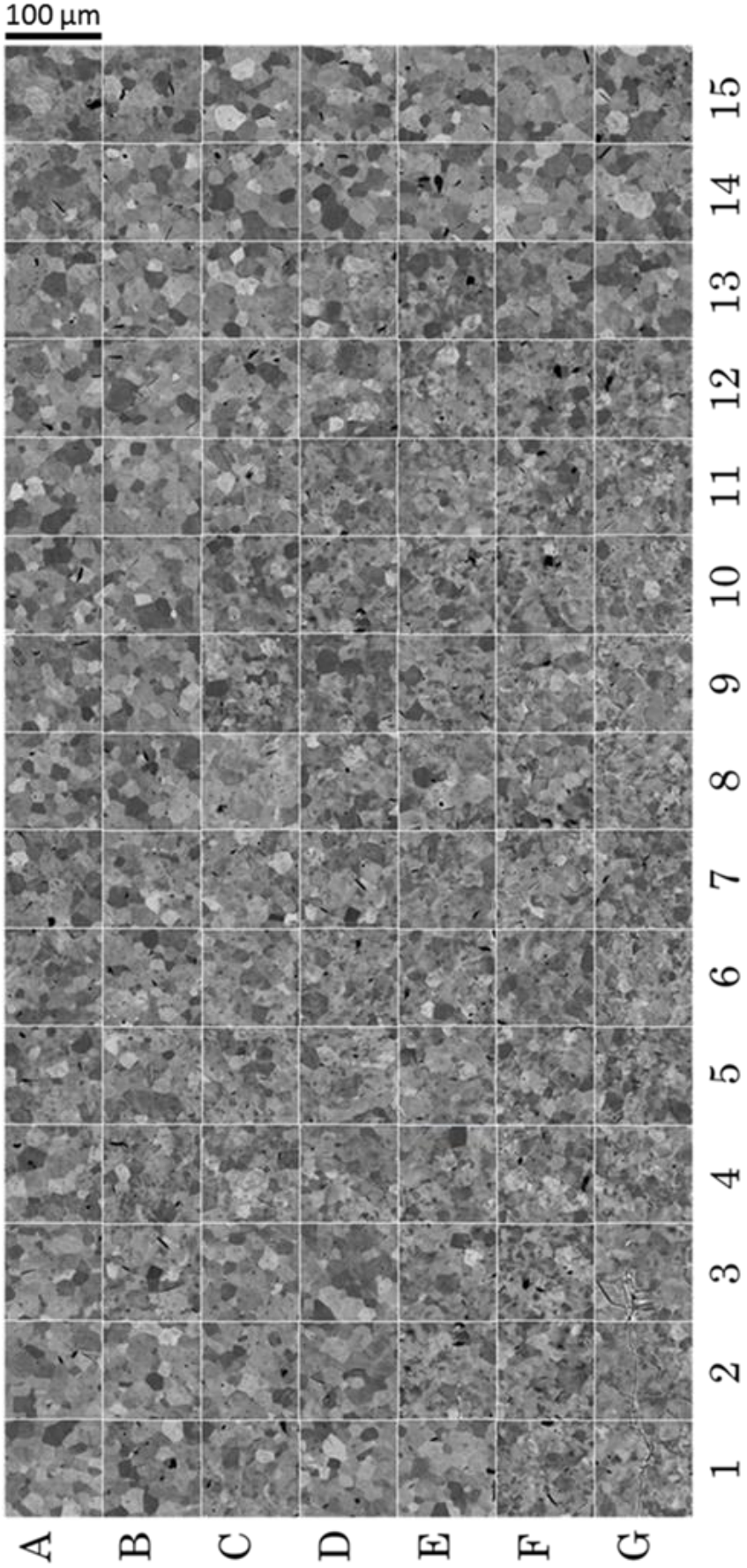

Fig 4.14: Upper half of the array of BSE images surrounding the crack tip at a centre-to-centre distance of 171 µm. Images surrounding the crack tip region shows more lattice distortion indicating higher residual plastic deformation

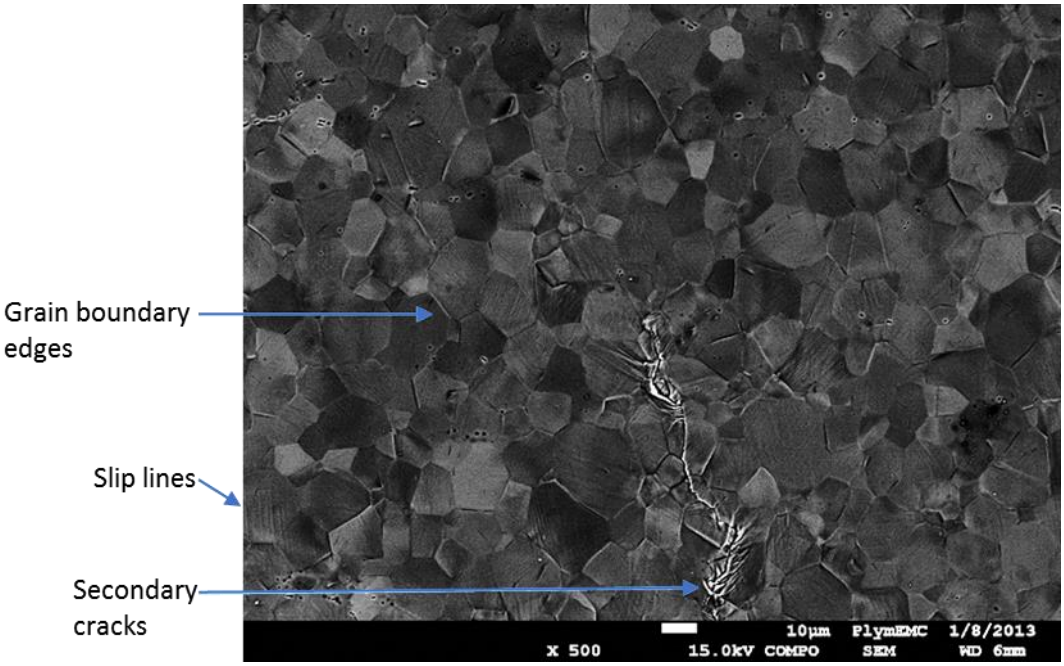

Fig 4.15: Clearly visible grain boundaries, secondary cracks and slip lines on BSE image

The results shown in Fig 4.16 are the map of residual plastic strain in which each coloured tile represents an average residual plastic strain. Fig 4.16(a), shows an area of high strain extending about 1.1 mm ahead of the crack and about 0.7 mm on both sides of the crack. It is important to note that there were 13 x 13 BSE images collected for specimen CT1(Fig 4.16(a)) but to compare it with rest of the specimens, additional columns were inserted (line 14 and 15) as shown by the black colour (not BSE images). The plastic strain in Fig 4.16 (a-d) exhibits a value of around 20% in the crack wake and at the crack tip, which decreases dramatically with distance from the crack tip. Fig 4.16 clearly reveals the decay in the local plastic strain distribution with distance from the crack tip, which is to be expected from traditional fracture mechanics models. In addition, significant scatter is seen in the strain levels within this decaying plastic zone. This scatter is because of the material heterogeneity that arises from the inter-granular variations in material morphology. Some scatter may arise from measurement uncertainties such as, change in brightness, contrast, magnification etc. but they are negligible. The plastic zone size estimated using TSA experiment has been superimposed on each map as a white line. The comparison of the crack tip plastic zones determined from the

TSA and BSEIA shows good agreement. The plastic zone size found using the BSEIA technique is sensitive to the percentage overload as can be seen in Fig 4.16(b). Immediately after a 50% overload for 10 cycles the plastic zone area calculated from BSEIA increased by 60% at crack length of 6.8 mm compared to crack length of 6.6 mm. (calculated by counting the number of patches having higher than 6% plastic strain) while the plastic zone area found from TSA data exhibits an increase of 57% which shows an excellent agreement between the techniques. It is known that the minimum plastic strain in a plastic zone is much smaller than 6% (especially at the border between plastic zone and elastically deformed material). In the current technique, various BSE images were plotted which are not overlapping so it is difficult to exactly evaluate the boundary. Most of the BSE images shows some extent of deformation and hence the strain. Observation of all four plastic strain maps shows a sudden change in plasticity from 6% to 0-2% in the array of the BSE images. This sudden change in plasticity values were taken in to consideration to determine the plastic zone size. This observation is consistence with Yang et al.'s plastic strain map where the plastic zone size is confined to the region where plasticity changes suddenly from high to low value [144]. The observation of strain map reveals that, far from the crack, the BSE images shows around 2% deformation which raises around 6% in the next image as we move from right to left in opposite direction to crack growth, e.g. Fig 4.16 (a) image 10D-10K and 11D-11K, Fig 4.16(b) 13B-13J and 14B-14J etc. So to determine the area of the plastic zone the images with higher than 6% plastic strain were selected. It can be observed from Fig 4.16(c) that after the application of an overload the area of the plastic zone starts decreasing until it reaches the pre-event value predicted by theory.

The plastic zone found from the TSA data is smaller than that determined from the BSEIA technique, but of the same order of magnitude with its boundary in the direction perpendicular to crack growth corresponding to 6-8% plastic strain measured from the BSE

images. Ahead of the crack, the boundary of the plastic zone found from the TSA data corresponds to 8-9% plastic strain evaluated from the BSE images.

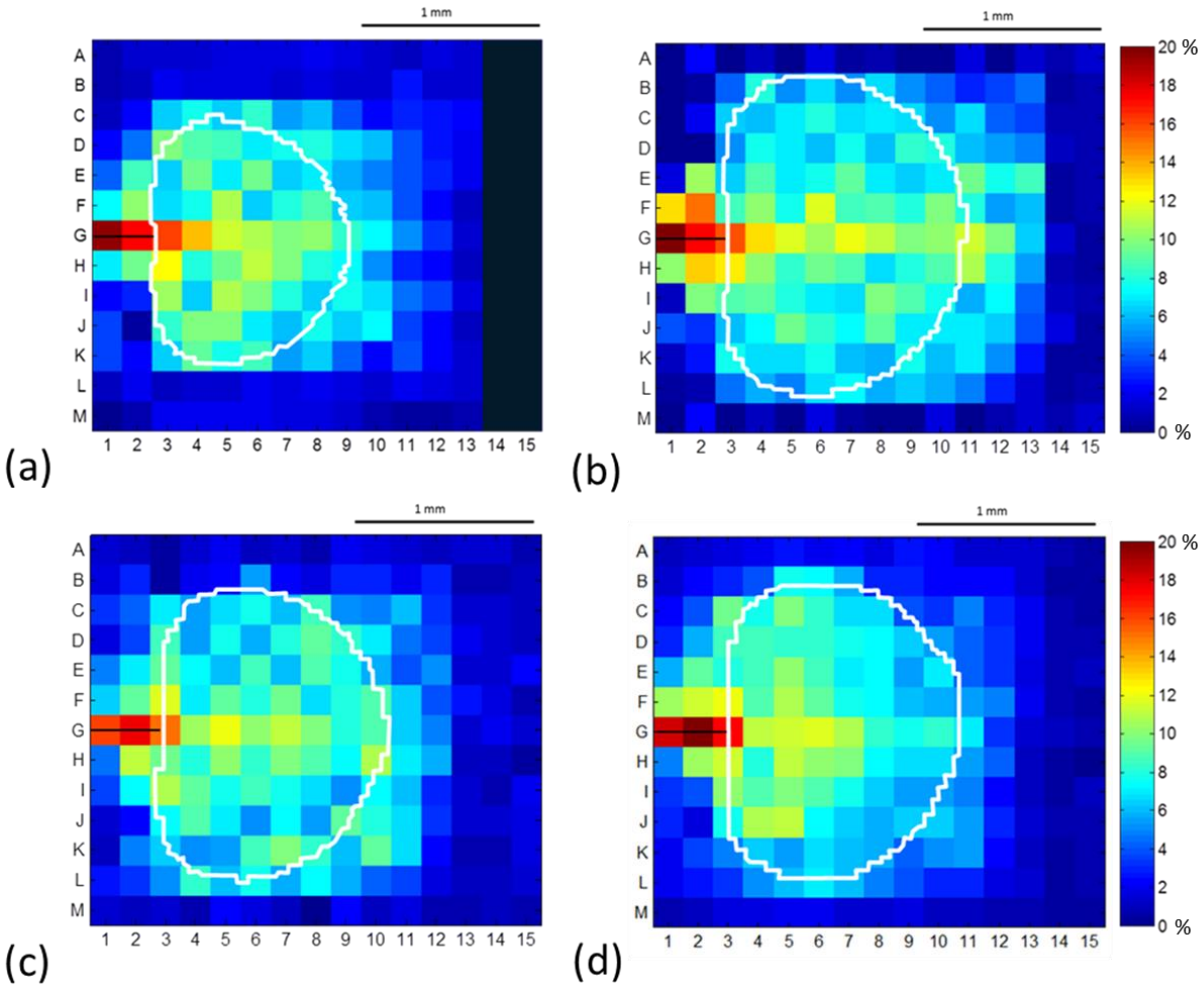

Fig 4.16: Plastic strain map surrounding the fatigue crack tip together with the thermoelastic stress analysis (white line) at crack lengths of (a) 6.6 mm - before applying overload (b) 6.8 mm - after application of overload (c) 7.0 mm - within the region where overload effect is prevailed (d) 7.2 mm – overload effect is vanished where plastic zone resumed pre-event crack growth predicted from theory. The colour bar represents the residual plastic strain in %

There is a difference in results from both the techniques as both experimental techniques are based on different physical principles. The TSA data is based on identifying the region, in which the generation of heat by dislocation movement is sufficiently large to cause adiabatic conditions to be lost, i.e. a heat transfer occurs during fatigue loading. A higher density of dislocations will generate a larger heat transfer, which was detected as a phase difference. The data from the BSE images are based on detecting the disruption of the grains by the residual dislocations resulting from plastic deformation which will not disappear when

the load is removed however; the removal of the load causes some reverse plasticity as a consequence of compatibility requirements between the crack tip plastic zone and the surrounding elastic region. This reverse plasticity influences the measurement of the plastic strain in the region closest to the crack tip but would not affect the maximum extent of plasticity detected as can be observed in Fig 4.16. Further exploration of Fig 4.16(a-d) suggests that the plastic zone boundaries achieved using BSE images are mostly symmetrical in the direction perpendicular to the crack length i.e. the plastic zone extent in BSE images 1to15A-G is same as the 1to15G-M. The % strain is surely different in all the images but the extent of plasticity is same on both the sides perpendicular to the crack length. So, it was proposed to capture only one half of the BSE images (either 1to15A-G or 1to15G-M) instead of capturing entire batch of BSE images surrounding the crack tip. This would reduce considerable labour, time and microscope usage expenditure for future studies. In the current study, two days were required to capture BSE images for one specimen so in total eight days for four specimens that could be shortened to only four days if the suggestion of capturing only half of the BSE images implemented.

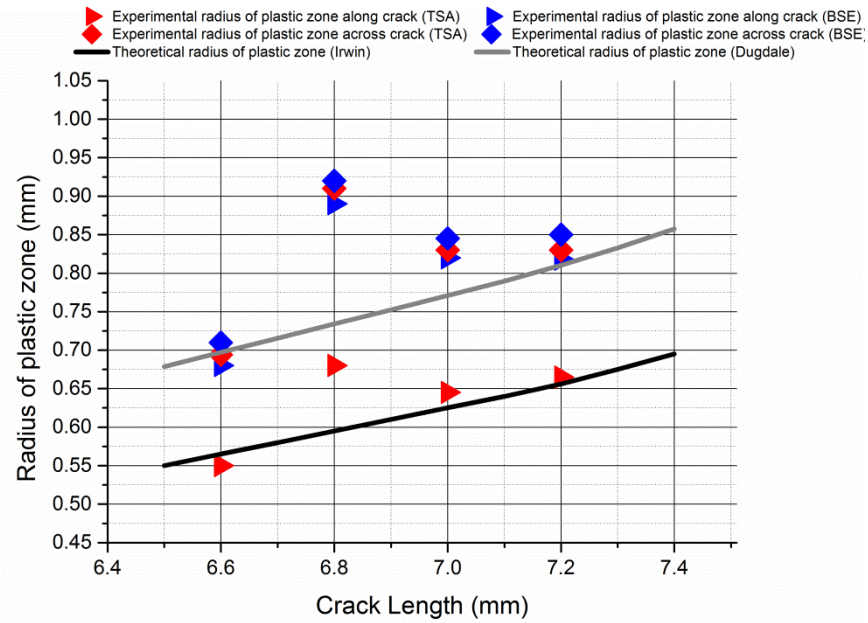

Fig 4.17: Comparison of theoretical radius of plastic zone along the crack length obtained using Irwin and Dugdale criteria together with the experimental radius of plastic zone along and across the crack length obtained from TSA and BSEIA techniques

Fig 4.17 compares the theoretical (according to Irwin and Dugdale approach) plastic zone radius with the experimental plastic zone radius obtained from TSA and BSEIA techniques for 4 specimens defined in Table 4. It is evident from the Fig 4.17 that the value of the experimental radius of the plastic zone perpendicular to the crack growth found from the TSA data is in between the values of plastic zone perpendicular and parallel to the crack growth found using the BSEIA technique. All three values are nearly similar and exhibit very good agreement with the theoretical radius of plastic zone calculated using Dugdale's approach. Fig 4.17 reveals that there is an excellent agreement between the extent of the plastic zone parallel to the crack growth direction found using TSA measurements and the value estimated using Irwin's approach and excellent agreement between the size of the plastic zone perpendicular to the direction of crack growth found using the TSA technique and the value estimated using Dugdale's approach. Although this level of agreement is encouraging, it should be noted that theoretical expressions are based on the continuum principles of linear elastic fracture mechanics, which take no account of dislocation distribution or movement, or how these will be affected by local grain structure and orientation variations. In short, the presence of plasticity is not accounted for in theory so the difference between the experimental and theoretical plastic zone radius are reasonable.

It was assumed that the DFT calibration associated with tensile test would be similar to the fatigue test i.e. irrespective of two strain paths. In the present work two strain paths are considerably different, i.e., a uniaxial strain distribution with measurements taken during monotonic loading compared to a tri-axial strain distribution at the crack tip induced by high-cycle fatigue with measurements taken after loading. Previous studies [212, 213] indicate that fatigue specimens can be expected to have a higher dislocation density for an equivalent strain

level than uniaxial tension specimens. Thus, the strain deduced for the fatigue sample based on the calibration using the uniaxial sample, might be an over-estimate of the actual strain to some small extent. The data from the BSE images is based on detecting the disruption of the grains by the geometrically necessary dislocations required for plastic deformation. This disruption will not disappear when the load is removed, as was necessary for the observations in the SEM; however, the removal of the load could have caused some reverse plasticity because of compatibility requirements between the crack tip plastic zone and the surrounding elastic region. This reverse plasticity could have influenced the measurement of the plastic strain in the region closest to the crack tip but would not affect the maximum extent of plasticity detected.

Crack tip plasticity has been established as a cause of crack closure and an increase in the crack tip plastic zone size due to the application of an overload would intensify the effect of plasticity-induced shielding of the crack tip and crack closure as can be observed in Fig 4.16 (b) and (c). The BSEIA technique shows the sensitivity to the overload and hence has a great potential in identifying the role of crack tip plastic zone in crack closure and plasticity-induced shielding.

4.2.1 Application of BSEIA technique to other materials

The BSEIA study was expanded to use the technique for the Al 2024-T3 and Al 6061-T6 materials used in present research. The mechanical polishing and electropolishing techniques were developed suitable to both the materials.

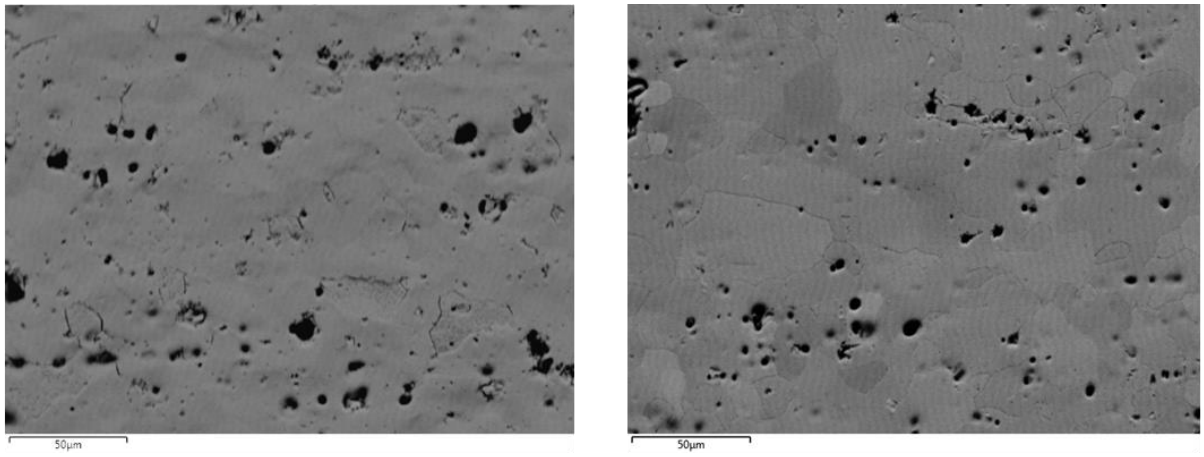

Fig 4.18: BSE images of Al 2024-T3 and Al 6061-T6 at x500 magnification

Fig 4.18 shows BSE images from Al2024-T3 and Al 6061-T6, in which grain boundaries are not visible. One of the reason could be the atomic number and it also depends on the settings of the SEM (e.g. the voltage). In general, the BSE signals can be obtained from 2 distinct phenomena: (1) atomic number contrast, in which the composition determines the image contrast, and (2) orientation contrast, in which the crystal structure of the material determines image contrast. There is also Electron Channelling Patterns, which are unique to a particular crystal orientation, but their usage is more complicated and is not be relevant to the current research. To obtain better images, various settings on SEM were tried such as working distance, current, voltage, contrast and brightness. The production efficiency for backscattered electrons is proportional to the material's atomic number, which results in the image contrast being a function of composition. The atomic number of Aluminium (13) is lower than the Titanium (22). As a result, the BSE detector is not able to generate visible contrast to identify clear grain boundaries. Al 2024-T3 and Al 6061-T6 are alloyed with Cu, Mn, Cr and Zn (additionally Al 2024-T3 has Ni) whose atomic number is higher so a few grain boundaries are faintly visible where these alloys are located. The observation of BSE images from Fig 4.17 also revealed that there was large number of black spots on both the images which resembled holes in the metal.

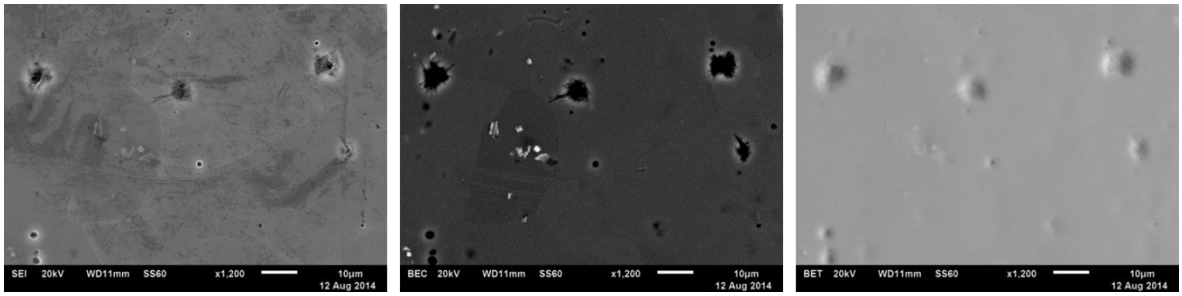

Fig 4.19: SEM images at same location of specimen captured using various detectors

To analyse it further, three images from different detectors namely Secondary Electron Images (SEI), Backscattered Electron Contrast (BEC) and Backscattered Electron Topography (BET) images were captured at the same location as shown in Fig 4.19. The BET image revealed that the black spots are etch pits introduced due to electropolishing of the specimen. To confirm the same, another technique called Energy Dispersive X-ray Spectroscopy (EDS or EDX) was used for elemental analysis of the sample as shown in Fig 4.20. A peak of Mg was detected in the elemental analysis on all three etch pits confirming the presence of the metal.

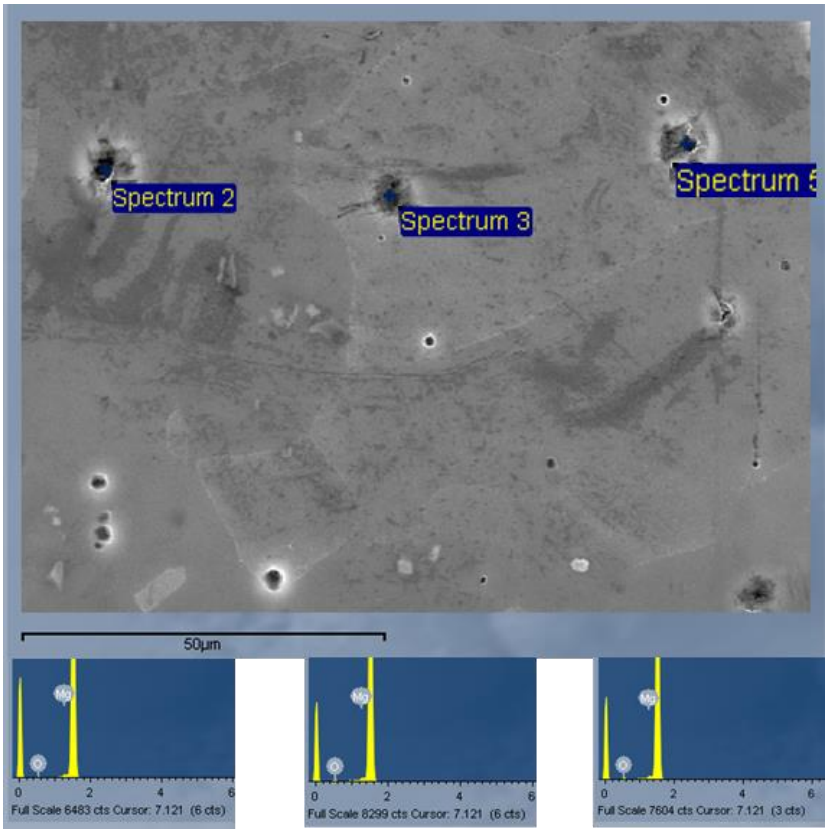

Fig 4.20: Energy dispersive X-ray spectroscopy (EDS/EDX) results revealed the presence of Mg on black spots

The etch pits are generated due to removal of precipitates and dislocations during electropolishing of specimen which can be explained by using Fig 4.21. Electropolishing removes a thin layer of material from the surface by means of anodic dissolution that will remove impurities, particles, structural defects etc. However, depending on the size of defects or the precipitates electropolishing may introduce well developed etch pits at the intersection points of dislocations, at the intersection line of grain boundaries and stacking faults with the surface as shown in Fig 4.20. The locations from where the precipitates have been removed are visible as shallow pits with varying size, depending on the size of the precipitate.

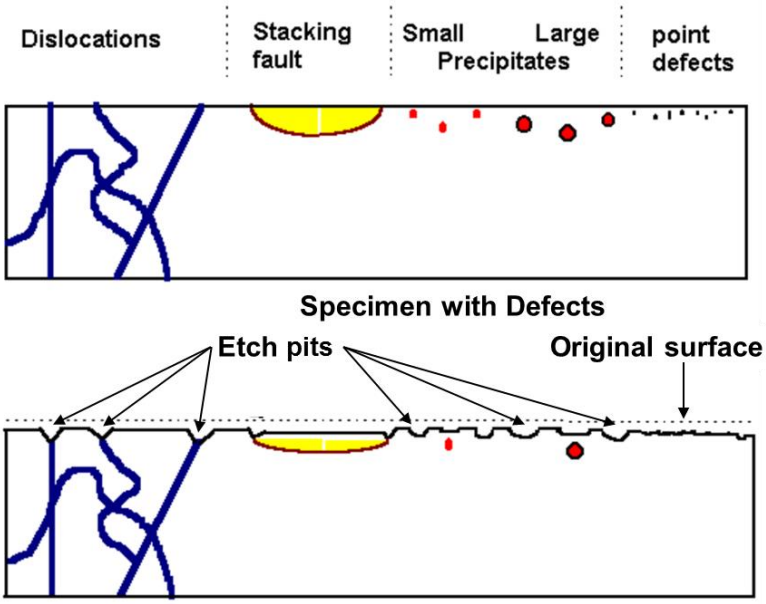

Fig 4.21: A schematic of specimen surface showing various defects before electropolishing (top image) and after electropolishing (bottom image) [208]

A similar phenomenon might have prevailed during the electropolishing of Al 2024-T3 and Al 6061-T6 resulting in etch pits. The Aluminium alloys do not reveal clear grain boundaries so it is not possible to find a distinct profile after applying the DFT to BSE images which results in very similar FWHM for all the images. Also, the etch pits will contribute to the profile of the DFT of the BSE images give artificially higher FWHM so it was decided to change the parameters of electropolishing such as voltage and time. When the time of electropolishing was increased, the specimen showed a distinct colour of electrolytes on surface

probably due to over-electropolishing and there was no significant decrease in etch pits. The change in voltage resulted in decreased number of etch pits but they were present in all images. The BSE images without etch pits were not achieved. Considering the restricted time and resources this technique was left for future investigation.

4.2.2 Recognition of plasticity from backscattered electron images using texture features

BSE images have useful information embedded in at the micro scale. The image processing and pattern recognition tools are very effective to analyse these images and offer great potential. In the previous section the plastic strain map was constructed by finding the FWHM of the DFT of BSE images. Yang et al. characterised residual plasticity using the features of the Fourier transform of Back-Scattered Electron (BSE) images on commercially pure Titanium Compact Tension (CT) specimen [144]. The same BSE images from Yang et al. were processed further to analyse the crack tip plasticity using the statistical information of BSE images. Fig 4.22(a) represents the results obtained by Yang et al. The top- image represents the calibration curve at six loading increments between 0% and 22% engineering strain levels from an in-situ tensile test [144]. For each strain level, six BSE images were acquired in a rectangular array in the middle of the specimen resulting 36 images in total. The bottom image represents the plastic strain map around the crack tip together with the TSA data (white line) and estimates of plastic zone size based on approaches of Dugdale (green line) and Irwin (blue line) criteria plotted by Yang et al [144].

In addition to Yang's approach, a number of image analysis techniques have been employed for quantifying plastic deformation in metals based on BSE images. It is found that some texture features correlate well with the level of plastic strain. In particular, statistical information of image, such as (a) standard deviation of the image and (b) histogram of the image,

Standard deviation is the measure to quantify the amount of variation or scatter in a set of data. A low standard deviation indicates that the data points tend to be close to the average of the set, while high standard deviation indicates that the data points are spread out over a wider range of values. The grains in BSE images within the elastic region shows even brightness and contrast and so the value of standard deviation of these BSE images are low representing that the each individual grain has values close to the average value of entire set of data. On contrary, within the plastic region, the accumulation of dislocations, distorted grain boundaries and significant local crystal rotations results in a remarkable variation in brightness and contrast. These lead to a high value of standard deviation in the BSE image. To confirm the same, the value of standard deviation of all BSE images were found using the MATLAB 'std(2)' function. Where standard deviation,

$$\boldsymbol{s = \left(\frac{1}{m-1}\sum_{i=1}^{n}(x_i - \overline{x})^2\right)^{1/2}} \qquad \textbf{[4.4]}$$

$$\boldsymbol{\overline{x} = \frac{1}{m}\sum_{i=1}^{n} x_i}$$

where, $\boldsymbol{s}$ is the standard deviation of data vector $\boldsymbol{X}$ and $\boldsymbol{m}$ is the number of elements in the data set. Fig 4.22(b) shows the calibration curve (top image) and the plastic strain map (bottom image) surrounding the fatigue crack plotted by finding the standard deviation of BSE images.

Histogram of the image calculates the pixel intensity values of the image. The histogram is a graph showing the number of pixels in an image at each different intensity value. The values of histogram would be different for the images within the plastic and elastic region due to the aforementioned reasons. Fig 4.22(c) shows the calibration curve (left image) and the plastic strain map (right image) surrounding the fatigue crack plotted by finding the maximum histogram number of BSE images.

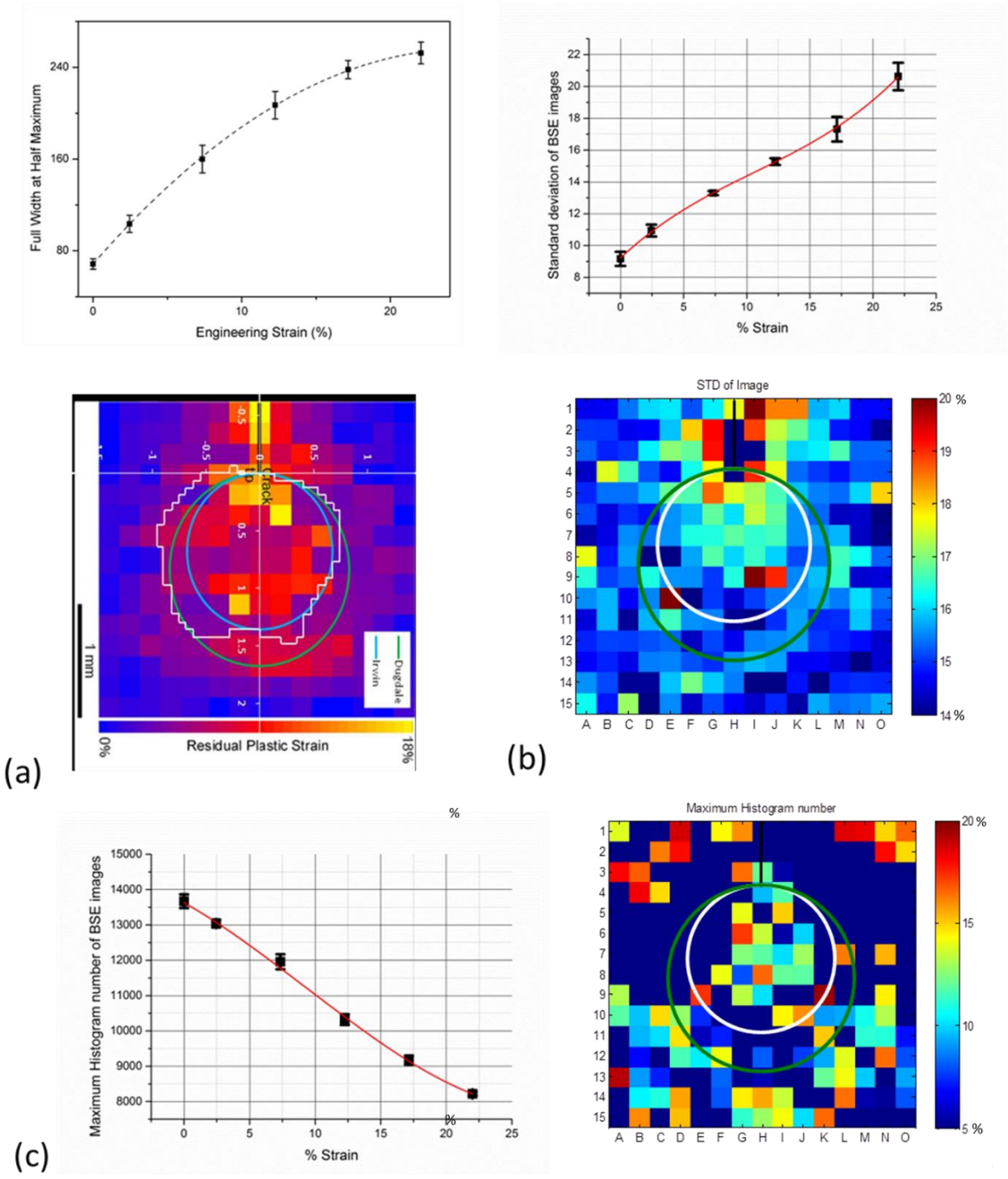

Fig 4.22: Calibration curve and relevant Plastic strain map surrounding the fatigue crack tip together with the radius of plastic zone found using Irwin (white line) and Dugdale (green line) approach (a) found using FWHM of DFT of BSE image [144] (b) found using standard deviation of BSE images (c) found using maximum histogram number of BSE images

It is apparent from the calibration curves (Fig 4.22(b) top image and 4.22(c) left image) that the values of standard deviation and histogram are sensitive to strain increment. However, the amount of sensitivity is not enough to identify the plastic zone in the array of BSE images surrounding the fatigue crack tip. For example, Fig 4.22(b) suggests that the regions

surrounding the crack has higher plastic strain yet the colormap scale indicates that the most of the images from the array are plastically deformed and have higher than 14% strain which is not supported by previous research by Yang et al. Fig 4.22(c) suggests that, the plastic strain ahead of the crack in 10-13H BSE images is less than 5% suggesting the elastic plastic boundary however the next two BSE images-14-15H have higher than 15% plasticity which is not consistent with previous research. Comparison of all three Figures of 4.22(a) to (c) indicates that there is disagreement between the radius of plastic zone obtained by image analysis technique and previous research by Yang et al. [144]. So it was concluded that the texture descriptors are not suitable to characterise the plastic zone. However, there are other texture features techniques such as image entropy analysis and edge detection algorithms should be explored further in order to quantify the elastic-plastic boundary. The evaluation of BSE images using texture features is very simplistic and less time consuming moreover no MATLAB programming is required as they are in-built MATLAB functions.

4.2.3 Nomarski Interference contrast microscopy (NIC)

The BSEIA technique was successfully employed for constant loading and during overload condition to quantify the plastic strain map surrounding the fatigue crack tip for pure Titanium. However, access to FE-SEM microscope is not available to many research institutions. Fig 4.23 shows a ZEISS inverted Nomarski Interference Contrast microscope.

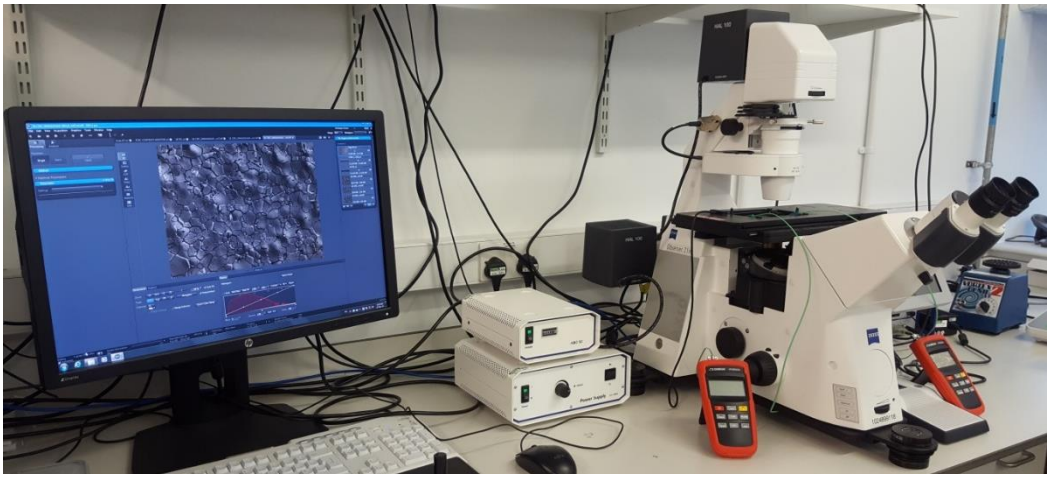

Fig 4.23: ZEISS Nomarski Interference Contrast microscope (University of Liverpool)

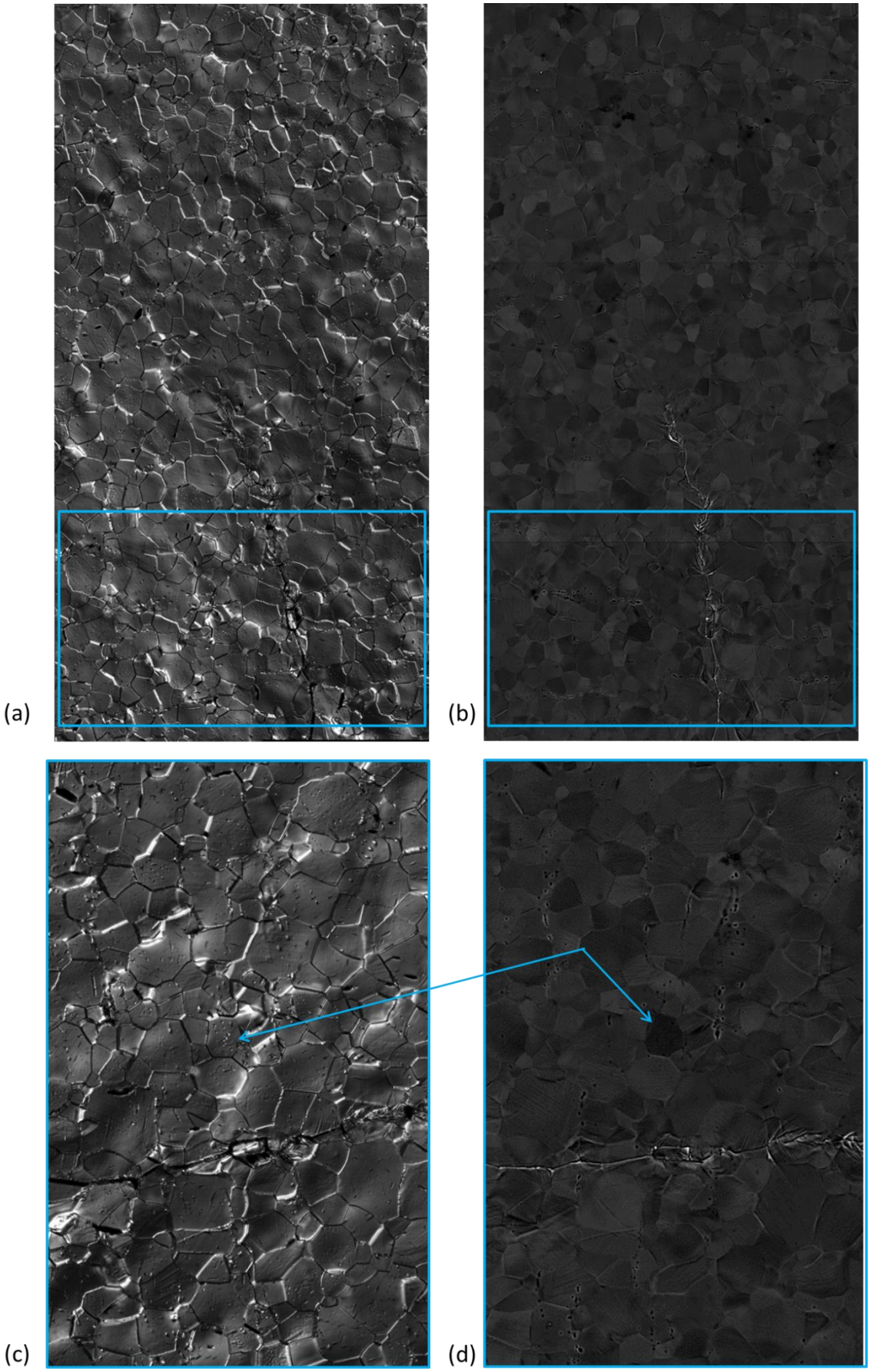

Fig 4.24: (a) NIC microscope image of a fatigue crack (b) BSE image of the same fatigue crack (c) Enlarged view of NIC image highlighted in blue (d) Enlarged view of BSE image from same location

The images captured using the Nomarski Interference Contrast microscope (NIC) resemble the BSE images captured using the FE-SEM for the same specimen at the same location as shown in Fig 4.24. Fig 4.24 (c) and 4.24 (d) are the enlarged region of Fig 4.24(a) and (b) respectively highlighted by blue box. The image in Fig 4.24(a) was capture using the NIC microscope and shows clearly visible grain boundaries, slip lines, dislocations and twins. The NIC image is sharper than the BSE image. The NIC image explains why some grains in the BSE image are darker than the rest of the grains. This is due to dislocations accumulation within the grain that makes the appearance of that particular grain dark as indicated by blue arrow in the Fig 4.24(c) and (d). The initial results were encouraging however, the NIC image shows some bright edges on grain boundaries. These bright grain boundaries are associated with the working principle of the Nomarski prism,

(1) Grain boundaries oriented perpendiculars to the shear axis are much brighter. The shear axis is the principal axis of a Nomarski prism. Rotating the specimen to a different angle illuminates other grain boundaries which will be perpendicular to the shear axis.

(2) Regions of increasing optical path difference appear much brighter such as surface relief, reflection boundaries.

(3) Some edges have very steep optical gradients due to low-bias retardation values which can be reduced by proper adjustment of the Nomarski prism position

In order to analyse and compare the NIC images with BSE images, several images were captured. Fig 4.25(a), (b) and (c) are the BSE images while (d), (e) and (f) are the NIC images. Fig 4.25(a), (b), (d) and (e) images are within the plastic region while (c) and (f) are from the elastic region away from the crack.

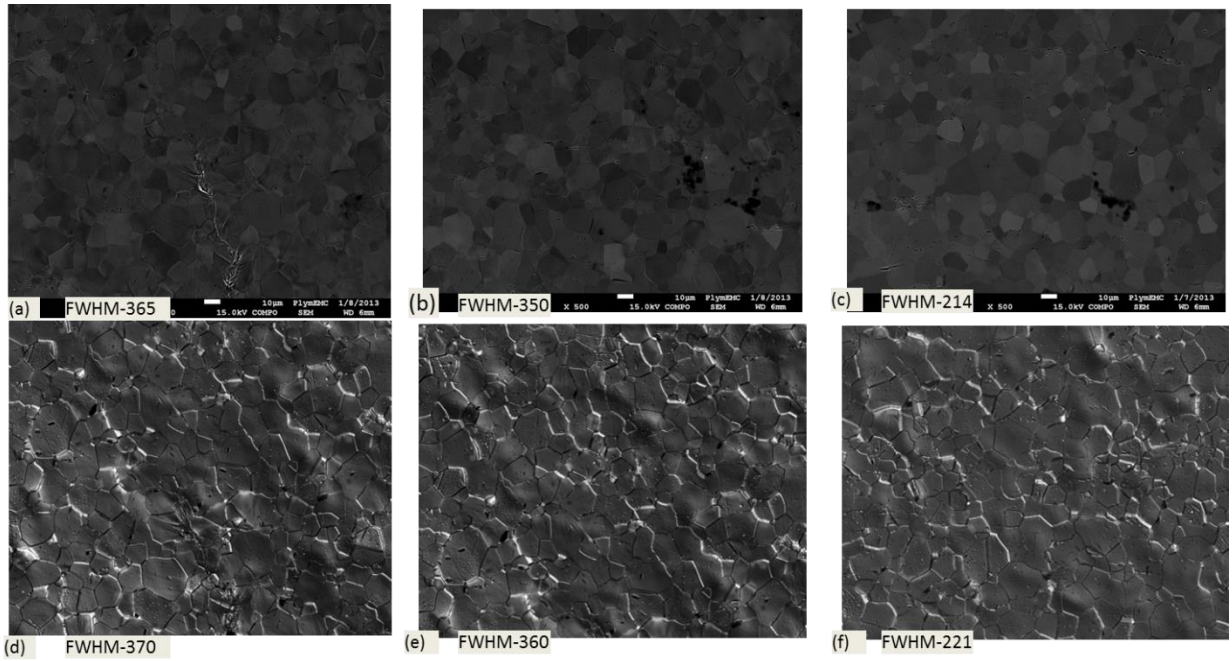

Fig 4.25: (a) BSE image surrounding the fatigue crack (b) BSE image ahead of the fatigue crack (c) BSE image within the elastic region away from the plastic region (d) NIC image surrounding the fatigue crack (e) NIC image ahead of the fatigue crack (f) BSE image within the elastic region away from the plastic region

The FWHM of all three NIC images are in accordance with the BSE images. The value of FWHM of NIC images are slightly higher than the BSE images, this could be due to bright grain boundaries in NIC images.

In order to depict all grains with a maximum contrast and minimum bright light, the Circular-Nomarski Interference Contrast (C-NIC) prism was employed which uses circularly polarised light in order to vary the image contrast. Fig 4.26 shows 3 images captured employing the C-NIC prism and 3 images captured without using the C-NIC prism.

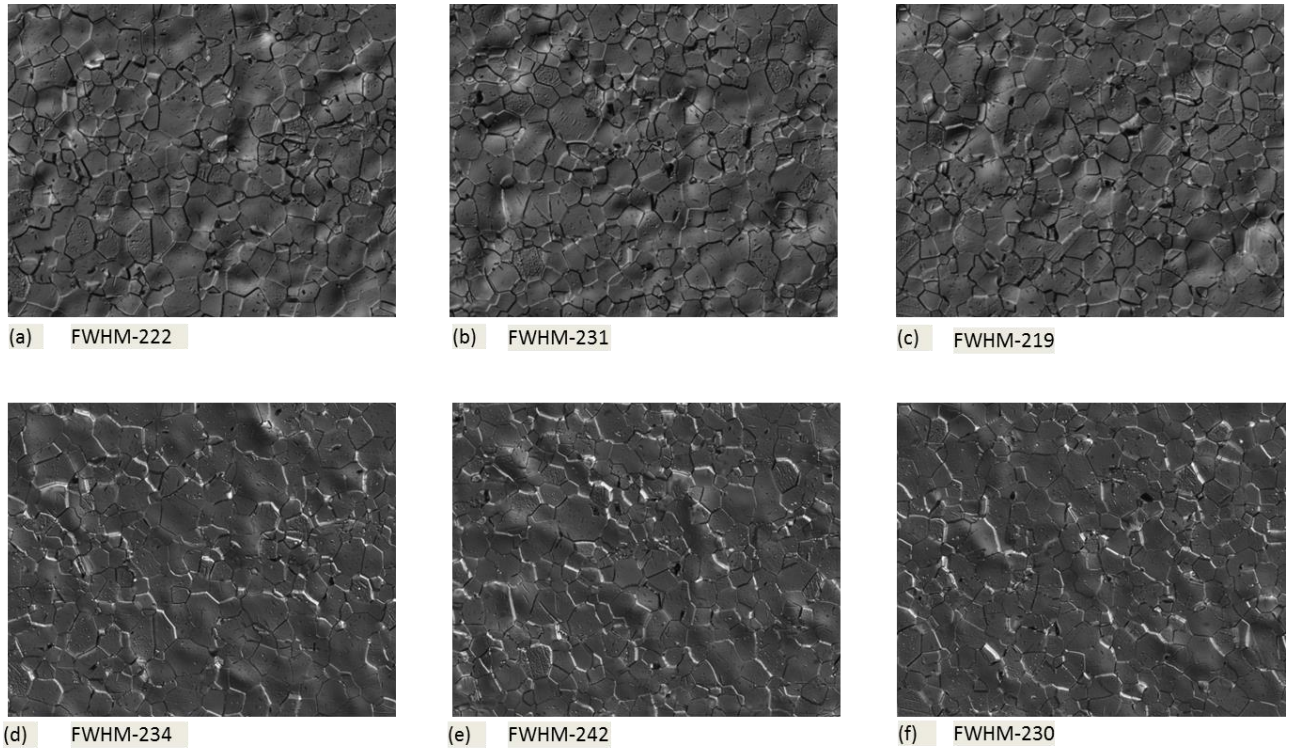

Fig 4.26: (a) , (b) , (c) images captured using C-NIC microscope within the elastic region away from the plastic region (d), (e), (f) images from the same location as top images captured using NIC microscope

The FWHM of the C-NIC images are lower than for the NIC images and compatible with the BSE images. It is concluded that NIC microscopy with a C-NIC prism could identify the crack tip plasticity in a similar way to the BSEIA technique. The cost to install and run the C-NIC microscope is considerably less than a FEG-SEM. Also, the time required to capture the images is notably reduced for the C-NIC microscope than capturing BSE images using FE-SEM. An automatic image acquisition system is also available with the C-NIC at some additional cost.

In conclusion, the initial results from C-NIC microscope are encouraging as the FWHM of BSE images and C-NIC microscope images shows the similar trend however, and it should be explored further in order to examine its potential to quantify the plasticity surrounding the fatigue crack.

Chapter 5

Characterization of the Plastic Zone

5.1 Comparison of experimental plastic zone with numerically predicted plastic zone from previous research

For decades, many researchers have made attempts to determine the size and/or shape of the plastic zone. Irwin [17] and Dugdale [18] proposed different models to estimate the plastic zone size ahead of the crack in 1957 and 1960 respectively. The plastic zone shapes adopted by Irwin and Dugdale models bear little resemblance to the actual plastic zone in metals. Von Mises and Tresca obtained a more accurate impression of plastic zone shape by examining the yield condition for non-zero angles. However, all these models are usually restricted to elastic perfectly plastic materials and do not consider the influence of strain hardening. The behaviour of the plastic zone in strain hardening materials under mode I loading were given by Hutchinson (1968) and by Rice and Rosengren (1968) and are known as HRR singularities as explained earlier [21, 22]. This analysis was extended by Shih for mixed mode loadings in 1973 [23]. He obtained an elastic-plastic solution for combined mode I and mode II loading of fatigue cracks as a function of the value of strain hardening exponent, n and plotted the resultant plastic zone contours. The plastic zone contours for small scale yielding under plane stress conditions proposed by Hutchinson in 1971 and by Shih in 1973 are shown in Fig 5.1(a) and (b) respectively for various values of strain hardening exponent [21, 23].

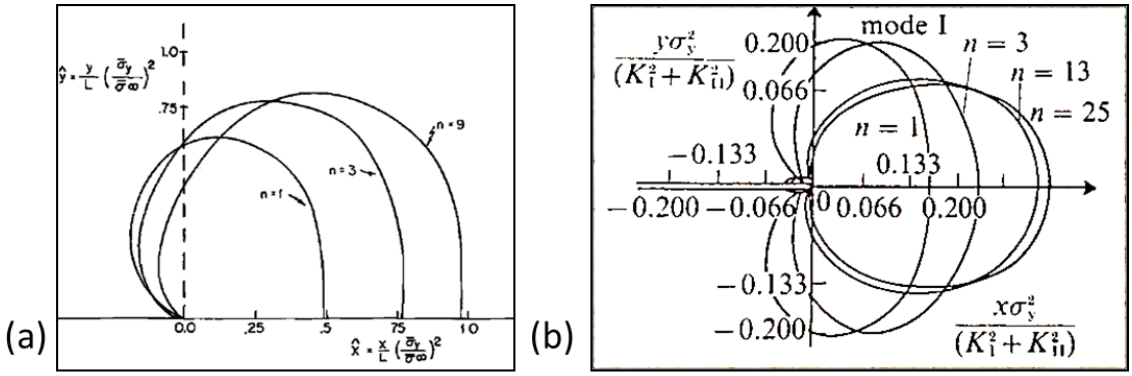

Fig 5.1: Plastic zone boundaries (a) proposed by Hutchinson 1971 (b) proposed by Shih 1973. For small scale yielding under plane stress loading for various values of strain hardening exponent

Fig 5.1 indicates that the plastic zone contours proposed by both of these researchers are different in shape and size except for a value of strain hardening exponent of n=1. According to Hutchinson's results, the size of plastic zones are increasing along X and Y axis for decreasing value of strain hardening exponent i.e. at n=3 and n=9. Also, the contours resemble the shape of the kidney or cardiac. However, according to Shih, as illustrated in Fig 5.1(b), for decreasing value of strain hardening exponent of n=3 to n=25, the size of the plastic zone starts decreasing on Y-axis and eventually becomes circular for all value of strain hardening exponent higher than 13. To evaluate this further, by following Hutchinson's methodology, the author reproduced his results in MATLAB using the following equations. According to Hutchinson, the crack tip stress field for a strain hardened material can be expressed by [21],

$$\boldsymbol{\sigma_e = Kr^{s-2}(\sigma_{rr}^2 + \sigma_{\theta\theta}^2 - \sigma_{rr}\sigma_{\theta\theta} + 3\sigma_{r\theta}^2)^{1/2}} \quad \textbf{[5.1]}$$

Where**,**

$$\boldsymbol{\sigma_{rr} = s\emptyset + \ddot{\emptyset}} \quad \textbf{[5.2]}$$

$$\boldsymbol{\sigma_{\theta\theta} = (s-1)\emptyset} \quad \textbf{[5.3]}$$

$$\boldsymbol{\sigma_{r\theta} = (1-s)\dot{\emptyset}} \quad \textbf{[5.4]}$$

$$s = \frac{2n+1}{n+1} \quad [5.5]$$

$$\emptyset = \cos\frac{\theta}{2} + \frac{1}{3}\cos\frac{3\theta}{2} \quad [5.6]$$

The plots in Fig 5.2(a) were produced by solving these equations. Fig 5.2(b) shows Hutchinson's plastic zone contours together with those the author obtained by following Hutchinson's methodology. The plastic zone contours from both are similar yet there is minor mismatch at some locations this might be due to the fact that the plots by Hutchinson are plotted in 1973 without the help of any advanced software so, the minor deviations in plots are acceptable.

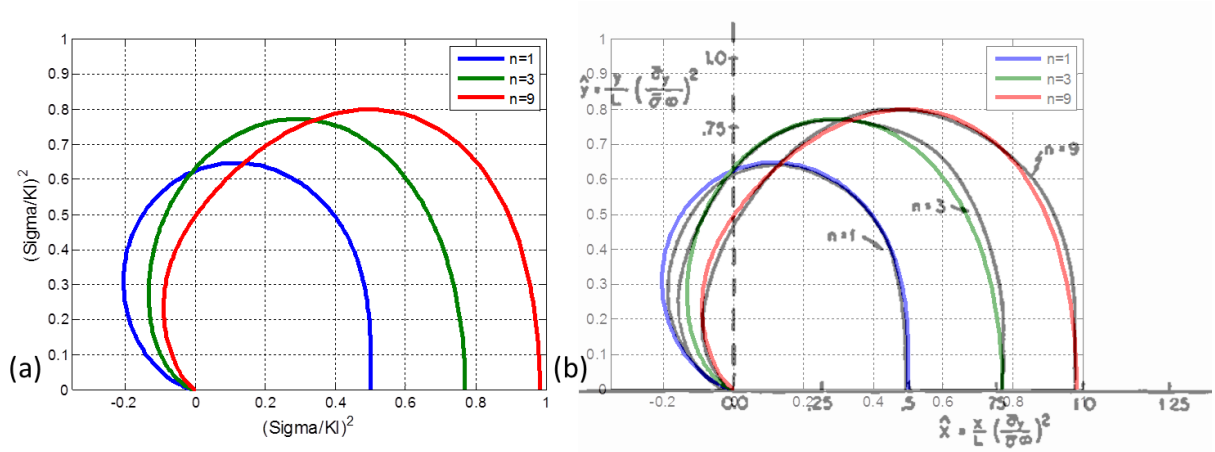

Fig 5.2: Plastic zone boundaries (a) plotted by author following Hutchinson's methodology 1971 (b) Author's plot superimposed on Hutchinson's plastic zone

It was not possible to reproduce Shih's results as he obtained his results using a specially written numerical programme. Also, the methodology he used was not clearly described in his thesis [23].

The plastic zone contours proposed by Hutchinson and Shih have never been demonstrated and validated experimentally, even though numerous studies using analytical and numerical approaches have been carried out. Hence, in the current project, the experimental plastic zone contours were obtained using the TSA technique for a range of strain hardening

exponents. Fig 5.3 shows the experimental plastic zone contours for strain hardening exponent value of 6, 8 and 14 at various crack lengths. It is evident from the Fig 5.3 that the plastic zone shape does not become circular for any value of strain hardening exponent. However this is contrary to the predictions of Shih. In addition to that, the plastic zone extends further in Y-direction with each decrease in value of strain hardening exponent from 6 through 8 to 14. This finding is consistent with findings of Hutchinson. It is concluded that experimental results do not validate Shih's predictions but they are in accordance with Hutchinson's solution.

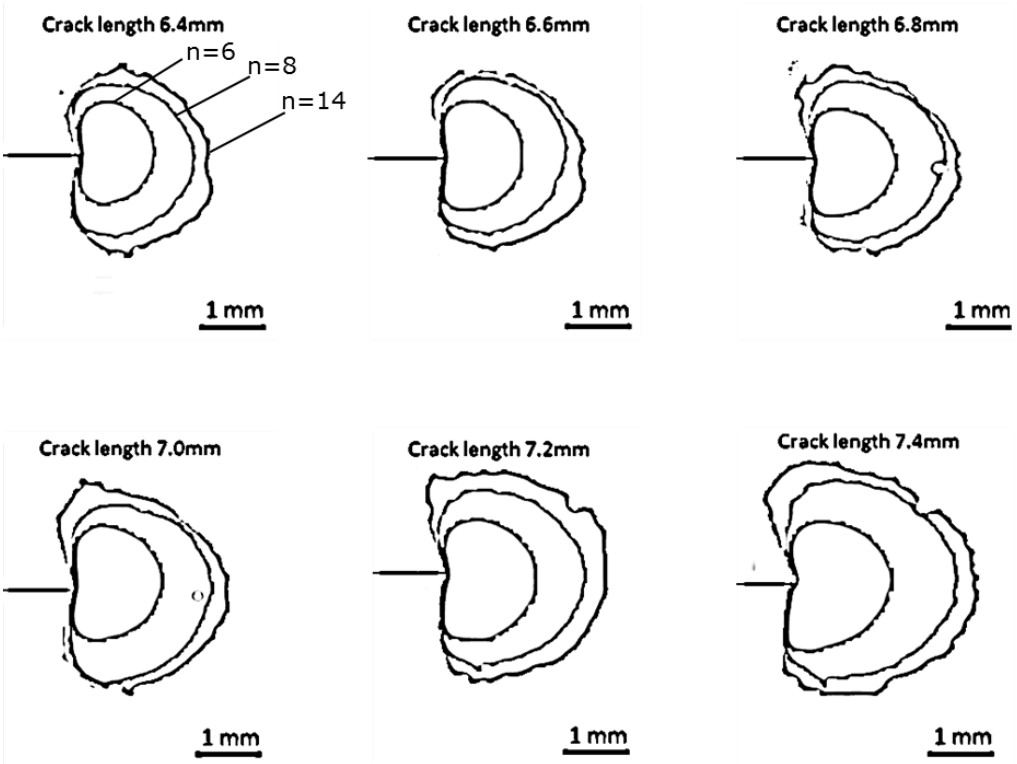

Fig 5.3: Experimental plastic zone contours obtained from TSA data at range of strain hardening exponents at various crack lengths

5.2 Characterising plastic zone using a quartic curve

There were several fatigue experiments performed as listed in Table 3 with varying load ratios at constant amplitude loading and during overloads for each material. Plastic zone contours were plotted for all these experiments. The resulting plastic zones showed a similar trend of increasing the plastic zone size in both x and y directions for decreasing levels of strain

hardening as obtained in Fig 5.3. The plastic zone contours for the 10% overload case for specimens 13, 14 and 15 are displayed in Fig 5.4.

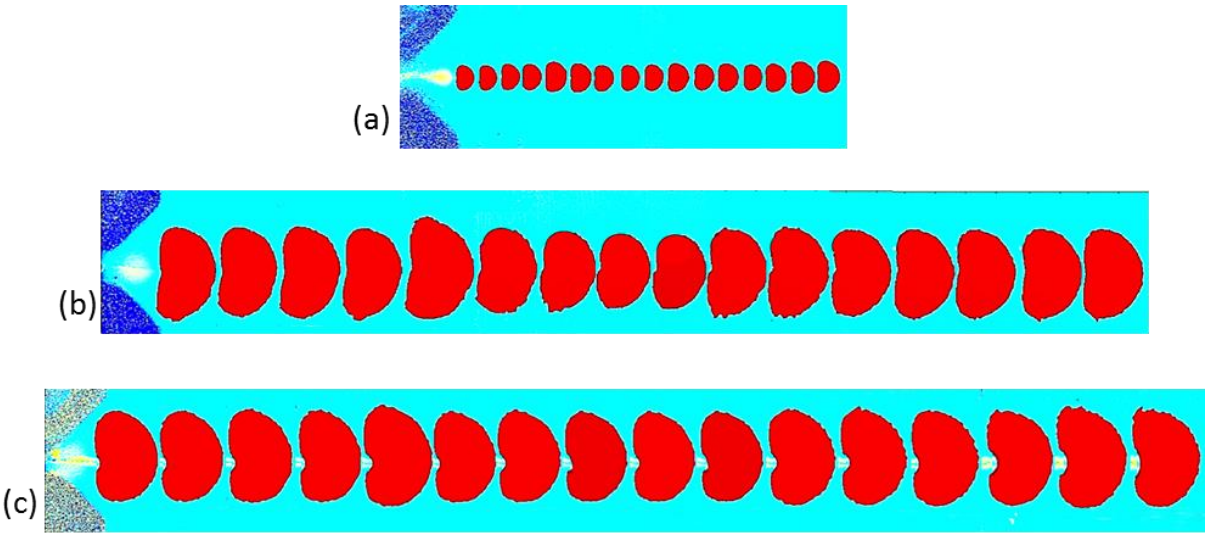

Fig 5.4: Plastic zone contours for crack lengths from 6.4 mm to 7.9 mm with 0.1 mm increment. 10% overload applied after 6.7 mm crack length at various values of strain hardening exponent (a) Titanium, n=6 (b) Al 2024-T3, n=8 (c) Al 6061-T6, n=14

It is obvious from Fig 5.4 that plastic zone contours are neither circular, as predicted by Irwin and Shih, nor like a strip as assumed by Dugdale. All previous research findings are based on finding the plastic zone radius parallel to the direction of crack growth nevertheless there is no research on modelling the plastic zone perpendicular to the direction of crack growth calculating the area of plastic zone. The radius of the plastic zone refers to a circle or a circular arc which is an inappropriate shape to describe the plastic zone.

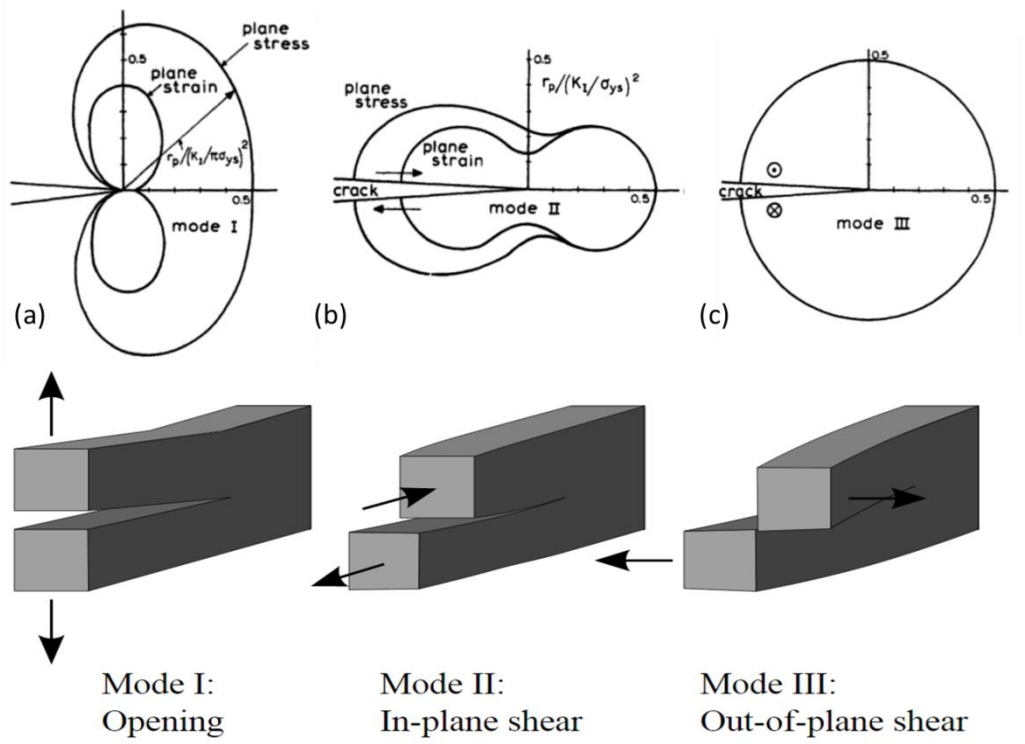

Fig 5.5: Top image: Plastic zone contours for different modes of loading during plane stress and plane strain conditions. Bottom image: The three modes of loading (a) Mode I - opening mode (b) Mode II – sliding mode (c) Mode III – tearing mode [209]

Furthermore, the shape of the plastic zone changes during different modes of loading depending on plane stress or plane strain condition as shown in Fig 5.5 where plastic zone shapes for modes I, II and III are derived on the basis of Von Mises yield criteria [209]. The bottom figure indicates three different modes of loading mode I (opening mode), mode II (sliding mode) and mode III (tearing mode). The plastic zone shape also changes for different thicknesses of specimen as shown in Fig 5.6 which clearly indicates that the plastic zone gradually decreases from the plane stress size at the surface to plane strain size in the interior of the plate. All of this evidence suggests that the radius of plastic zone is not a reliable measure.

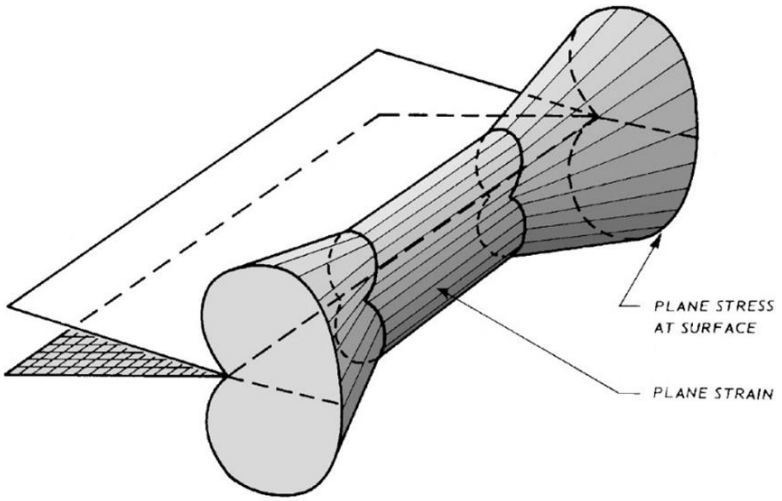

Fig 5.6: Through-thickness plastic zone in a plate of intermediate thickness [19].

Moreover, the plastic zone radius in the direction of crack growth is not similar to the plastic zone extent perpendicular to the direction of crack growth. The area of plastic zone has an additional advantage compared to the plastic zone radius as it contains the information about both shape and size of the plastic zone parallel and perpendicular to the crack growth. It has been concluded that the area of plastic zone would be a genuine measure to analyse the fatigue crack growth. Therefore it was decided to consider the area of the plastic zone as a reliable parameter to characterise the plastic work ahead of the crack tip instead of relying on either the size or shape of the plastic zone. As presented in Fig 5.3 and 5.4, the plastic zone size is dependent on the value of strain hardening exponent but the shape is independent of the value of strain hardening exponent. The shape of the plastic zone resembles the shape of a kidney. There are several families of geometric curves such as algebraic, caustic and polar curves. Amongst them, two curves that resembles the shape of a kidney are the bean curve (a member of the algebraic family of curves) and a cardioid (from polar curve family) as shown in Fig 5.7 hence it was proposed to model the plastic zone size using these curves in order to find its area.

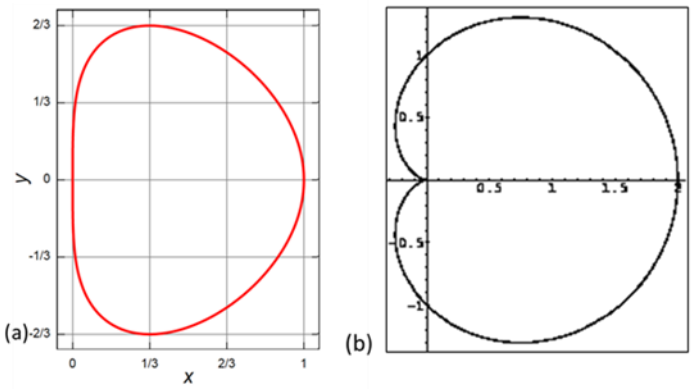

Fig 5.7: Schematic representation of (i) bean curve (ii) cardioid curve [210]

The algebraic curve is a curve whose equation involves only algebraic functions. These functions in their most general form can be written as the sum of a set of polynomials in x multiplied by powers of y, which is equal to zero. The bean curve is a plane algebraic quartic curve of the fourth degree defined by the equation,

$$(ax)^4 + (ax)^2(by)^2 + (by)^4 = ax((ax)^2 + (by)^2) \quad \textbf{[5.7]}$$

By substituting Irwin's plastic zone size equation,

$$r_p = \frac{1}{\pi}\left[\frac{\Delta K_I}{\sigma_y}\right]^2 \quad \textbf{[5.8]}$$

And Dugdale' plastic zone size equation,

$$r_p = \frac{\pi}{8}\left[\frac{\Delta K_I}{\sigma_y}\right]^2 \quad \textbf{[5.9]}$$

as 'a' and 'b' respectively in equation [5.7] , the final equation is,

$$\left[\frac{\Delta K_I}{\sigma_y}\right]^2 [[8^2x^2+\pi^4y^2]^4 - 8^2\pi^4x^2y^2] - 8^2\pi^3x[8^2x^2 - \pi^2y^2] = 0 \quad \textbf{[5.10]}$$

The plastic zone predicted using the above equation for a crack length of 6.4 mm for three value of strain hardening exponent are shown in Fig 5.8 together with the corresponding experimental plastic zone showing a good agreement between them.

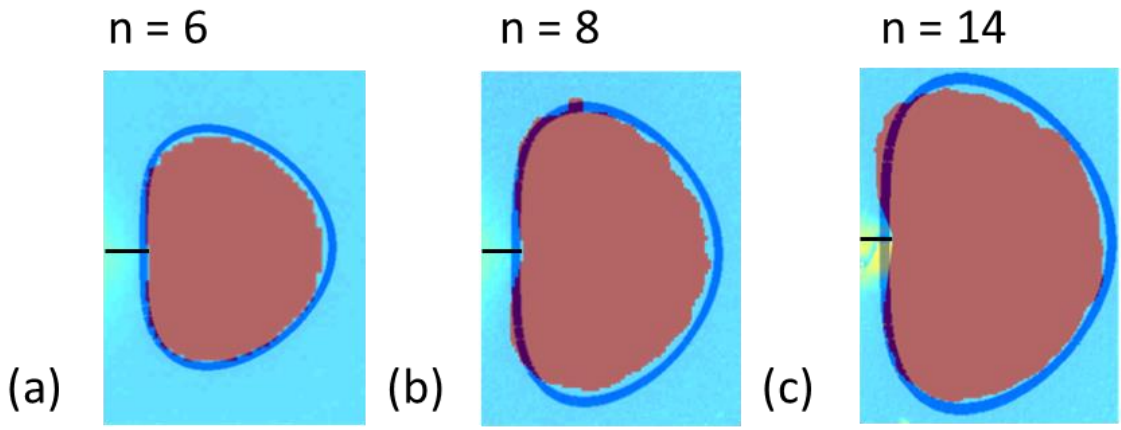

Fig 5.8: Experimental plastic zone (red) together with the plastic zone found using bean curve (blue)

Similarly, the plastic zone was predicted using the cardioid curve which is a polar curve. Cardioid is an epicycloid with one cusp at the origin represented by,

$$x = a\cos\theta(1-\cos\theta); \quad y = b\sin\theta(1-\cos\theta) \qquad [5.11]$$

Substituting equations, [5.8] and [5.9] in equation [5.11], the final equations to define the plastic zone are,

$$x = \frac{1}{\pi}\left[\frac{\Delta K_I}{\sigma_y}\right]^2 \cos\theta(1-\cos\theta); \quad y = \frac{\pi}{8}\left[\frac{\Delta K_I}{\sigma_y}\right]^2 \sin\theta(1-\cos\theta) \qquad [5.12]$$

The plastic zone predicted using the above equations are shown in Fig 5.9 together with the corresponding experimental plastic zones.

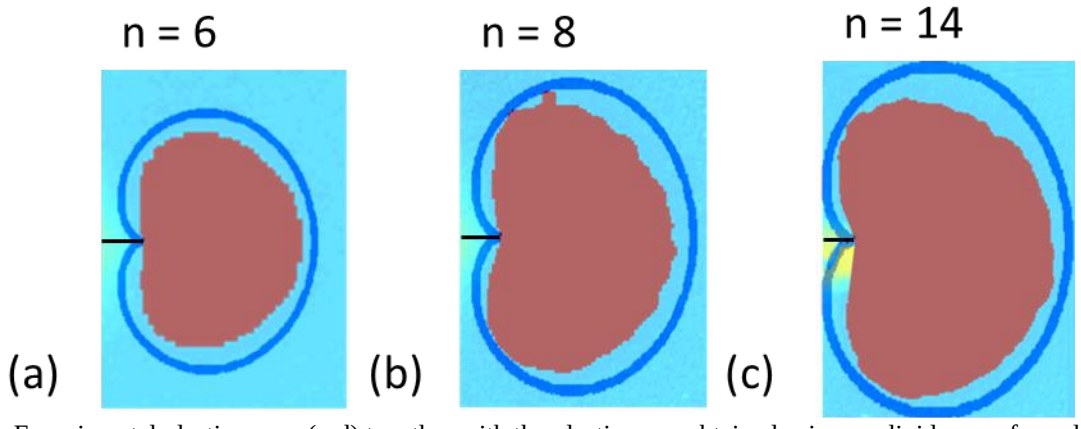

Fig 5.9: Experimental plastic zones (red) together with the plastic zone obtained using cardioid curve for value of strain hardening exponent (a) n=6 (b) n=8 (c) n=14

It is evident from the Fig 5.9 that the cardioid curve models the plastic zone radius well ahead of the crack but it does not fit well perpendicular to the direction of crack growth. This is due to the nature of cardioid curve. This can be explained using Fig 5.10 where cardioid curve is shown along with the plastic zone plotted using Irwin (green circle) and Dugdale (red circle) criteria. It is clear from the figure that the plastic zone predicted by cardioid matches well with the Irwin's plastic zone along the x-axis. However, in the y-axis, it does not match well with the Dugdale plastic zone as the cardioid in y-axis extends beyond the Dugdale's plastic zone as shown by the two horizontal tangents (black line) to the Dugdale plastic zone (red circle). Also, the cardioid extends on both the side of the cusp beyond the vertical tangent line to the Irwin and Dugdale plastic zone. All these result in an overestimate of the plastic zone area hence it was concluded that the cardioid curve is less good for characterizing the plastic zone.

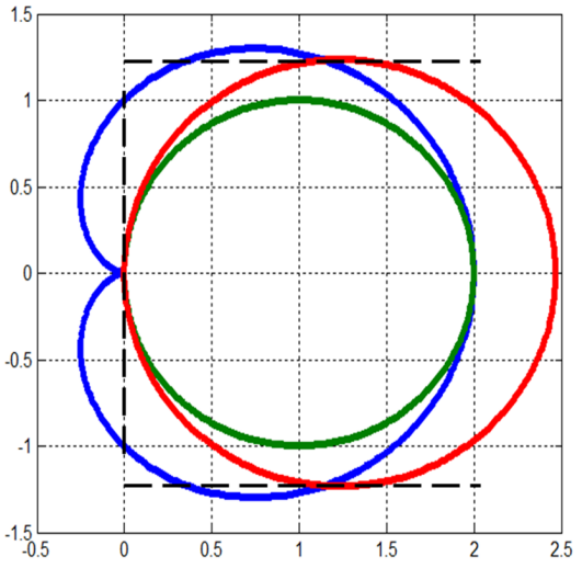

Fig 5.10: The cardioid plastic zone (blue) achieved using equation [6.12] along with the contours of plastic zone plotted using Irwin (red circle) and Dugdale (green circle) criteria. The horizontal dashed black line denotes the tangents to the Dugdale plastic zone and vertical black line shows the tangents to Irwin and Dugdale plastic zone. The cardioid plastic zone extends beyond all three tangents overestimating the plastic zone area

The experimental plastic zones predicted using a bean curve for constant amplitude loading for all values of strain hardening exponent considered are presented in Fig 5.11 for various crack lengths. It is apparent from the figure that the bean curve has a great potential to

model the plastic zone size because there is good agreement between the plastic zone found using proposed method and corresponding experimental plastic zone.

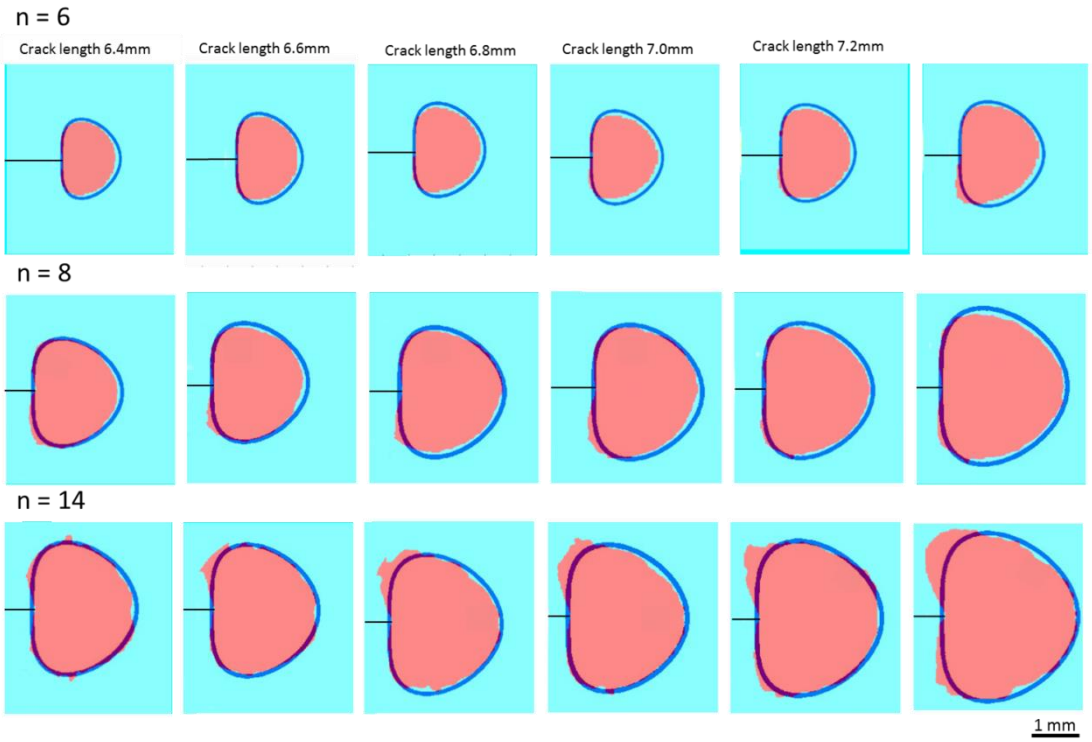

Fig 5.11: The plastic zone size abstained using bean curve (blue) superimposed on experimental plastic zones (red) for value of strain hardening exponent, n=6, 8 and 14

Fig 5.12 compares the plastic zone area found experimentally and predicted using the bean curve. The experimental data is in close agreement with the plastic zone area calculated using the bean curve at all crack lengths.

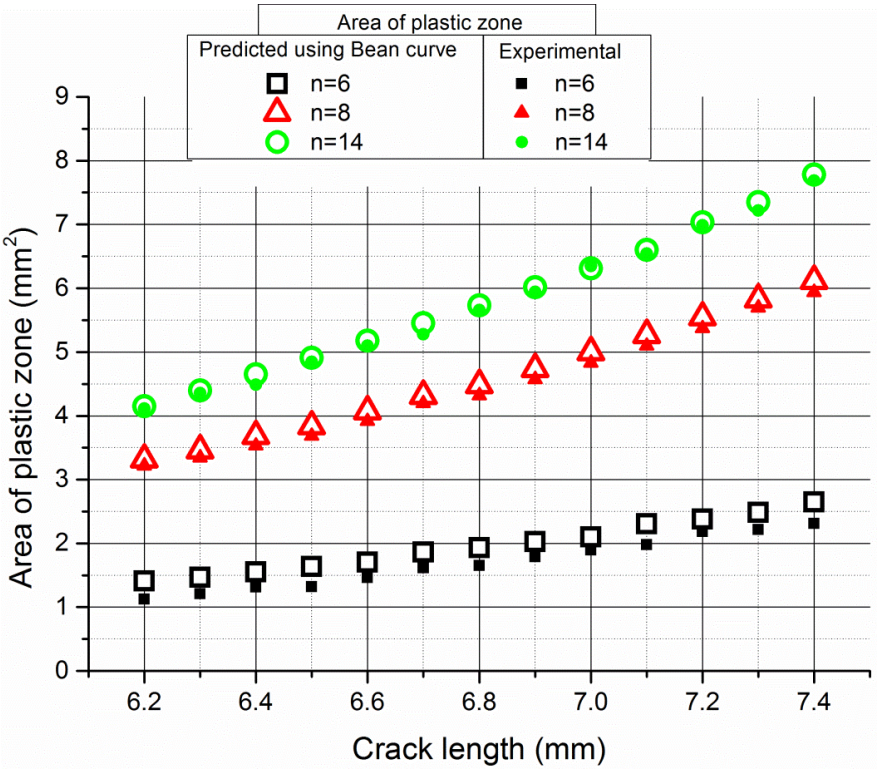

Fig 5.12: Comparison of area of plastic zone found experimentally and using a bean curve at various crack lengths for three value of strain hardening exponent at constant amplitude loading

It is noticeable in Fig 6.12 that the difference of the area of plastic zone between the experimentally measured and predicted using a novel method is higher for higher strain hardening (n=6) exponent compared to the lower value of strain hardening exponent (n=14). This is due to the fact that the plastic zone characterized using a bean curve is dependent on Irwin and Dugdale's estimates of plastic zone radius. These estimates typically assume an elastic-perfectly plastic material response. However, in reality, the three materials strain hardens and has different value of strain hardening exponent, so the experimental plastic zone size is smaller for the material with highest value of strain hardening exponent. As the value of material's strain hardening exponent decreases, its capacity to strain harden decreases resulting in less difference between the experimental and predicted plastic zone size compared to higher value of strain hardening exponent. It is significant that the novel method is able to detect a difference in the plastic zone size for experiments conducted at various values of strain hardening exponent. This highlights the potential of the novel method to evaluate the phenomenon of plasticity induced crack closure.

Chapter 6

Conclusions

The present project was undertaken to characterise the plastic zone of a fatigue crack experimentally and numerically at various values of strain hardening exponent. To characterise the plastic zone experimentally at the macro scale and micro scale, two techniques Thermoelastic Stress Analysis (TSA) and Back Scattered Electron Image Evaluation (BSEIA) have been employed. To characterise the plastic zone at a range of strain hardening exponents, three varied materials viz. pure Titanium (n= 6), Al 2024-T3 (n= 8), and Al 6061-T6 (n= 14), were chosen whose value of strain hardening exponent was calculated experimentally.

The TSA system was employed to monitor the fatigue experiments on compact tension specimens of all three materials to investigate the effect of value of strain hardening exponent on plastic zone size and shape and on plasticity-induced crack closure during constant amplitude loading and after the application of overload. The experimental plastic zone size and shape were determined by applying a binary filter to a phase image obtained from TSA.

1. **Effect of value of strain hardening exponent on plastic zone size**

   The comparison of theoretical plastic zone radius and experimental plastic zone radius achieved by employing TSA technique showed a good level of agreement between them for all value of strain hardening exponent. The experimental results suggests that, at a higher value of strain hardening exponent (n=6), the radius of the plastic zone is smaller than for a lower value of strain hardening exponent (n=14) for the same crack length. The experiments also suggests that the size of plastic zone radius increases rapidly at the lower value of strain hardening exponent (n=14) than that at the higher n-

value (n=6). The value of strain hardening exponent is related to the plastic deformation of the material. There is less stress redistribution occurs in the material with higher value of strain hardening exponent n, due to pile up of dislocations resulting in the small plastic zone size compared to lower value of strain hardening exponent. The experimental results support the conclusion that the value of strain hardening exponent has a major influence on plastic zone size.

2. Effect of value of strain hardening exponent on crack closure

It was found that the values of experimental ΔK_I are less than the theoretical values of ΔK_I for three load ratios (0.1, 0.33, 0.5) suggesting the presence of crack closure. However, the level of crack closure was different in all three materials with different value of strain hardening exponent. It has been observed that, at lower value of strain hardening exponent, the difference between the values of experimental and theoretical ΔK_I is less compared to that for the higher value of strain hardening exponent which suggests that the value of strain hardening exponent influences the extent of crack closure. As the load ratio increases, the values of experimental ΔK_I tend to approach the theoretically predicted values of ΔK_I suggesting that there is a reduction on crack closure level and this reduction is associated with the value of strain hardening exponent i.e. higher the value of strain hardening exponent, lower the reduction in crack closure level. These experimental evidence leads to a conclusion that the value of strain hardening exponent has a notable influence on crack closure phenomena.

3. Effect of value of strain hardening exponent on overload

Overloads were applied to a series of specimens while the plastic zone size and stress intensity factor were monitored using the data from TSA system. After an overload had been applied, the plastic zone size was larger, ΔK_I smaller and the growth was slowed

and it was observed that these changes were proportional to the applied overloads. Also, at a higher value of strain hardening exponent, the decrease in ΔK_I is more significant than that for the lower value of strain hardening exponent. As the crack propagated through the enlarged plastic zone, the area of crack tip plastic zone reduced while the ΔK_I values and the growth rate increased and returned to approximately the pre-event values when the post-overload growth equalled the plastic radius at the overload. The crack growth retardation was higher for higher value of strain hardening exponent at a higher overload. All these support the conclusion that the value of strain hardening exponent plays a major role on size of the plastic zone, values of ΔK_I and crack growth retardation demonstrating that it is an important material parameter.

4. Experimental characterisation of plastic zone at micro-scale using a Back Scattered Electron Image Evaluation (BSEIA) technique

The plastic strain around a fatigue crack subjected to overload in pure Titanium compact tension specimen has been evaluated by employing a Back Scattered Electron Image Evaluation (BSEIA) technique based on using the discrete Fourier transform to analyse the structure of Back Scattered Electron (BSE) images. The full-width at half maximum of the magnitude of the Discrete- Fourier Transform (DFT) of the BSE images was used as a measure of the level of plasticity based on the distortion of grains caused by dislocation accumulation during plastic deformation. The technique was calibrated using images obtained from a uniaxial tension test performed in-situ in the Scanning Electron Microscope (SEM) so that the magnitude of the average plastic strain in the field of view of an image could be related to the Full Width at Half of the Maximum (FWHM) for the image. The crack was initiated from the notch and TSA data were collected after crack growth of 3.0 mm on one side of the specimen followed by observation in the SEM and BSE image capture on the other side after completion

of each experiment. The results from the two techniques are in general agreement. The value of the experimental radius of the plastic zone perpendicular to the crack growth found from the TSA data is in between the values of radius plastic zone perpendicular and parallel to the crack growth found using the BSEIA technique. All three values are nearly similar and exhibit very good agreement with the theoretical radius of plastic zone calculated using Dugdale's approach. Immediately after a 50% overload for 10 cycles the plastic zone area calculated from BSEIA increased by 60% while the plastic zone area found from TSA data exhibits an increase of 57% which shows an excellent agreement between the techniques. After the application of an overload the area of the plastic zone starts decreasing until it reaches the pre-event value predicted by theory. Crack tip plasticity has been established as a cause of crack closure and an increase in the crack tip plastic zone size due to the application of an overload would intensify the effect of plasticity-induced shielding of the crack tip and crack closure as supported by BSEIA observations. It has been concluded that BSEIA technique is able to measure the changes in plastic zone radius associated to overload and so it has a great potential in identifying the role of crack tip plastic zone in crack closure and plasticity-induced shielding.

5. Application of BSEIA technique to the other materials

The BSEIA study was expanded to use the technique for the Al 2024-T3 and Al 6061-T6 materials used in present research. The mechanical polishing and electropolishing techniques were developed suitable for both the materials. Unfortunately, these materials developed severe etch pits during electropolishing process and their grain boundaries were not clearly visible due to the different atomic number of the materials in these alloys. So, it was concluded that the BSEIA technique is not applicable to Aluminium alloys.

6. The C-NIC technique - an alternative to BSEIA technique

Considering the facts that, the access to FE-SEM microscope is not available to many research institutes, the cost of running the SEM and image acquisition time is higher, the use of Circular Nomarski Interference contrast microscopy (C-NIC) was suggested. The FWHM of the C-NIC images were compatible with the BSE images. It has been concluded that the results from C-NIC microscope should be explored further in order to examine its potential to quantify the plasticity surrounding the fatigue crack.

7. The comparison of experimental plastic zone contours with the plastic zone contours predicted by previous researchers

The plastic zone contours for small scale yielding under plane stress conditions proposed by Hutchinson in 1971 and by Shih in 1973 have never been demonstrated and validated experimentally. Hence, in the current project, the experimental plastic zone contours were obtained using the TSA technique for a range of strain hardening exponents. The plastic zone contours proposed by both of these researchers are different in shape and size except for a value of strain hardening exponent of n=1. The author reproduced Hutchinson's plastic zone contours by following his methodology and there was a very good agreement between the plastic zone contours achieved by Hutchinson and the same reproduced by the author. However, the experimental results do not match with the numerically predicted plastic zone contours of Shih for all value of strain hardening exponent. It has been concluded that experimental results do not validate Shih's predictions but they are in accordance with Hutchinson's solution.

8. Characterisation of the plastic zone using a novel method

The radius of the plastic zone refers to a circle or a circular arc which is an inappropriate shape to describe the plastic zone. Furthermore, the shape of the plastic zone changes during different modes of loading depending on plane stress or plane strain condition.

The area of plastic zone has an additional advantage compared to the plastic zone radius as it contains the information about both shape and size of the plastic zone parallel and perpendicular to the crack growth. Hence, a novel methodology to characterise the plastic zone size during fatigue crack growth has been developed. This methodology is based on the fact that the plastic zone size is dependent on the value of strain hardening exponent but the shape is independent of the value of strain hardening exponent. The plastic zone size was determined by applying Irwin and Dugdale's plastic zone radius as variables in the equation of a bean curve which is a plane algebraic quartic curve. It was concluded that the bean curve has great potential to model the plastic zone size because there is good agreement between the plastic zone found using proposed method and corresponding experimental plastic zone for all three value of strain hardening exponent. It can be concluded that the novel methodology provides an improved prediction of the crack tip plastic zone area compared with theoretical predicted models which either relies on plastic zone size or shape.

Concluding Remark:

This doctoral dissertation provides the following original contributions in the field of fracture mechanics,

1) A comprehensive study of the effects of value of strain hardening exponent on crack closure and overloads on fatigue cracks in terms of the experimental stress intensity factors, radius of crack tip plastic zones and crack growth rates.
2) Experimental characterisation of plastic zone at micro-scale using a Back Scattered Electron Image Evaluation (BSEIA) technique before, during and after the application of overload.

3) The experimental validation of the plastic zone contours for small scale yielding under plane stress conditions proposed by Hutchinson in 1971. Shih's theory has not been validated with the experimental results obtained in this work
4) A novel method to model the crack tip plastic zone size using a mathematical function.

This doctoral dissertation provides understanding of the effect of value of strain hardening exponent on the structural behaviour of engineering materials. This work shows how materials of various values of strain hardening exponent behaves after application of overload and in the presence of crack closure. The technique utilizing thermoelastic stress analysis can be used to study different fracture scenarios and materials to increase the understanding in the effects of crack closure on fatigue crack growth rate. The novel method to model the plastic zone will help develop better post-fracture life prediction model that can be used for less conservative, energy saving engineering designs.

Chapter 7

Future Works

To gain a deeper understanding of how value of strain hardening exponent affects the size of the plastic zone, crack closure and overload retardation, series of further experimental studies are suggested:

(1) In the current project, three value of strain hardening exponent were chosen ranging from 6 to 14. It is proposed that in future, the study should be performed on materials such as copper, 304 annealed mild steel whose value of strain hardening exponent is very high (n≈2)

(2) The current study was focused on experimental plastic zone for plane stress condition. It is recommended that in future the experiments should be performed for plane strain condition.

(3) At present, the BSEIA technique was only applicable to pure Titanium. Further work needs to be done to establish the other materials whose plastic zone can be characterised using this technique

(4) The initial results from C-NIC microscope were encouraging and they should be explored further in order to examine its potential to quantify the plasticity surrounding the fatigue crack.

(5) The novel method proposed to evaluate the plastic zone using a bean curve was applied to the plastic zone for constant amplitude loading. Further research is needed to determine its applicability during the overload scenario.

References

1) http://climate.nasa.gov/climate_resources/24

2) PPMC 2015 Research Brief: Renewable energy and transport–Decarbonising Fuel in the Transport Sector

3) U.S. Department of Energy, Energy Information Administration, Independent Statistics & Analysis. (2016, March 9). Country Analysis Brief: United Kingdom

4) USAF Damage Tolerant Design Handbook: Guidelines for the Analysis and Design of Damage Tolerant Aircraft Structures, Peggy C. Miedlar, Alan P. Berens, Allan Gunderson, and J.P. Gallagher

5) NDT Education Resource Centre, www.ndt-ed.org

6) Metal Fatigue in Engineering (Second ed.) by Stephens, Ralph I.; Fuchs, Henry O. (2001). John Wiley & Sons, Inc. p. 69

7) Schutz, W. (1996). "A history of fatigue". Engineering Fracture Mechanics 54: 263–300

8) Fatigue Failure Analysis Case Studies by Zamanzadeh, Mehrooz,Larkin, Edward, Mirshams, Reza, Journal of Failure Analysis and Prevention 2015,V 15,1864-1245

9) Aviation Accident Report, National Transportation Safety Board AAR-90-06

10) http://webarchive.nationalarchives.gov.uk/20131001175041/http://www.railreg.gov.uk/upload/pdf/incident-hatfield-secondinterim.pdf

11) S.J Findlay, N.D Harrison, Why aircraft fail, Materials Today, Volume 5, Issue 11, November 2002, Pages 18-25, ISSN 1369-7021

12) Kim, W.H.; Laird, C. (1978). Crack Nucleation and State I Propagation in High Strain Fatigue- II Mechanism. Acta Metallurgica. pp. 789–799.

13) Paris, P., Erdogan, F., 1963. A critical analysis of crack propagation laws. J. Basic Eng. Trans. ASME, 528–534

14) T. L. Anderson, "Fracture Mechanics: Fundamentals and Applications" (1995) CRC Press,

15) Fine, M.E. and Davidson, D.L., Quantitative measurement of energy associated with a moving crack in Fatigue Mechanisms: Advances in quantitative measurement of physical damage. American Society for Testing and Materials, 1983. p. 350-370

16) Hahn, G.T. and Rosenfield, A.R., Sources of fracture toughness: the relation between K and the ordinary tensile properties of metals in applications related phenomenon in Titanium alloys. American Society for Testing and Materials, 1968. p. 5-32.

17) Irwin G (1957), Analysis of stresses and strains near the end of a crack traversing a plate, Journal of Applied Mechanics 24, 361–364

18) Dugdale, D. S. (1960), "Yielding of steel sheets containing slits", Journal of the Mechanics and Physics of Solids, 8 (2): 100–104

19) H.L. Ewalds, R. J. H. Wanhill, Fracture Mechanics, Butterworth-Heinemann Ltd, May 1984

20) Hahn, G.T. and Rosenfield, A.R., Sources of fracture toughness: the relation between K and the ordinary tensile properties of metals in applications related phenomenon in Titanium alloys. American Society for Testing and Materials, 1968. p. 5-32.

21) Hutchinson, J.W., 1968a. Singular behaviour at the end of a tensile crack in a hardening material. Journal of the Mechanics and Physics of Solids 16, 13–31. Hutchinson, J.W., 1968b. Plastic stress and strain fields at a crack tip. Journal of the Mechanics and Physics of Solids 16, 337–347

22) Rice, J.R., Rosengren, G.F., 1968. Plane strain deformation near a crack tip in a power law hardening material. Journal of the Mechanics and Physics of Solids 16, 1–12.

23) Shih, C.F., 1973. Elastic–plastic analysis of combined mode crack problems, Ph.D. Thesis, Harvard University, Cambridge, MA

24) Ramberg, W., & Osgood, W. R. (1943). Description of stress–strain curves by three parameters. Technical Note No. 902, National Advisory Committee For Aeronautics

25) S.N. Atluri, M. Nakagaki J-Integral estimates for strain-hardening materials in ductile fracture problems, AIAA J., 15 (7) (1977), pp. 831–92

26) Panayotounakos, D. E. and Markakis, M.: Closed form solutions of the differential equations governing the plastic fracture field in a power-law hardening material with low strain-hardening exponent. Ingenieur-Archiv 60 (1990) 444-462

27) Dong, P. and Pan, J. (1990). Plane-strain mixed-mode near-tip fields in elastic perfectly plastic solids under small scale yielding conditions. International Journal of Fracture 45, 243–262

28) Loghin, A., Joseph, P.F., Mixed mode fracture in power law hardening materials near Mode I, Int. J. Fract., 123, 2003, 81–106

29) A. Sotiropoulou, N. Panayotounakou, D. Panayotounakos Analytic parametric solutions for the HRR nonlinear elastic field with low hardening exponents, Acta Mechanica , 2006; 183(3):209 230

30) S.A. English, N.K. Arakere, Effects of the strain-hardening exponent on two-parameter characterizations of surface-cracks under large-scale yielding Int. J. Plast., 27 (2011), pp. 920–939

31) Md. Arefin Kowser, Md. Mahiuddin, An Iteration Method for Near-tip singular fields of a crack in a Power-law Hardening Material Using Asymptotic Analysis, ICMIME 2013, At Rajshahi, Bangladesh

32) W. Elber, Fatigue crack closure under cyclic tension, Engng Fracture Mech. 2, 37-45 (1970)

33) Endo, K., Okada, T., Komai, K. and Kiyoto, M. (1972) Fatigue crack propagation of steel in oil. Bull. JSME. 15, 1316–1323

34) Pineau, A. G. and Pelloux, R. M. (1974) Influence of strain-induced martensitic transformations on fatigue crack growth rates in stainless steels. Metall. Trans. 5, 1103–1112

35) Suresh, S., Zamiski, G. F. and Ritchie, R. O. (1982) Oxide-induced crack closure: an explanation for near-threshold corrosion fatigue crack growth behaviour Metall. Trans. A: Phys. Metall.

Mater. Sci., 12A, 1435–1443

36) Walker, N. and Beevers, C. J. (1979) Fatigue crack closure mechanism in titanium. Fatigue Fract. Engng. Mater. Structs. 1, 135–148

37) R. Branco, D. Rodrigues, F. Antunes Influence of through-thickness crack shape on plasticity induced crack closure Fatigue Fract Engng Mater Struct, 31 (2008), pp. 209–220

38) C.H. Wang, L.R.F. Rose, J.C. Newman Closure of plane strain cracks under large scale yielding conditions Fatigue Fract Engng Mater Struct, 25 (2002), pp. 127–139

39) J. Wang, J.X. Gao, W.L. Guo, Y.P. Shen, Effects of specimen thickness, hardening and crack closure for the plastic strip model, Theoretical and Applied Fracture Mechanics, Volume 29, Issue 1, April–May (1998), Pages 49-57

40) J.C. Newman Jr., H. Armen Jr. Elastic–plastic analysis of a propagating crack under cyclic loading AIAA J., 13 (1975), pp. 1017–1023

41) W. Guo Fatigue crack closure under triaxial stress constraint—I. Experimental investigation Engng. Fract. Mech., 49 (1994), pp. 265–275

42) C.Y. Kim, J.H. Song Fatigue crack closure and growth behaviour under random loading Engng. Fract. Mech., 49 (1994), pp. 105–120

43) N.E. Ashbaugh, B. Dattaguru, M. Khobaib, T. Nicholas, R.V. Prakash, T.S. Ramamurthy, B.R. Seshadri, R. Sunder Experimental and analytical estimates of fatigue crack closure in an aluminium copper alloy, I Fatigue Fract. Engng. Mater. Struct., 20 (1997), pp. 951–961

44) N.A. Fleck Finite element analysis of plasticity-induced crack closure under plane strain conditions Engng. Fract. Mech., 25 (1986), pp. 441–449

45) Hoffmann M, Seeger T. Dugdale solutions for strain hardening materials, the crack tip displacement in elastic–plastic fracture mechanics. In: Workshop on the CTOD Methodology, Geesthacht (Germany), 1985, pp. 57–77

46) X.G. Chen, X.R. Wu, M.G. Yan Dugdale model for strain hardening materials Engng. Fract. Mech., 41 (1992), pp. 843–871

47) S.R. Daniewicz A closed-form small-scale yielding collinear strip yield model for strain hardening materials Engng. Fract. Mech., 49 (1994), pp. 95–103

48) P.S. Theocaris, E.E. Gdoutos The modified Dugdale-Barenblatt model adopted to various configurations in metals Int. J. Fracture, 10 (1974), pp. 549–564

49) R. E. Jones, Fatigue crack growth retardation after single cycle peak overload in T&II-4V titanium alloy. Engineering Fracture Mech 5, 585-604 (1973).

50) J. F. Knott and A. C. Pickard, Effects of overloads on fatigue crack propagation: aluminium alloys. Met. Sci. 11, 399-404 (1977)

51) J. F. Knott and A. C. Pickard, Effects of overloads on fatigue crack propagation: aluminum alloys. Met. Sci. 11, 399-404 (1977)

52) Shin, C. S. and Hsu, S. H. (1993) On the mechanisms and behaviour of overload retardation in AISI-304 stainless steel. Int. J. Fatigue , 15, 181–192.

53) Christensen RH. Fatigue crack, fatigue damage and their detection. Metal fatigue. New York:

MacGraw-Hill; 1959.

54) Shijve J, Broek D. The result of a test program based on a gust spectrum with variable amplitude loading. Aircraft Engng 1962;34:314–6

55) Vecchio RS, Hertzberg RW, Jaccard R. On the overload induced fatigue crack propagation behavior in aluminium and steel alloys. Fatigue Engng Mater Struct 1984;7(3):181–94.

56) Ward-Close CM, Ritchie RO. On the role of crack closure mechanisms in influencing fatigue crack growth following tensile overloads in a titanium alloy: near threshold versus higher DK behaviour. In. Mechanics of fatigue crack closure, ASTM STP 982. Philadelphia: American Society for Testing and Materials; 1988. p. 93–111.

57) Jones RE. Fatigue crack growth retardation after single-cycle peak overload in Ti–6Al–4V titanium alloy. Engng Fract Mech 1973;5:585–604

58) Venkateswara Rao KT, Ritchie RO. Micromechanisms of transient fatigue crack growth behavior in aluminium–lithium alloys following single tensile overloads. In: Fatigue crack growth under variable amplitude loading. Elsevier; 1988. p. 134–46.

59) L.P. Borrego, J.M. Ferreira, J.M. Pinho da Cruz, J.M. Costa, Evaluation of overload effects on fatigue crack growth and closure Eng Fract Mech, 70 (2003), pp. 1379–1397

60) Bichler CH, Pippan R. Direct observation of the residual plastic deformation caused by a single tensile overload. In: McClung RC, Newman Jr JC, editors. Advances in fatigue crack closure measurement and analysis, ASTM STP 1343. West Conshohocken: American Society for Testing and aterials; 1999. p.191–206

61) C. Makabe, A. Purnowidodo, A.J. McEvily, Effects of surface deformation and crack closure on fatigue crack propagation after overloading and underloading Int J Fatigue, 26 (2004), pp. 1341-1348

62) Ch. Bichler, R. Pippan Effect of single overloads in ductile metals: A reconsideration Eng Fract Mech, 74 (2007), pp. 1344–1359

63) R.I. Barabash, J.S. Chung, S.Y. Lee, P.K. Liaw, H. Choo, Y. Sun, et al. Neutron and X-ray Microbeam Diffraction Studies around a Fatigue-Crack Tip after Overload Metall Mater Trans A, 39 (2008), pp. 3164–3169

64) S.Y. Lee, H. Choo, P.K. Liaw, E.C. Oliver, A.M. Paradowska In situ neutron diffraction study of internal strain evolution around a crack tip under variable-amplitude fatigue-loading conditions Scripta Mater, 60 (2009), pp. 866–869

65) J. Codrington, A. Kotousov Crack growth retardation following the application of an overload cycle using a strip-yield model Eng Fract Mech, 76 (2009), pp. 1667–1682

66) Krumar R, Garg SBL. Effect of yield strength and single overload cycles on effective stress intensity range ratio in 6061-T6 Al alloy Engng Fract Mech 1989;34(2):403–12.

67) Ling MR, Schijve J. The effect of intermediate heat treatments on overload induced retardations during fatigue crack growth in an Al-alloy. Fatigue Fract Engng Mater Struct 1992;15(5):421–30.

68) Skorupa M, Skorupa A, Schijve J, MachniewiczT, Korbut P. Effect of specimen thickness and stress ratio on fatigue crack growth after a single overload cycle on structural steel. In: Proceedings 13th European Conference on Fracture (ICF13). Elsevier, 2000.

69) S Suresh, Fatigue of materials, second edition, Cambridge University press, 2006

70) Shercliff H.R. and Fleck N.A., "Effect of specimen geometry on fatigue crack growth in plane strain – II. Overload response", Fatigue Fract. Engng Mater. Struct., 13, 297-310 (1990)

71) Fleck N.A., "Influence of stress state on crack growth retardation", in Basic Questions in Fatigue: Volume 1 (Ed. Fong J.T. and Fields R.J.) pp. 157-183, ASTM STP 924, American Society for Testing and Materials, Philadelphia (1988)

72) C. M. Hudson and H. F. Hardrath, Effects of changing stress amplitude on the rate of fatigue crack propagation of two aluminium alloys. NASA Technical Note D-960

73) J. Wang, J.X. Gao, W.L. Guo, Y.P. Shen, Effects of specimen thickness, hardening and crack closure for the plastic strip model, Theoretical and Applied Fracture Mechanics, Volume 29, Issue 1, April–May (1998), Pages 49-57

74) D. Broek and J. Schijve, NRL Report TRM2119, The Netherlands

75) T. C. Lindley and C. E. Richards, The relevance of crack closure to fatigue crack propagation. Mater. Sci. Engng 14, 281-293

76) A. J. McEvily, Current aspects of fatigue. Met. Science 11, 274-284 (1977)

77) Damri D. and Knott J.F., "Fracture modes encountered following the application of a major tensile overload cycle", Int. J. Fatigue, 15, 53-60 (1993)

78) Ng'Ang' A.S.P. and James M.N., "Variable amplitude loading in En8 (080M40) steel: a detailed experimental study of crack growth", Fatigue Fract. Engng Mater. Struct., 19, 217-216 (1996).

79) Shuter D.M. and Geary W., "The influence of specimen thickness on fatigue crack growth retardation following an overload", Int. J. Fatigue, 17, 111-119 (1995).

80) Robin C., Louah M. and Pluvinage G., "Influence of the overload on the fatigue crack growth in steels", Fatigue Fract. Engng Mater. Struct., 6, 1-13 (1983)

81) Shin C.S. and Hsu S.H., "On the mechanisms and behaviour of overload retardation in AISI 304 stainless steel", Int. J. Fatigue, 15, 181-192 (1993)

82) Endo, K., Okada, T., Komai, K. and Kiyoto, M. (1972) Fatigue crack propagation of steel in oil. Bull. JSME. 15, 1316–1323

83) Pineau, A. G. and Pelloux, R. M. (1974) Influence of strain-induced martensitic transformations on fatigue crack growth rates in stainless steels. Metall. Trans. 5, 1103–1112

84) S. Suresh Crack deflection: implications for the growth of long and short fatigue cracks Metal Trans A, 14 (11) (1983), pp. 2375–2385

85) R. H. Christensen, Metal Fatigue. McGraw-Hill, New York (1959).

86) Griffith, A. A. (1921), "The phenomena of rupture and flow in solids" (PDF), Philosophical Transactions of the Royal Society of London, A, 221: 163–198

87) P.C. Paris, M.P. Gomez, and W.E. Anderson. A rational analytic theory of fatigue. The Trend in Engineering, 1961, 13: p. 9-14

88) J. R. Rice, Mechanics of crack tip deformation and extension by fatigue, in fatigue crack propagation. ASTM STP 415, 247-311

89) WELLS, A.A. Unstable Crack Propagation in Metals. In: Propagation Symposium Proc., 1962, United Kingdom. Cleavage and Fast Fracture Crack. United Kingdom: Cranfield College Of Aeronautics, September 1961. p. 210

90) H.L. Ewalds, R. J. H. Wanhill, Fracture Mechanics, Butterworth-Heinemann Ltd, May 1984

91) BS ISO 12108:2012 Metallic materials- Fatigue testing- Fatigue crack growth method

92) Airy, G.B., Report of the British Association for the advancement of science, 1862

93) Westergaard, H.M., Bearing pressures and cracks. Journal of Applied Mechanics, 1939. 6: p. 49

94) https://www.ndeed.org/EducationResources/CommunityCollege/Materials/Structure/strengthenig.htm

95) Richards, C.E., The Measurement of crack length and shape during fracture and fatigue. Beevers, C.E. Ed., Engineering Materials Advisory Services, U.K., 1980. p. 461

96) Bathias, C., Plastic Zone Formation and Fatigue Crack Growth. 4th International Conference on Fracture II, 1977. p. 1307-1312.

97) Shanmugham, S. and Liaw P.K., Detection and monitoring of fatigue cracks. Fatigue and Fracture ASM Handbook. (19): p. 210-223

98) Hahn, G.T. and Rosenfield, A.R., Sources of fracture toughness: the relation between K and the ordinary tensile properties of metals in applications related phenomenon in Titanium alloys. AmericanSo ciety for Testing and Materials, 1968. p. 5-32.

99) Luo, L.G., Ryks, A. and Embury, J.D., On the development of a metallographic method to determine the strain distribution ahead of a crack tip. Metallography, 1989. 23: p. 101-117

100) Kwun, S.I. and Fine, M.E., Dependence of cyclic plastic work of fatigue crack propagation on AK in MA87 Al P/M alloy. Scripta Metallurgica, 1980. 14: p. 155-158.

101) Iino, Y., Accumulated plastic zone around fatigue crack in type 304 stainless steel. Material Science and Technology, 1976. 10(5): p. 159- 164.

102) Tschegg, E., Faltin, C. and Stanzl, S., X-ray microbeam and recrystallization studies of plastic deformation around fatigue cracks. Journal of Material Science, 1980. 15(1): p. 131-138.

103) Fine, M.E. and Davidson, D.L., Quantitative measurement of energy associated with a moving crack in Fatigue Mechanisms: Advances in quantitative measurement of physical damage. American Society for Testing and Materials, 1983. p. 350-370

104) Fatigue Crack Growth and Applications, Farahmand, Bahram, Fracture Mechanics of Metals, Composites, Welds, and Bolted Joints: Application of LEFM, EPFM, and FMDM Theory, 2001, Springer, P 118-179

105) Chanani, G.R., Determination of plastic-zone sizes at fatigue-cracks by optical interference technique. International Journal of Fracture, 1977. 13(1): p. 394-399 .

106) Nicoletto, G. (1987). Fatigue crack tip strains in 7075-T6 aluminum alloy. Fatigue Fract. Eng. Mater. Struct. 10, 37–49

107) T.E. Tay, C.M. Yap, C.J. Tay, Crack tip and notch tip plastic zone size measurement by the laser speckle technique, Engineering Fracture Mechanics, Volume 52, Issue 5, 1995, Pages 879-893

108) A. Azushima and M. Miyagawa, Measurement of the plastic zone around a fatigue crack of a stainless steel structure member with a laser beam. Proc. of Joint Conf on Experimental Mech., pp. 709-713 (1982)

109) Steuwer, A., Edwards, L., Pratihar, S., Ganguly, S., Peel, M., Fitzpatrick, M. E., Marrow, T. J. Withers, P. J., Sinclair, I., Singh, K. D., Gao, N., Buslaps, T. and Buffiere, J.-Y. (2006). In situ analysis of cracks in structural materials using synchrotron X-ray tomography and diffraction. Nuclear Instruments and Methods in Physics Research, Section B: Beam Interactions with Materials and Atoms 246, 217–225

110) Patterson, E.A. and Olden, E.J., Optical analysis of crack tip stress fields: a comparative study. Fatigue and Fracture of Engineering Materials and Structures, 2004. 27 (7): p. 623–636

111) Lee, O.S. and Hong, S.K., Determination of stress intensity factors and J integrals using the method of caustics. Engineering Fracture Mechanics, 1993. 44: p. 981-989.

112) Green A.E., Lindsay K.A.: Thermoelasticity, J. Elast. 2, 1 (1972) pp 1-7

113) Patki, A.S. and Patterson, E.A., Thermoelastic stress analysis of fatigue cracks subject to overloads. Fatigue & Fracture of Engineering Materials & Structures, 2010. 33(12): p. 809-821.

114) Stanley, P. and Chan, W.K., The determination of stress intensity factors and crack tip velocities from thermoelastic infra-red emissions. In: Proceedings of International Conference of Fatigue of Engineering Materials and Structures, 1986. c262: p. 105–114.

115) Lesniak, J.R., Bazile, D.J., Boyce, B.R., Zickel, M.J., Cramer, K.E. and Welch, C.S., Stress intensity measurement via infrared focal plane array. Non-Traditional Methods of Sensing Stress, Strain, and Damage in Materials and Structures. ASTM STP 1318, 1997.

116) Lin, S.T., Feng, Z. and Rowlands, R.E., Thermoelastic determination of stress intensity factors in orthotropic composites using the J-integral. Engineering Fracture Mechanics, 1997. 56(4): p. 579-592.

117) Nurse, A.D. and Patterson, E.A., Determination of predominantly mode II stress intensity factors from isochromatic data. Fatigue & Fracture of Engineering Materials & Structures, 1993. 16: p. 1339–1353.

118) Tomlinson, R.A., Nurse, A.D. and Patterson, E.A., On determining stress intensity factors for mixed mode cracks from thermoelastic data. Fatigue & Fracture of Engineering Materials & Structures, 1997. 20, p. 217–226.

119) Diaz, F.A., Yates, J.R. and Patterson, E.A., Some improvements in the analysis of fatigue cracks using thermoelasticity. International Journal of Fatigue, 2004. 26: p. 365–376.

120) M. Rossi, M. Sasso, G. Chiappini, E. Mancini, D. Amodio Identification of the plastic zone using digital image correlation Frattura ed Integrità Strutturale, 30 (2014) 552-557

121) Issues in structural and materials engineering, 2011, Published by Scholarly Editions, Atlanta, Georgia

122) Poissant, J. & Barthelat, A Novel “Subset Splitting” Procedure for Digital Image Correlation on Discontinuous Displacement Fields, F. Exp Mech (2010) 50: 353

123) Du, Y., Díaz, F.A., Burguete, R.L., Patterson E. A., Evaluation Using Digital Image Correlation of Stress Intensity Factors in an Aerospace Panel, Exp Mech (2011) 51: 45

124) A Brief History of the Microscopy Society of America, http://www.microscopy.org

125) Becker, W.T. and Lampman, S., Fracture Appearance and Mechanisms of Deformation and Fracture. ASM Handbook, 2002. 11: p. 559-586.

126) Davidson, D.L. and Lankford, J., Fatigue Mechanisms: Advances in quantitative measurement of Physical Damage. Fatigue Engineering and Material Structures, 1983. 6: p. 241.

127) Davidson, D.L. and Lankford, J., Fatigue crack growth in metals and alloys: mechanisms and micromechanics. International Materials Reviews, 1992. 37, p. 45-76

128) Brown, C.W. and Smith, G.C., Advances in Crack Length Measurement. Chamelon Press Ltd, London, 1982. p. 41.

129) Blochwitz, C. and Tirschler, W., In-situ scanning electron microscope observations of the deformation behaviour of short cracks. Materials Science and Engineering, 2000. A276: 273–276

130) Jieping, Z., Cheng, G. and Huljin, Z., Tensile deformation and fracture in high purity Titanium: In Situ Observation by Scanning Electron Microscope. Materials Science and Engineering, 1989. A114: p. 89-96.

131) Crompton, J.S. and Martin, W., The study of local plastic strain in nickel based superalloys by selected area channelling patterns in the STEM. Metallography, 1980. (13): p. 225-234.

132) Joy, D.C., Newbury, D.E. and Hazzledine, P.M., Anomalous crystallographic contrast on rolled and annealed specimens. Scanning Electron Microscopy Symposium, 1972. p. 97–104.

133) Joy, D.C., The observation of crystalline materials in the scanning electron microscope. Journal of Microscopy, 1972. (103): p. 1–23.

134) Davidson, D.L. and Lankford, J., Fatigue crack tip plastic strain in high strength aluminium alloys. Fatigue of Engineering Materials and Structures, 1980. (3): p. 289-303.

135) J. Guyon, H. Mansour, N. Gey, M.A. Crimp, S. Chalal, N. Maloufi, Sub-micron resolution selected area electron channeling patterns, In Ultramicroscopy, Volume 149, 2015, Pages 34-44,

136) Wilkinson, A.J., Gonzalez, G. and Dingley, D.J., The measurement of local plastic deformation in metal-matrix composite by electron back-scatter patterns. Journal of Microscopy, 1993. (169): p.255-261.

137) Wilkinson, A.J. and Dingley, D.J., The distribution of plastic deformation in a metal matrix composite caused by straining transverse to the fibre direction. Acta Metallurgica Materialia, 199. 40(12): P. 3357-3368.

138) Quested, P.N., Henderson, P.J. and Mclean, M., Observations of deformation and fracture heterogeneities in a nickel base superalloy using electron backscattering patterns. Acta Metallurgica, 1988. 36: p. 2743- 2752.

139) Jia, N., Lin Peng, R., Chai, G.C., Johansson, S. and Wang, Y.D., Direct experimental mapping of microscale deformation heterogeneity in duplex stainless steel. Material Science and Engineering. A, 2008. (491): p. 425- 433.

140) Liu, W., Ice, G.E., Larson, B.C., Yang, W., Tischler, J.Z. and J.D. Budai., The three dimensional X-ray crystal microscope: A new tool for materials characterization. Metallurgical and Materials Transactions A, 2004. (35A): p. 1963–1967.

141) Barabash, O.M., Santella, M., Barabash, R.I., Ice, G.E. and Tischler, J., Measuring depth dependent dislocation densities and elastic strain in an indented Ni-based superalloy. JOM, 2010. 62(12): p. 29-34

142) Hruby P., Understanding Plasticity and Fracture in Aluminum Alloys and their Composites by 3D X-ray Synchrotron Tomography and Microdiffraction, Arizona State University May 2014

143) Withers PJ., Fracture mechanics by three-dimensional crack-tip synchrotron X-ray microscopy. Philosophical transactions Series A, Mathematical, physical, and engineering sciences. 2015; 373- 2036

144) Yang, Y., Crimp, M., Tomlinson, R.A. and Patterson E.A., Quantitative Measurement of Plastic Strain Field at a Fatigue Crack Tip. Proceedings of the Royal Society, 2012. p. 1-17

145) Newman, J.C., "A Finite Element Analysis of Fatigue Crack Closure." ASTM STP 590, American Society for Testing and Materials, Philadelphia, PA, 1976, pp. 281–301.

146) McClung, R.C. and Raveendra, S.T., "On the Finite Element Analysis of Fatigue Crack Closure—1. Basic Modeling Issues." Engineering Fracture Mechanics, Vol. 33, 1989, 237–252.

147) K. Endo, T. Okada, K. Komai, M. Kiyoto, Bull. On the location of crack closure and the threshold condition for fatigue crack growth, JSME., 15 (1972) 1316.

148) Mei, Z. & Morris, J.W. Influence of deformation-induced martensite on fatigue crack propagation in 304-type steels, MTA (1990) 21: 3137

149) Budiansky, B. and Hutchinson, J. W. (1978) Analysis of closure in fatigue crack growth. Trans. ASME., J. Appl. Mech. 45, 267–276

150) N.A. Fleck Finite element analysis of plasticity-induced crack closure under plane strain conditions Engng. Fract. Mech., 25 (1986), pp. 441–449

151) Roy Chowdhury, S. and Dodds, R.H., Jr., "Three Dimensional Effects on Fatigue Crack Closure in the Small-Scale Yielding Regime." Fatigue & Fracture of Engineering Materials and Structures,Vol.26, 2003, pp. 663–673.

152) S. Suresh Crack deflection: implications for the growth of long and short fatigue cracks Metal Trans A, 14 (11) (1983), pp. 2375–2385

153) J. Schijve, Fatigue crack propagation in light alloy sheet materials and structures. NRL report MP 195, Amsterdam, The Netherlands

154) Elber, W. The significance of fatigue crack closure. Am. Soc. Testing Mater. 486, 230-242. (1971)

155) J. Willenborg, R. M. Engle and H. Wood, A crack growth retardation model using an effective stress intensity concept. Technical Report TFR 71-701, Los Angeles Division, North American Rockwell (1971)

156) G. Marci and P. F. Packman, The effects of plastic wake zone on the conditions for fatigue crack propagation. Int. J. Fracture 16, 282-295 (1980)

157) Walker, N. and Beevers, C. J. (1979) Fatigue crack closure mechanism in titanium. Fatigue Fract. Engng. Mater. Structs. 1, 135–148

158) González-Herrera A, Zapatero J. Influence of minimum element size to determine crack closure stress by the finite element method. Eng Fract Mech 2005;72:337–55.

159) P. Lopez-Crespo, A. Shterenlikht, J.R. Yates, E.A. Patterson, P.J. Withers, Some experimental observations on crack closure and crack-tip plasticity. Fatigue Fract. Fatigue Fract Eng Mater Struct, 32 (2009), pp. 418–429

160) E.A. Patterson,M. N. James Crack tip shielding effects, Part 1, Forni di Sopra (UD), Italy, March 7-9, (2011), 96-103

161) J.M. Vasco-Olmo, F.A. Díaz, Experimental evaluation of plasticity-induced crack shielding from crack tip displacements fields,2015, Frattura ed Integrità Strutturale 9(33):191-198

162) F.V. Antunes, R. Branco, J. D. Costa And D. M. Rodrigues, Plasticity induced crack closure in Middle-Crack Tension specimen: numerical versus experimental

163) Becker, T. H., Mostafavi, M., Tait, R. B., Marrow, T. J. (2012) An approach to calculate the J integral by digital image correlation displacement field measurement. Fatigue Fract. Engng Mater. Struct., 35, 971–984.

164) Song, H., Zhang, H., Fu, D., Kang, Y., Huang, G., Qu, C., Cai, Z. (2013) Experimental study on damage evolution of rock under uniform and concentrated loading conditions using digital image correlation. Fatigue Fract. Engng Mater. Struct., 26, 760–768.

165) Nowell, D., Paynter, R. J. H., de Matos, P. F. P. (2010) Optical methods for measurement of fatigue crack closure: moiré interferometry and digital image correlation. Fatigue Fract. Engng Mater. Struct.,33, 778–790.

166) Nowell, D, De Matos, P. F. P.,. (2008) Experimental and numerical investigations of thickness effects in plasticity-induced fatigue crack closure. Int. J. Fatigue, 31, 1795–1804

167) P. López-Crespo, R.L. Burguete, E.A. Patterson, A. Shterenlikht, P.J. Withers, J.R. Yates., Study of a Crack at a Fastener Hole by Digital Image Correlation, Experimental Mechanics (2009) 49:551-559

168) E.A. Patterson,M. N. James Crack tip shielding effects, Part 1, Forni di Sopra (UD), Italy, March 7-9, (2011), 96-103

169) Leaity, G. P. and Smith, R. A. (1989) The use of SPATE to measure residual stresses and fatigue crack growth. Fatigue Fract. Engg. Mater. Struct. 12, 271–282

170) Fulton, M. C. (1998) Improved evaluation of stress intensity factors from SPATE data. In: Proceedings of the 11th International Conference on Experimental Mechanics, 1211–1216

171) Dulieu-Barton, J. M., Fulton, M. C. and Stanley, P. (2000) The analysis of Thermoelastic isopachic data from crack tip stress field. Fatigue Fract. Engg. Mater. Struct. 23, 301–314

172) Diaz, F. A., Yates, J. R. and Patterson, E. A. (2004) Some improvements in the analysis of fatigue cracks using thermoelasticity. Int. J. Fatigue 26, 365–376

173) J. Codrington, A. Kotousov Crack growth retardation following the application of an overload using a strip-yield model Eng Fract Mech, 76 (2009), pp. 1667–1682

174) 0. C. Wheeler, Spectrum loading and crack growth. J. Basic Engng Trans. ASME, Series D 94(l), 181-186 (1972).

175) Lu, Y. and Li, K. A new model for fatigue crack growth after a single overload. Engg. Fract. Mech. 46, 1993, 849–856

176) Lopez-Crespo, P., Withers, P.J., Yusof, F., Dai, H., Steuwer, A., Kelleher, J.F., Buslaps, T., Overload effects on fatigue crack-tip fields under plane stress conditions: surface and bulk analysis. Fatigue Fract Eng Mater Struct, 36 (2013) 75-84

177) Lide, D. R., ed. (2005). CRC Handbook of Chemistry and Physics (86th ed.). Boca Raton (FL): CRC Press

178) Moiseyev, Valentin N. (2006). Titanium Alloys: Russian Aircraft and Aerospace Applications. Taylor and Francis,

179) Shoesmith, D. W.; Noel, J. J.; Hardie, D.; Ikeda, B. M. (2000). "Hydrogen Absorption and the Lifetime Performance of Titanium Nuclear Waste Containers". Corrosion Reviews. 18 (4–5)

180) P. DeGarmo, J.T. Black, R.A. Kohser Materials and Processes in Manufacturing John Wiley, New York (2003)

181) H. Kacer, E. Atik, C. Miric J. “The effect of precipitationhardening conditions on wear behaviours at 2024 aluminium wrought alloy” Mater. Processing Tech., 142 (3) (2003), 762-766

182) Degarmo, E. Paul; Black, J T.; Kohser, Ronald A. (2003), Materials and Processes in Manufacturing , Wiley

183) BS EN ISO 10275:2014, Metallic materials. Sheet and strip. Determination of tensile strain hardening exponent

184) Pitarresi, G. and Patterson, E. A. (2003) A review of the general theory of thermoelastic effect. J Strain Anal, 38, 405-417

185) W. Weber: Über die spezifische Wärme fester Körper insbesondere der Metalle, Ann. Phys. Chem. 96, 177–213 (1830)

186) W. Thomson (Lord Kelvin): On dynamical theory of heat, Trans. R. Soc. Edinburgh 20, 261–283 (1853)

187) K.T. Compton, D.B. Webster: Temperature changes accompanying the adiabatic compression of steel: verification of W. Thomson’s theory to a very high accuracy, Phys. Rev. 5, 159–166 (1915)

188) FLIR SC7000 Series Infrared Cameras Datasheet, http://www.flir.co.uk

189) Diaz Garrido F.A., 2004. Development of a methodology for thermoelastic investigation of the effective stress intensity factor. PhD thesis, University of Sheffield

190) Diulieu-Smith JM. Alternative calibration techniques for quantitative thermoelastic stress analysis. Strain. 1995 ;31 :9-16

191) Muskhelishvili, N.I., Some basic problems of the mathematical theory of elasticity (3rd Edition).

1953. Noordhoff Ltd. Groningen, Holland

192) A. D. Nurse and E. A. Patterson (1993) Determination of predominantly mode II stress intensity factors from isochromatic data. Fatigue Fract. Engng Muter. Struct. 16(12), 1339- 1354

193) Williams, M.L., On the stress distribution at the base of a stationary crack. Journal of Applied Mechanics, 1957. 24: p. 109-114.

194) Neider JA, and Mead R. A simplex methodfor junction minimization. Comp J. 1965;7:308-313.

195) Press WH. Numerical recipes in C: The art of scientific computing. Cambridge: Cambridge University Press, 1988.

196) Stanley P, and Chan WK. The determination of stress intensity factors and crack tip velocities from thermoelastic infra-red emissions. In: Proceedings of International Conference of Fatigue of Engineering Materials and Structures. Sheffield, UK: c262, IMechE; 1986. p. 105-114.

197) McMullan D., "Scanning electron microscopy 1928–1965".2006 Scanning. 17 (3): 175–185

198) Wilkinson AJ, High resolution measurements of strain and tilt distributions in SiGe mesas using electron backscatter diffraction, Applied Physics Letters, (2006), vol. 89, 241910

199) Kamaya M, Wilkinson AJ, Titchmarsh JM, Quantification of plastic strain of stainless steel and nickel alloy by electron backscatter diffraction Acta Materialia (2006), vol. 54, 239-248

200) Tucker AM, Wilkinson AJ, Henderson MB and Martin JW, Measurement of fatigue crack plastic zones in fine-grained materials using electron backscatter diffraction Material Science and Technology (2000), vol.16, 457-462

201) Meaden G. and Dingley D. J., Wilkinson A. J., High Resolution Elastic Strain Measurement from Electron Backscatter Diffraction Patterns- New Levels of Sensitivity Ultramicroscopy (2006), vol. 106, 307-313

202) Nye J., Some geometrical relations in dislocated crystals, Acta metallurgica 1953;Volume 1, Issue 2:153-162

203) Joy, D. C. (1975), The observation of crystalline materials in the scanning electron microscope (SEM). Journal of Microscopy, 103: 1–23. doi:10.1111/j.1365-2818.1975

204) Bieler, T.R., Crimp, M.A., Yang, Y., Wang, L., Eisenlohr, P., Mason, D.E., Liu, W., Ice, G.E., 2009, Strain heterogeneity and damage nucleation at grain boundaries during monotonic deformation in commercial purity titanium, JOM, 61, 45-52

205) https://www.plymouth.ac.uk/your-university/about-us/university-structure/faculties/scienceengineering/electron-microscopy-centre

206) https://deben.co.uk/wp-content/uploads/2012/12/Gatan-MTEST2000ES

207) Chona, R., Irwin, G. R. and Sanford, R. J. (1983) Influence of specimen size and shape on the singularity-dominated zone. In: Proceedings of the ASTM STP 791: Fracture Mechanics Fourteenth Symposium, Vol. 1, pp. 3–23.

208) Institute of material science - University of Kiel – Observation of dislocations and defects

209) F.A. McClintock and G.R. Irwin, Fracture Toughness Testing and Its Applications, plasticity aspects of fracture mechanics, ASTM STP 381, 1965 pp 84–113

210) Weisstein, Eric W. "Bean Curve", "Cardioid." From MathWorld--A Wolfram Web Resource.

211) R. A. Tomlinson and E. A. Patterson, Examination of Crack Tip Plasticity Using Thermoelastic Stress Analysis. Thermomechanics and Infra-Red Imaging, Volume 7 pp 123-129

212) D.L. Davidson and J. Lankford, Fatigue crack tip plastic strain in high-strength aluminium alloys, Fatigue of Engng. Mater. Struct., (3):289-303, 1980.

213) G. Konig and W. Blum, Comparison between cell structures produced in aluminium by cycling and monotonic creep, Acta Metall., (28):519-537, 1980

214) P. Mazal, F. Vlasic, V. Koula, Use of acoustic emission method for identification of fatigue micro-cracks creation 6th Fatigue Design conference, Fatigue Design 2015 Procedia Engineering 133 (2015), 379 – 388

215) http://www.springer.com/978-0-387-26883-5